

FORMATION AND QUANTIFICATION OF CORROSION

DEPOSITS IN THE POWER INDUSTRY

Haritha Namduri, B.E., M.S.

Dissertation Prepared for the Degree of

DOCTOR OF PHILOSOPHY

UNIVERSITY OF NORTH TEXAS

May 2007

APPROVED:

Seifollah Nasrazadani, Major Professor  
Michael Kaufman, Committee Member and Chair  
of the Department of Materials Science and  
Engineering  
Brian Gorman, Committee Member  
Jeff Kelber, Committee Member  
Nandika D'Souza, Program Coordinator  
Oscar Garcia, Dean of the College of Engineering  
Sandra L. Terrell, Dean of the Robert B. Toulouse  
School of Graduate Studies

Namduri, Haritha. *Formation and Quantification of Corrosion Deposits in the Power Industry*. Doctor of Philosophy (Materials Science and Engineering), May 2007, 163 pp., 16 tables, 55 figures, references, 153 titles.

The presence of deposits on the secondary side of pressurized water reactor (PWR) steam generator systems is one of the main contributors to the high maintenance costs of these generators. Formation and transport of corrosion products formed due to the presence of impurities, metals and metallic oxides in the secondary side of the steam generator units result in formation of deposits.

This research deals with understanding the deposit formation and characterization of deposits by studying the samples collected from different units in secondary side system at Comanche Peak Steam Electric Station (CPSES). Fourier transform infrared spectrophotometry (FTIR), scanning electron microscopy (SEM) and energy dispersive spectroscopy (EDS) have been used for studying the phases, morphologies and compositions of the iron oxides formed at Unit 1 and Unit 2 of secondary side of steamgenerator systems. Hematite and magnetite were found to be the dominant phases of iron oxides present in the units. Fe, Cr, O, Ni, Si, Cl and Cu were found in samples collected from both the units.

A qualitative method was developed to differentiate iron oxides using laser induced breakdown spectroscopy (LIBS) based on temporal response of iron oxides to a high power laser beam. A quantitative FTIR technique was developed to identify and quantify iron oxides present in the different components of the secondary side of the steam generator of CPSES.

Amines are used in water treatment to control corrosion and fouling in pressurized water reactors. CPSES presently uses an amine combination of dimethylamine (DMA), hydrazine and morpholine to control the water chemistry. Along with the abovementioned amines, this study

also focuses on corrosion inhibition mechanisms of a new amine DBU (1, 8-diazabicyclo [5.4.0] undec-7-ene). Electrochemical impedance spectroscopy and polarization curves were used to study the interaction mechanism between DBU solution and inconel alloys 600 and 690 at steam generator operating temperatures and pressures. Of all the amines used in this study (DMA, DBU, ETA, and morpholine), DMA was more effective at keeping the passive film formed on the alloy 600 surface from failing at both ambient and high temperatures. Morpholine was found to result in higher corrosion resistance compared to the other amines in case of alloy 690.

Copyright 2007

by

Haritha Namduri

## ACKNOWLEDGEMENTS

I take this opportunity to express my deep regards to my committee chair Dr. Seifollah Nasrazadani for his exemplary guidance and considerate support in completion of this research work. I would also like to thank my other committee members, Dr. Michael Kaufman, Dr. Brain Gorman (Department of Materials Science and Engineering, University of North Texas,), Dr. Jeff Kelber (Department of Chemistry, University of North Texas) for their consistent support and encouragement. I would also like to thank Mr. Jim Stevens and Mr. Robert Theimer (Chemistry Group, TXU, Glenn Rose, TX) for their significant contribution and support towards this research.

I like to thank all my colleagues Mr. Jorge Diaz, Mr. Walter Maranon, Ms. Vaishali Paliwal, Mr. Bobby Grimes and all other students and faculty of the Departments of Materials Science and Engineering, and Engineering Technology for their co-operation without which this research would not have completed on time. Finally I would like to thank my family and friends for their constant encouragement and support.

## TABLE OF CONTENTS

	Page
ACKNOWLEDGEMENTS .....	iii
LIST OF TABLES .....	vii
LIST OF ILLUSTRATIONS .....	viii
 Chapter	
1. INTRODUCTION .....	1
1.1. Main Objectives .....	2
1.2. Comanche Peak Steam Electric Station (CPSES) .....	3
1.3. Corrosion Issues in Nuclear Power Plants .....	5
1.3.1. Different Types of Corrosion Problems Encountered .....	6
1.3.2. Mechanism of Deposit Formation .....	7
1.3.3. Factors Controlling Deposit Formation .....	9
1.4. Corrosion Inhibitors Used in Nuclear Power Plants .....	10
1.5. Chapter References .....	13
2. LITERATURE REVIEW AND EXPERIMENT .....	17
2.1. Fundamentals Concepts of Corrosion in Ferrous Alloys .....	17
2.1.1. Electric Double Layer Model in Metals .....	18
2.2. Iron Oxides and Hydroxides .....	19
2.2.1. Dissolution Kinetics of Iron Oxides .....	20
2.2.2. Phase Transformation .....	21
2.2.3. Crystal Structure and Morphology .....	24
2.2.4. Characterization of Iron Oxides .....	26
2.3. Effect of Amines on Iron Oxides .....	27
2.4. Prevention of Corrosion-Role of Protective Oxides .....	30
2.5. Experimental Methodology .....	34
2.6. Chapter References .....	36
3. CHARACTERIZATION OF CORROSION PRODUCTS FORMED AT COMANCHE PEAK STEAM ELECTRIC STEAM STATION (CPSES) .....	44
3.1. Introduction .....	44

3.1.1.	Need for Deposit Characterization.....	45
3.2.	Experimental Procedure.....	46
3.3.	Results and Discussion .....	46
3.3.1.	Thickness Measurements of Deposits on Samples Collected From Unit 1 and Unit 2 Components .....	46
3.3.2.	Deposit Analysis of Different Components For Unit 1 and Unit 2 .....	50
3.4.	Summary and Conclusions .....	60
3.4.1.	Comparison of Samples for Unit 1 for Years 2002 and 2004 Outages .....	60
3.4.2.	EDS Quantification of Corrosion Deposits.....	66
3.5.	Chapter References .....	71
4.	STUDY OF PHASE TRANSFORMATION IN IRON OXIDES USING LASER INDUCED BREAKDOWN SPECTROSCOPY (LIBS).....	73
4.1.	Introduction.....	73
4.2.	Experimental Procedure.....	76
4.3.	Results and Discussion .....	78
4.3.1.	Laser Breakdown Induced Spectroscopy .....	78
4.3.2.	Fourier Transform Infrared Spectrophotometry .....	81
4.3.3.	X-Ray Diffraction .....	82
4.4.	Summary and Conclusions .....	84
4.5.	Chapter References .....	86
5.	QUANTITATIVE ANALYSIS OF IRON OXIDES USING FOURIER TRANSFORM INFRARED SPECTROPHOTOMETRY (FTIR).....	89
5.1.	Introduction.....	89
5.2.	Experimental Procedure.....	94
5.3.	Results and Discussion .....	95
5.4.	Summary and Conclusions .....	99
5.5.	Chapter References .....	103
6.	STUDY OF INTERACTION BETWEEN AMINES AND INCONEL ALLOYS .....	106
6.1.	Introduction.....	106
6.1.1.	Alloy 600 Vs Alloy 690.....	108

6.2.	Experimental Setup .....	110
6.2.1.	Room Temperature Studies.....	110
6.2.2.	High Temperature Studies .....	111
6.3.	Results and Discussion .....	113
6.3.1.	Room Temperature Studies.....	113
6.3.2.	High Temperature Studies .....	119
6.4.	Summary and Conclusions .....	137
6.5.	Chapter References .....	141
7.	CONCLUSIONS AND RECOMMENDATIONS .....	148
	REFERENCES .....	153



## LIST OF TABLES

	Page
1.1. Common redox reactions during corrosion in presence of common aggressive species .....	9
2.1. Eight forms of iron oxides and oxyhydroxides.....	19
3.1. Deposit thickness measurement of samples collected from Unit 1 .....	49
3.2. Deposit thickness measurement of samples collected from Unit 2 .....	49
3.3. Comparison of samples for Unit 1 for years 2002 and 2004 outages.....	61
3.4. Comparison of samples for Unit 2 for years 2002 and 2003 outages.....	66
3.5. Summary of characterization results for the samples collected from Unit 1 .....	63
3.6. Summary of characterization results for the samples collected from Unit 2.....	64
3.7. EDS Analysis of Unit 1, 2004 outage samples.....	67
3.8. EDS Analysis of Unit 2, 2005 outage samples.....	68
4.1. LIBS system operational parameters .....	77
5.1. Major metallic impurities found in steam generator cycle .....	91
5.2. Infrared bands of different iron oxides .....	93
5.3. FTIR Intensities for different known concentrations of iron oxides used in calibration curves (I = Intensity of iron oxide mixture, and I <sub>o</sub> = Intensity of 3640 cm <sup>-1</sup> peak of CaO) .....	97
5.4. Concentration of field sample collected from different components of secondary side of Unit 1 and Unit 2 steam generator system of CPSES.....	102
6.1. Chemical composition of alloys 600 and 690.....	112

## LIST OF ILLUSTRATIONS

	Page
1.1. Schematic showing different components in secondary side at CPSES.....	4
1.2. Chemical structure of a) morpholine, b) ETA, c) DMA, and d) DBU .....	12
2.1. Electrical double layer .....	18
2.2. Phase transformation in iron oxides.....	23
2.3. XRD spectra of – synthetic magnetite (Fe <sub>3</sub> O <sub>4</sub> ) and maghemite (γ-Fe <sub>2</sub> O <sub>3</sub> ) powders .....	27
2.4. Pourbaix (Potential-pH) Diagrams for a) nickel-water, b) chromium-water and c) ironwater systems at 288°C (Dissolved species activities of 10 <sup>-3</sup> ).....	33
3.1. Schematic of sample identification for samples from Unit 1 .....	47
3.2. Schematic of sample identification for samples from Unit 2 .....	48
3.3. SEM photographs of main condenser sample from a) & b) Unit 1 and c) & d) Unit 2..	51
3.4. EDS spectra of main condenser sample from a) Unit 1 and b) Unit 2.....	52
3.5. SEM photographs of feedwater heater samples collected from a) & b) Unit 1 and c) & d) Unit 2 .....	53
3.6. EDS analysis of feedwater heater samples collected from Unit 1 .....	54
3.7. EDS analysis of feedwater heater samples collected from Unit 2 .....	55
3.8. Moisture separator samples for a) Unit 1 and b) Unit 2 .....	56
3.10. Elemental mapping of moisture separator sample collected from Unit 2.....	57
3.11. FTIR spectra of samples collected from Unit 1 .....	58
3.12. FTIR spectra of samples collected from Unit 2 .....	59
3.13. EDS quantification of samples collected from a) condenser, b) LP heaters, c) HP heaters and d) moisture separator) .....	71
4.1. Schematic of laser set-up .....	77
4.2. Detector gate delay (μs) Vs intensity (Counts) for different iron oxides at wavelength λ = 373.39 nm at gate width 100 μs .....	79

4.3.	LIBS analysis for magnetite samples treated at a) 185°C, b) 250°C, c) 350°C and d) 500°C at $\lambda = 373.39$ nm .....	80
4.4.	LIBS analysis for magnetite samples treated at a) 185°C, b) 250°C, c) 350°C and d) 500°C at $\lambda = 373.39$ nm .....	80
4.5.	FTIR spectra of magnetite powder heated to different temperatures .....	83
4.6.	XRD analysis of magnetite samples treated at different temperatures a) 185°C for 2 hrs, b) 250°C for 1 hr c) 350°C for 1 hr and d) 500°C [M-magnetite, MH-maghemite and H-hematite] .....	85
5.1.	FTIR spectra of 100% CaCO <sub>3</sub> , hematite, maghemite and magnetite .....	97
5.2.	FTIR calibration for mixture containing magnetite and maghemite (630 cm <sup>-1</sup> peak for maghemite) .....	98
5.3.	FTIR calibration for mixture containing hematite and maghemite (540 cm <sup>-1</sup> peak for hematite) .....	98
5.4.	FTIR calibration for mixture containing magnetite and hematite (540 cm <sup>-1</sup> peak for hematite) .....	99
5.5.	FTIR spectra for samples collected from secondary side of SG at CPSES .....	101
6.1.	Equivalent circuit representation for electrochemical processes taking place at metal surface and solution .....	108
6.2.	Nyquist plots of Inconel 600 alloy exposed to DMA solution for 6, 12, 24 and 48 hrs	114
6.3.	Equivalent circuit for the Nyquist plot shown in DBU solution.....	114
6.4.	Nyquist plots of Inconel 600 alloy exposed to DMA solution for 6, 12, 24 and 48 hrs	116
6.5.	Equivalent circuit for the Nyquist plot shown in DMA solution.....	116
6.6.	Nyquist plots of Inconel 600 alloy exposed to ETA solution for 6, 12, 24 and 48 hrs.	118
6.7.	Equivalent circuit for the impedance response in the ETA solution .....	118
6.8.	Nyquist plot of Inconel 600 alloy exposed to morpholine solution for 6, 12, 24 and 48 hrs .....	120
6.9.	Equivalent circuit for the impedance response in the morpholine solution.....	120
6.10.	Nyquist plots of alloy 600 in morpholine solution at a) 100°C, b) 200°C, and c) 3 hrs at 300°C.....	123

6.11.	Nyquist plots of alloy 600 in ETA solution at a) 100°C, b) 200°C, and c) 3 hrs at 300°C	123
6.12.	Nyquist plots of alloy 600 in DMA solution at a) 100°C, b) 200°C, and c) 3 hrs at 300°C	124
6.13.	Nyquist plots of alloy 600 in DBU solution at a) 100°C, b) 200°C, and c) 3 hrs at 300°C	124
6.14.	Polarization resistance of alloy 600 for different amines	125
6.15.	SEM photographs of Inconel alloy 600 samples exposed to a) untreated, b) control, c) morpholine, d) ETA, e) DMA, and f) DBU for 3 hrs at 300°C in autoclave at pH = 9.0	127
6.16.	EDS elemental concentration of inconel 600 samples treated with untreated, morpholine, ETA, DMA, and DBU at 300°C for 3 hrs and pH = 9.0	128
6.17.	EDS spectra of alloy 600 samples exposed to ETA at 300°C for 3 hrs and pH = 9.0	129
6.18.	Nyquist plots of alloy 690 in morpholine solution at a) 100°C, b) 200°C, and c) 3 hrs at 300°C	131
6.19.	Nyquist plots of alloy 690 in ETA solution at a) 100°C, b) 200°C, and c) 3 hrs at 300°C	131
6.20.	Nyquist plots of alloy 690 in DMA solution at a) 100°C, b) 200°C, and c) 3 hrs at 300°C	132
6.21.	Nyquist plots of alloy 690 in DBU solution at a) 100°C, b) 200°C, and c) 3 hrs at 300°C	132
6.22.	Polarization resistance of alloy 690 for different amines	132
6.23.	SEM photographs of Inconel alloy 690 samples exposed to a) untreated, b) control, c) morpholine, d) ETA, e) DMA, and f) DBU for 3 hrs at 300°C in autoclave at pH = 9.0	135
6.24.	EDS elemental concentration of inconel 690 samples treated with untreated, morpholine, ETA, DMA, and DBU at 300°C for 3 hrs and pH = 9.0	136
6.25.	EDS spectra of alloy 690 sample exposed to ETA solution for 3 hrs at 300°C at pH = 9.0	137

## CHAPTER 1

### INTRODUCTION

Every year the cost of maintaining, repairing and inspecting steam generators (SG) at U.S. pressurized water reactor (PWR) plants exceeds \$100 million. This is approximately equivalent to \$1.5 million per plant. These costs exclude the costs incurred in routine inspection and repair. SG problems have frequently resulted in forced outages, extensions to regularly scheduled outages, and the need to perform mid-cycle inspections. An important factor that leads to high maintenance costs is the presence of deposits on the secondary side of SGs. The corrosion in secondary side is mainly attributed to three factors: water chemistry, hydrodynamic conditions and the presence of products such as zinc oxide and copper resulting from the condensers. These deposits are formed due to presence of impurities, metals, metallic oxides and other foreign particles. Metal oxides and other contaminants enter PWR SGs during operation, but usually only a small amount of total metal oxides entering systems are removed through the blowdown. The remaining oxides continue to build up and deposit in the SG. The majority of the deposit found in the SGs is composed of iron oxide along with other metal oxides depending on the materials used in the construction of the balance of the system<sup>1, 2</sup>.

Amines are added in secondary systems of steam generators to reduce the formation and transport of corrosion products. The corrosion products formed in these systems can lead to major maintenance and operational costs. Along with characterizing the corrosion deposits, this research was also focused in studying the effect of the organic amines on the Inconel alloy, which has been extensively used as materials in constructing steam generator tubing. The outcome of the study should give a better insight into the nature of the iron oxide deposit formation in the steam generators (SG) in the presence of amines. For example, the study of the

affect of amine added should help in controlling the chemistry in the secondary feedwater systems. The study should help in better understanding the local conditions of corrosion and its affect on the integrity of the steam generators. For example, steam generator fouling rates are a strong function of water and surface chemistry. Therefore, fouling can be mitigated by optimization of water chemistry<sup>3, 4, and 5</sup>.

### 1.1. Main Objectives

The thermal hydraulic performance and integrity of the steam generators may be compromised due to the presence of corrosion deposits. So it is very important to understand the nature of these deposits in detail. The main objective of this research is to characterize the corrosion deposits including iron oxides formed in secondary side of steam generator units at Comanche Peak Steam Electric Station (CPSES) in order to better interpret and control the corrosion processes. This dissertation is divided into eight chapters. The present chapter gives a brief introduction on corrosion aspects in nuclear power plants with special focus on CPSES. Chapter 2 gives background on studies performed in past by researchers in characterizing and controlling corrosion in nuclear power plants and fundamentals of corrosion in ferrous metals. Chapter 3 deals with characterization of corrosion deposits formed in unit 1 (outage no. 1RF10) and unit 2 (outage no. 2RF06) at CPSES and comparing these results to the data obtained from unit 1(outage no. 1RF09) and unit 2 (outage no. 2RF05) refueling outages. Identifying iron oxides is a very important step in characterizing corrosion deposits. Chapter 4 and chapter 5 deal with characterizing iron oxides both quantitatively and qualitatively. The phase of iron oxide present can have a great influence on the type of corrosion deposits formed in the feedwater trains. Chapter 6 presents the effect of amines on inconel alloy 600 and 690. During the

operation of reactor, the tube materials in the steam generator react with oxygen and oxides. The oxide properties depend on the water chemistry, temperature and the alloy composition<sup>6</sup>. The aim of the study in this chapter was to understand the fundamental effect of certain selected amines on the surface of inconel alloy, which is extensively used in construction of steam generator tubing, to efficiently characterize the corrosion products formed in power plants. Conclusions and references are given in chapters 7 and 8 respectively.

## 1.2. Comanche Peak Steam Electric Station (CPSES)

The Comanche Peak Steam Electric Station (CPSES) is a two-unit nuclear-fueled power plant located in Somervell County, Texas. Fuel for the plant is uranium dioxide. Each of the two units has a generating capacity of 1,150,000 kilowatts, for a total generating capacity of 300,000 kilowatts<sup>3</sup>. Comanche Peak is a relatively new plant with slightly more than 8 cycles of operation on unit 1 and nearly 6 full cycles on unit 2. Unit 1 steam generator (SG) mainly consists of mechanically expanded alloy 600 MA tubing whereas unit 2 SG has hydraulically expanded alloy 600, TT tubing. The corrosion resistance of the tubing in unit 2 is expected to be greater when compared to unit 1<sup>7</sup>.

CPSES has employed a variety of methods to assess the effectiveness of the deposit control program. These include extensive visual inspection programs and detailed corrosion product analysis and trending. Corrosion product is to be minimized in order to control fouling and corrosion in nuclear steam generators. The chemistry program at CPSES is designed to minimize corrosion release, corrosion product transport and solid deposition during operation and non steady conditions. Key to the strategy is control of soluble iron transport, which has

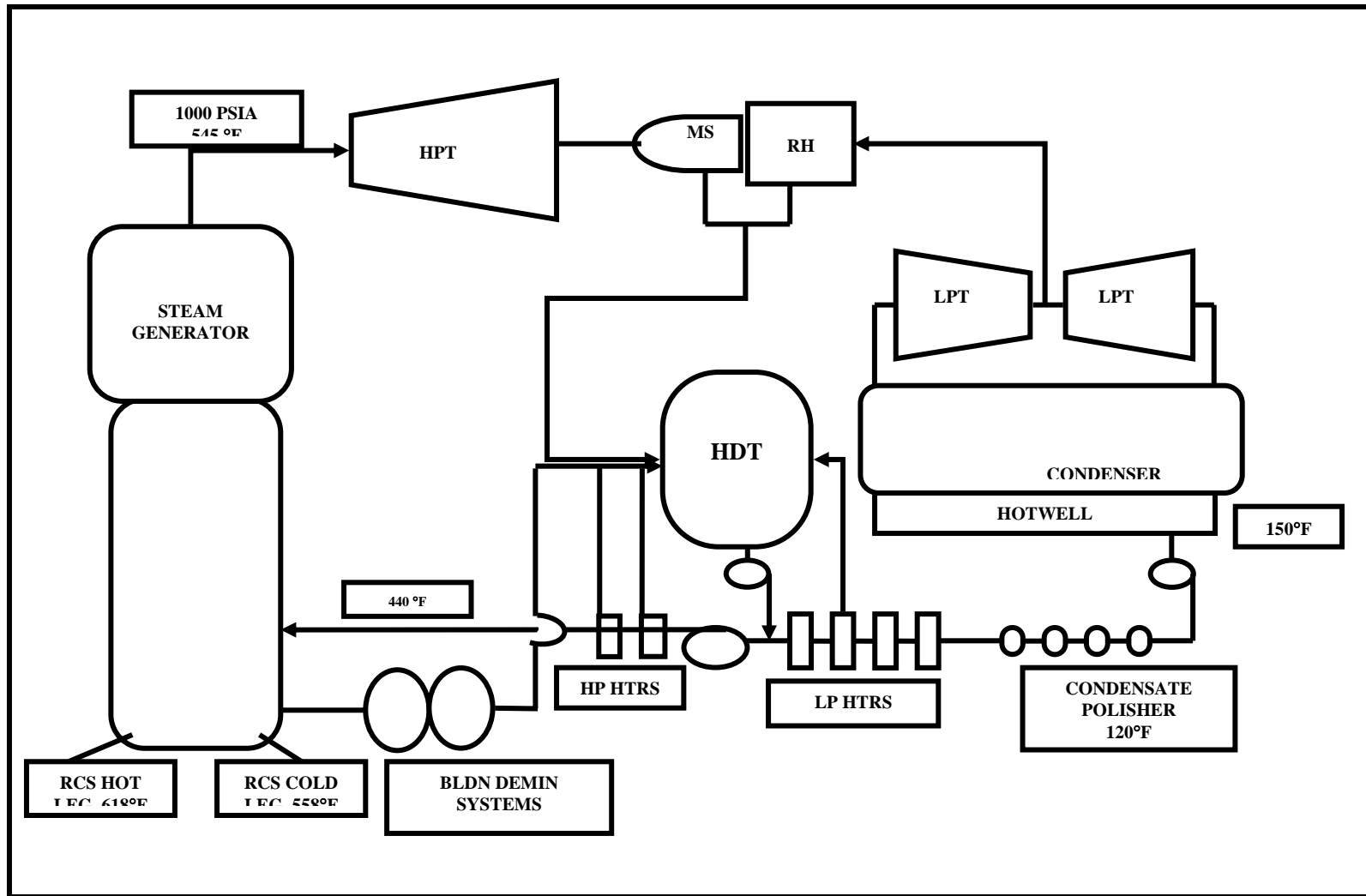


**Figure 1.1. Schematic showing different components in secondary side at CPSES**  
 (Reactor coolant system (RCS), blow down de-mineralizing system (BLDN DEMIN SYS), high pressure heaters (HP HTRS), low pressure heaters (LP HTRS), low pressure turbine (LPT), re-heater (RH), moisture separator (MS), high pressure turbine and (HPT), heater drain tank (HDT))



been found to be the cause of densification of tube deposits, or loss of porosity<sup>8</sup>. The typical layout of steam generator unit along with different components is given in Figure 1.1.

### 1.3. Corrosion Issues in Nuclear Power Plants

Corrosion products from various systems of the secondary side of steam generators accumulate together to form sludge. This sludge can cause very serious corrosion problems and can be very detrimental to the steam generator tubes and other parts of the steam generator system<sup>9</sup>. The major part of the cost involved in steam generator maintenance is mostly related directly or indirectly to the formation and transportation of corrosion products in the secondary systems<sup>10, 11</sup>. The corrosion products accumulate and increase the probability of corrosion in secondary side tube which includes stress corrosion cracking and inter-granular cracking. These corrosion products accumulate and form layers on the tube surfaces and many other flow passages in the secondary side. These deposits affect the performance and the maintenance cost of the power plant<sup>12</sup>. The characterization of these deposits will reveal both physical and chemical properties, which in turn would help the power plant to assess the extent of maintenance and inspection. The characterization of deposits can be used as first step by plant operations and chemistry in assessing feedwater, condensate and drain systems erosion-corrosion and overall chemistry control successes<sup>13</sup>. Documenting operation history, material condition, chemistry and deposit characterization of the plant together can prove to be very valuable information for future evaluations of changes in the material conditions or operations<sup>11, 14, 15</sup>.

Steam generators in PWR make the steam in secondary side by taking the heat from the primary reactor coolant and drive the turbines in secondary side using this steam. During the course of reactor operation, corrosion products and impurities from the make up water and

condenser leak accumulate on the tubes and tube sheets of the steam generator<sup>16</sup>. These impurities lead to a) loss in heat transfer efficiency, and b) under deposit attack of tubes leading to tube failure. During the course of reactor operation, most of the contaminants whether they are introduced as particles or as dissolved species into the secondary system circuit are accumulated in the steam generator. These contaminants lead to the fouling which in result leads to decrease in the heat efficiency of the steam generator<sup>17</sup>.

### 1.3.1. Different Types of Corrosion Problems Encountered in Nuclear Power Plants

The different types of corrosion problems that are typically found in nuclear power plants are as follows:

- a) Tube Wastage: This is also called thinning. This is the most typical corrosion problem that occurs in Recirculating Steam Generator (RSG) with sodium phosphate as a secondary water treatment.
- b) Denting: This type of corrosion occurs when the corrosion products build up in the crevices between the tubes and carbon steel tube support plates. In the past, changes in the chemistry of secondary side resulted in reducing tube denting<sup>18</sup>.
- c) Pitting: In this type of corrosion, the corrosion deposits form localized pits for accumulation of aggressive impurities like chlorides and copper oxides.
- d) Under Deposit Corrosion: In this kind of corrosion process, the tube scale deposits provide locations where corrosion deposits can concentrate and hence result in insulating the tubes. The typical corrosion species that are likely to deposit are copper oxides, lead and sulfur.
- e) Intergranular attack/stress corrosion cracking (IGA/SCC): This kind of corrosion occurs when cracks develop in metallic materials due to stress and corrosion. Typical example of this kind of

corrosion is cracking of welded pipes, made of stainless steel, in boiling-water reactors. The initiation and growth of IGA/SCC in inconel alloy 600 steam generator tubing has been shown to be a strong function of the local electrochemical potential and is known to increase in an oxidizing condition in caustic, acidic and neutral environments<sup>19</sup>.

f) Flow assisted corrosion (FAC): This kind of corrosion results in thinning of piping, vessels and other components in both primary and secondary side of the plant. This results when the protective oxide on the low carbon steel surfaces get dissolved when exposed to flowing fluid or steam. In the past it has been shown that the chromium concentration is an important parameter affecting FAC<sup>20</sup>.

g) Erosion-Corrosion: Two phase erosion-corrosion is one of the major world wide corrosion problems and has been experienced in nuclear electric's steam-water circuits both in the USA and the United Kingdom. This kind of corrosion occurs when the protective oxide layer on the steel is interfered by highly turbulent fluid thereby resulting in soluble iron. This kind of corrosion is not only dependent on the fluid flow conditions but also depends on the pH and steam quality in the steam generator cycle<sup>13</sup>.

### 1.3.2. Mechanism of Deposit Formation

The corrosion deposits can consist of a wide variety of elements. The materials used to construct secondary cycle components contain many alloying elements in addition to iron, copper and zinc. So the protective oxide layers that form on both ferrous and non-ferrous alloys consist of these minor alloying species. So, there is a possibility of these minor species getting transported into the feedwater and then into steam generator system.

The different impurities that can be present in the corrosion deposits can be categorized into ionic species, particulate and soluble species. The ionic species can be sodium, chlorides and sulfates. These ionic species can concentrate in the tube support crevices, sludge piles, within and under tube scale deposits. Sludge is formed by agglomeration of particulate impurities. These sludge particles settle down at the bottom of steam generator and form horizontal piles, especially in regions where the flow of feedwater velocity is low. Along with forming horizontal piles, the sludge can also form a scale by attaching to the tube surface. The particulate species mainly consist of iron and iron oxides, silicon dioxide, copper and copper oxides. Organics, organic species and gases can be categorized as soluble species. These species can react with each other and alter their chemical form resulting in formation of corrosive species<sup>1, 11</sup>.

The electrochemical reaction that takes place at the metal-liquid/ gas interface is called corrosion. At the metal-liquid interface, corrosion takes place after a thin liquid film is formed on the surface of the metal. Aqueous corrosion is more appropriate for corrosion taking place in the nuclear power plant. Many redox reactions take place in the steam cycle system<sup>21</sup>. Some of the cathodic and anodic reactions that take place in steam cycle systems are given in the Table 1.1.

The important factors which affect the corrosion of steel components are pH, temperature, presence of oxygen, and presence of CO<sub>2</sub>. Even low concentrations of oxygen present in the system can increase the corrosion. Presence of CO<sub>2</sub> is known to be one of the major sources of corrosion in steam cycle<sup>22, 23, 24</sup>. Deposits consist of different impurities which include metals like copper, lead, sulfur etc. These metals form different ionic species and some of these species combine with iron oxides and form complex spinels leading to increase in the deposit formation<sup>19</sup>. The corrosion product films on the carbon steel consist of magnetite, hematite, ferrous hydroxides and oxyhydroxides species. These species move through the

feedwater system and are known to transform into magnetite or maghemite as the temperature increases.

Jobe pointed out a three stage mechanism for the formation of corrosion product deposits in secondary side of steam generators: a) Dissolution of iron metal or the iron oxide into ionic forms, b) hydrolysis of these ionic species into oxyhydroxides, and c) deposits are formed by thermal degradation of the oxyhydroxides<sup>25</sup>. This three step mechanism clearly justifies a strong need for characterization of corrosion deposits including the phase transformation of iron oxides.

**Table 1.1. Common redox reactions during corrosion in presence of common aggressive species** (*Adapted from Varrin, EPRI, 1996*)

<b>Anodic Half reaction: <math>\text{Fe} \rightarrow \text{Fe}^{+2} + 2\text{e}^-</math></b>			
<b>Aggressive species</b>	<b>Cathodic Half reactions</b>		<b>Corrosion products</b>
	<b>Acidic</b>	<b>Neutral to basic</b>	
$\text{O}_2$	$\text{H}^+ + \text{e}^- \rightarrow 1/2 \text{H}_{2(\text{g})}$	$1/2 \text{O}_2 + \text{H}_2\text{O} + 2\text{e}^- \rightarrow 2\text{OH}^-$	$\text{Fe}_2\text{O}_3 (\text{s})$ , $\text{Fe}_3\text{O}_4 (\text{s})$
$\text{H}_2\text{S}$	Same	$\text{H}_2\text{S} + 2\text{e}^- \rightarrow \text{S}^{2-} + \text{H}_2$	$\text{FeS} (\text{s})$
$\text{CO}_2$	Same	$\text{H}_2\text{CO}_3 + 2\text{e}^- \rightarrow \text{CO}_3^{2-} + \text{H}_2$	$\text{FeCO}_3 (\text{s})$
$\text{H}^+$	Same	.....	$\text{Fe}^{2+} (\text{aq})$

### 1.3.3. Factors Controlling Deposit Formation

The important factors which effect corrosion of steel components are: pH, temperature, presence of oxygen, presence of  $\text{CO}_2$ . For example a pH of 6.5 will be 100 times more aggressive to mild steel than a pH of 7.5 and 10,000 times more aggressive than pH 8.5. As the temperature increases the corrosion increases. Even low concentrations of oxygen present in the

system can increase the corrosion. Presence of  $\text{CO}_2$  is one of the major sources of corrosion in steam cycle<sup>26</sup>. The concentration of some metallic species like copper, chromium, lead, sulfur, chlorides, etc., also plays an important role in controlling corrosion deposits.

Copper if present in the steam generator system, can result in formation of copper oxides and cupric ions.  $\text{Cu}^{2+}$  reacts with magnetite to form maghemite and copper metal<sup>27</sup>. Another common deposit constituent is nickel. From the past studies it has been found that nickel often combines with iron oxides to form spinels<sup>28</sup>. Even small percentages of lead can result in deleterious effects on the secondary side. The typical concentration of Pb entering the steam generator via feedwater is in the range of 0.05-400 ppt<sup>29</sup>. Sulfur is in the form  $\text{SO}_4^{2-}$ , sulfide ions and hydrogen sulfides in the secondary side. Sulfur enters steam generator via feedwater from a number of sources like makeup water, condenser lakes, chemical cleaning inhibitors etc. It is known that presence of sulfur leads to inter-granular attack and under deposit pits. Presence of species like Ca, Mg, Zn, Si and Al increase the pH conditions within the deposits and increase the potential for caustic SCC of the tubes. These compounds promote the initiation of tube scale formation and interfere with the heat transfer along the tubes.

#### 1.4. Corrosion Inhibitors used in Nuclear Power Plants

In past many utilities have elected to add amines to feedwater to control corrosion deposits formed in the steam generator systems. Previously plants that operated with phosphate water treatment have adopted all volatile treatment (AVT) chemistry, which employs ammonia or other amines for pH control. The purpose of using amines instead of ammonia is to take advantage of their lower distribution coefficient in steam-water system. This property of amines provides a greater protection to the extraction lines, condensers, heater shells, etc. Amines are

less volatile when compared to ammonia in the secondary side of steam generators. Amines are used both in controlling pH and corrosion. In some cases addition of amines is known to reduce the transportation of dissolved iron into steam generators<sup>2</sup>. Many amines have been used till date in nuclear industry. Until 1993 many industries used morpholine to minimize corrosion in plants. But in 1993, CPSES investigated DMA chemistry, to accomplish several objectives like minimizing FAC, general corrosion and reduction in transport of soluble iron<sup>9</sup>.

The future sections discuss some of these amines used in the industry today and also their affect on the inconel alloy 600 and 690. Experiments carried out to understand the effect of amines on inconel alloy include:

- (1) Exposure of Inconel alloys 600 and 690 coupons to amine solution at high temperature and high pressure conditions for short oxidation times in an autoclave. AC and DC electrochemical techniques were used to study the reaction mechanism between amine and metal surface.
- (2) Scanning electron microscopy (SEM) and energy dispersive spectroscopy (EDS) were used to study the morphology and composition of the metal surface.

The following amines were studied for their effect on Inconel 600 and 690 metal surface at high temperature and pressure:

- 1) Morpholine: The chemical formula of morpholine is  $O(CH_2CH_2)_2NH$ . The chemical structure of morpholine is shown in the Figure 1.2a. Morpholine is basically used as neutralizing agent to control corrosion in nuclear power stations. This amine helps in adjusting pH and is more effective when used in combination with hydrazine or ammonia. Morpholine has proven to be an effective corrosion inhibitor and has been successfully used in steam generator systems<sup>2, 30</sup>.

2) ETA (ethanolamine): It is also called 2-aminoethanol or monoethanolamine. The chemical formula of ETA is  $C_2H_7NO$ . The chemical structure of ETA is shown in the Figure 1.2b.

3) DMA (dimethylamine): DMA is a secondary amine and its chemical formula is  $C_2H_7N$ . The chemical structure of DMA is shown in the Figure 1.2c.

4) DBU (1, 8-diazabicyclo [5.4.0] undec-7-ene): The chemical structure of DBU is  $C_9H_{16}N_2$  and the chemical structure is shown in Figure 1.2d. DBU is a tertiary amine. It is typically used as a catalyst for polyurethane.

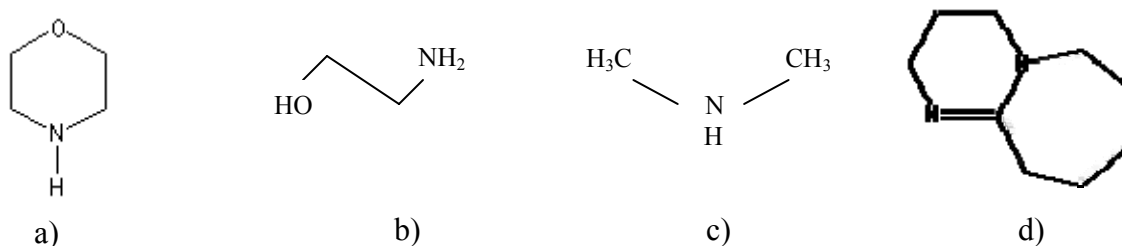


**Figure 1.2. Chemical structure of a) morpholine, b) ETA, c) DMA, and d) DBU**

In summary, attempts are made to understand the role of corrosion inhibitors used in power industry by characterization of corrosion products formed on different components of CPSES plant. In this research, samples collected from major components (condensers, high and low temperature feedwater heaters, moisture separator, etc.) of the plant over four scheduled outages were analyzed for oxide thickness and phases present using standard characterization tools including x-ray diffraction, infrared spectrophotometry, scanning electron microscopy, energy dispersive spectroscopy. In this process, a novel technique for iron oxides identification based on laser induced breakdown spectroscopy (LIBS) was developed to differentiate two major constituents of iron oxide corrosion products namely magnetite and maghemite. Microsecond temporal response of different iron oxides to a high-energy laser beam was utilized to identify



them. To further understand the mechanism of corrosion in steam generator alloys (alloy 600 and 690), electrochemical AC-impedance spectroscopy coupled with an autoclave was utilized to study oxidation mechanisms. Following chapters present literature review followed by oxide characterization, oxide quantification using FTIR, phase analysis using LIBS, electrochemical studies, and finally conclusions.

### 1.5. Chapter References

1. Varrin, Jr., "Characterization of PWR steam generator deposits", EPRI, TR-106048, Research Project S523-01, 1996.
2. Turner and Klimas, "The effect of alternative amines on the rate of boiler tube fouling", EPRI, TR-108004, September 1997.
3. "Qualification testing of three advanced amines for secondary system pH control in once-through steam generator plants", EPRI, TR-103098, March 1994.
4. Turner, "Identification and testing of amines for steam generator chemistry and deposit control", EPRI, TR-1002773, December 2002.
5. Frattini, "Surface chemistry interventions to control boiler tube fouling", EPRI, TR-110083, December 1999.
6. Gyung Guk Kim, Ji Hui Kim, Kwon Yeong Lee, Seon Jin Kim, Deok Hyun Lee, Do Haeng Hur, Myung Sik Choi, and Jung Ho Han, "Wear Behavior of Steam Generator Tubes in Nuclear Power Plant Operating Condition", Transactions of the 17<sup>th</sup> International Conference on Structural Mechanics in Reactor Technology, Prague, Czech Republic, August 17-22, 2003.
7. Billy Fellers, Chemistry Projects and Programs, TXU, Glenn Rose, TX. Interview by author, 17<sup>th</sup> December, 2002, Texas.

8. J. Stevens, B. Fellers, and Orbon, "S/G Deposit Control Program Assessment at Comanche Peak", Chimie 2002, Avignon, France, 2002.
9. B. Fellers, J. Stevens and G. Nichols, " Strategic elements of steam cycle control practices at TXU'S Comanche Peak steam electric station", Chimie 2002, Water Chemistry in Nuclear Reactors Systems, Avignon, France, 2002.
10. Nasrazadani and H. Namduri, "Characterization of Iron Oxide Deposits formed at Comanche Peak Steam Electric Station (CPSES)", Final Report, 2002.
11. Namduri, Haritha, "Characterization of Iron Oxide Deposits formed at Comanche Peak Steam Electric Station", Masters Thesis, University of North Texas, May 2003.
12. B. Sala, P. Combrade, R. Erre, and A. Gelpi, "Local Chemistry and Formation of Deposits on the Secondary Side of Steam Generators. A Laboratory Study", Sixth International Symposium on Environmental Degradation of Materials in Nuclear Power Systems-Water Reactors, San Diego, Aug 1-5, 1993.
13. Greene and Donaldson, "The role played by ion chromatography in the assessment of amines for two-phase erosion-corrosion control in nuclear electric's steam-water circuits", Journal of Chromatography, 640, 1993, 303-308.
14. Hur D.H. Hee Lee E. Sik Choi M. Sub Chung H. and Chul Kim U., "High temperature application of EDTA solvents for iron oxide removal", Journal of Nuclear Materials 299 (2001) 271-273.
15. J. Stevens, "Secondary System Oxide Characterization Study at Comanche Peak", 12<sup>th</sup> Annual Southwest Chemistry Workshop, July 2003, Dallas, TX.
16. Srikantiah and Chappidi, "Particle Deposition and Fouling in PWR Steam Generators", Nuclear Engineering and Design 200 (2000), pp. 285-294.

17. Wade, "Steam Generator Degradation and its Impact on Continued Operation of Pressurized Water Reactors in the United States", Energy Information Administration/ Electric Power Monthly, August 1995.
18. "Steam Generator Tube Issues", Fact Sheet, United States Nuclear Regulatory Commission, January 2004.
19. Cyrus and Maggi, "Steam Generator Deposit Trends and Characterization for Operating Nuclear Power Stations", Steam Generator Secondary Side Management Conference (2003), February 10-12.
20. "Flow-Associated Corrosion in Power Plants", EPRI (1998), Report No: TR-106611-R1.
21. Sadiq Shah, "Surface and Interface Characterization in Corrosion", NACE International, 1994, ISBN 1-877914-29-0.
22. Bloom, Deborah M. and Daniels, David, "Advance amines cut Condensate Corrosion", Power 145(2001)4, pp 81.
23. S.A. Salih, A.A. Mazhar, and H. Mahanny, "The effect of Sour Gases and some Anions on the Corrosion Behavior of Carbon Steel", Portugaliae Electrochimica Acta 22 (2004), pp. 205-225.
24. Mora-Mendoza and Turgoose, "Fe<sub>3</sub>C influence on the Corrosion Rate of Mild Steel in Aqueous CO<sub>2</sub> Systems under Turbulent flow Conditions", Corrosion Science 44 (2002), pp. 1223-1246.
25. David Jobe, "The calculated solubilities of hematite, magnetite and lepidocrocite in steam generator feed trains", AECL, 1997.

26. Bloom and Daniels, "Advance Amines cut Condensate Corrosion", Power 145 (2001), pp 81.
27. Marks and Varrin, "Application of Deposit Oxidation Models to Plant Practices: The Seabrook Example", Steam Generator Secondary Side Conference (2003), February 10-12.
28. Beverskog and Puigdomenech, "Pourbiax Diagrams for the Ternary System of Iron-Chromium-Nickel, Corrosion 55(1999).
29. "Pressurized Water Reactor Lead Source Book: Identification and Mitigation of Lead in PWR Secondary Systems, EPRI 2006, 1013385.
30. Frattini and Fruzzetti, "Protonation constant of Morpholine, Dimethylamine and Ethanolamine to 290C and the Effect of Morpholine and Dimethylamine on the surface charge of Magnetite at 150-250 C", EPRI, 1003179, November 2002.

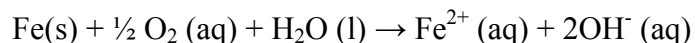
## CHAPTER 2

### LITERATURE REVIEW AND EXPERIMENTAL METHODOLOGY

#### 2.1. Fundamental Concepts of Corrosion in Ferrous Alloys

The destructive result due to chemical reaction between a metal or metal alloy and its environment is called corrosion. Corrosion results in converting the metal in the chemical compound to its original state from which the metal was actually extracted. Some researchers in the past have also called corrosion process as extractive metallurgy in reverse<sup>1</sup>. Aqueous corrosion processes that take place in metals are electrochemical.

Corrosion of carbon steel in steam generators occurs by a very complex mechanism, but it has generally been accepted that the corrosion of feed train begins when oxygen and/or water attacks the carbon steel surface. The following reactions indicate this phenomenon:



The release of  $\text{Fe}^{2+}$  can result in several corrosion products depending on the surrounding conditions. For example if the conditions are reducing,  $\text{Fe (OH)}$  could be found and if the conditions are oxidizing at higher temperature, can result in magnetite<sup>2, 3</sup>. The presence of certain anions like  $\text{CO}_3^{2-}$ ,  $\text{NO}_3^-$ ,  $\text{Cl}^-$ ,  $\text{SO}_4^{2-}$ , etc., have been found to have an effect on the oxidation mechanism of ferrous hydroxides for given pH and electrode potential of the solution<sup>4</sup>. For example iron combines with carbonate ions to form  $\text{FeCO}_3$  or siderite. It is known that siderite increases the electrochemical potential of tube materials to a level that it can increase the probability of stress corrosion cracking<sup>5</sup>. Ferric ions are most often associated with acidic aqueous environments and ferrous or ferric species in neutral or basic species.

### 2.1.1. Electric Double Layer Model in Metals

It is known from the past research that corrosion in aqueous solution involves electron or charge transfer. Any change in the electrochemical activity or potential on the metal surface can affect the corrosion rate. When in the contact with the aqueous solution, like water, the free electrons in the metal form a complex interface. The  $H^+$  and  $OH^-$  ions result due to dissociation of water and get attracted to the conductive metal surface, and form a solvent layer. The plane of positively charged cations closest to the negatively charged surface is called outer Helmholtz plane. This results in an interfacial structure of separated charges that is called electrical double layer. This double layer prevents easy charge transfer limiting electrochemical reactions at the metal surface. Figure 2.1 illustrates the processes taking place at the metal surface.

When a corrosion inhibitor is added to the above mentioned double layer, it changes the composition and structure of the double layer. The inhibitor molecules change the dielectric properties of water molecules in the electric double layer. Sometimes addition of the inhibitor may change capacitance of the double layer due to the formation of the inhibitor film<sup>6, 7</sup>.

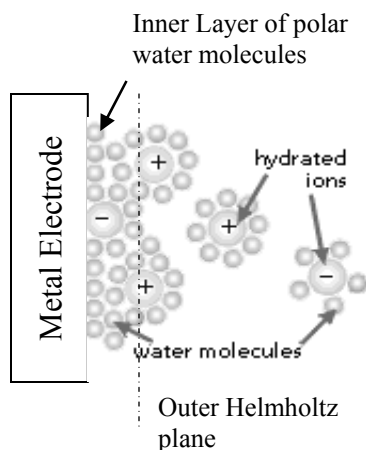


**Figure 2.1. Electrical double layer**  
(Adapted from Cornell and Schwertmann, 1996)

## 2.2. Iron Oxides and Hydroxides

Iron oxides and oxyhydroxides generally referred to as iron oxides have various applications such as pigments, catalysts, magnetic materials, sensors, etc<sup>9</sup>. One of the characteristics of the iron oxide system is the variety of possible transformations between the different phases. The most commonly occurring phases of iron oxides in power plants are given in Table 2.1. Iron oxides exhibit a wide variety of crystal morphologies and crystalline sizes both in their man-made and natural forms.

**Table 2.1. Eight forms of iron oxides and oxyhydroxides**

Oxyhydroxides		Oxides	
Formula	Name	Formula	Name
$\alpha$ -FeOOH	Goethite	$\text{Fe}_5\text{OH}_8 \cdot 4\text{H}_2\text{O}$	Ferrihydrite
$\beta$ -FeOOH	Akaganite	$\alpha$ - $\text{Fe}_2\text{O}_3$	Hematite
$\gamma$ -FeOOH	Lepidocrocite	$\gamma$ - $\text{Fe}_2\text{O}_3$	Maghemite
$\delta$ -FeOOH	Ferroxhyte	$\text{Fe}_3\text{O}_4$	Magnetite

Hematite, magnetite and maghemite are the most prevalent iron oxides found in steam generators. Other forms of iron oxyhydroxides can exist depending on the thermodynamic conditions present in the secondary cycle of pressurized water reactor. The presence of hematite could also be due to “weathering” of the sample during collection, storage, handling, or exposure of secondary side to oxidants during refueling outages.

One more reason to justify characterizing iron oxides is the existence of substituted spinels. Substituted spinels are formed when octahedral  $\text{Fe}^{3+}$  ion sites are substituted by nickel,

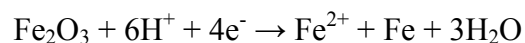
aluminum or silicon. Some of these spinels include  $\text{Fe}_{2.76}\text{Al}_{0.2}\text{O}_4$  (substituted magnetite) and multi element spinels like  $\text{Fe}^{3+}(\text{Cr}_2)\text{Fe}^{2+}(\text{Ni}, \text{Mn}, \text{Zn})\text{O}_4$ <sup>10</sup>.

### 2.2.1. Dissolution Kinetics of Iron Oxides

In the past researchers have shown that the dissolution rate of iron oxides depends on the presence of reducing agents. For example, presence of certain aggressive reducing species can result in dissolving the protective layer of iron oxide on the metal surface. The dissolution mechanism can also be affected by the addition of sulfur containing compounds and ascorbic acid. This is because the additives added to the system may form complexes at the metal surface and can result in ligand to metal electron transfer<sup>11</sup>. Iron oxyhydroxides are known to be strong absorbents of heavy metals. When these oxyhydroxides are dissolved in reducing conditions, metals are released in an aqueous medium. The solubility of magnetite decreases with increasing pH and temperature. Many models have been developed to explain the interactions between the solution and the metal interface<sup>12</sup>. Electrical double layer theory explained in previous section is one of the theories modeled to explain dissolution mechanism in metals. Garcell and group showed that when maghemite is suspended in aqueous solution, the charging that results involves complex reactions and the interfacial properties of the aqueous solution is similar to that of magnetite suspended in aqueous solution<sup>13</sup>.

Ogura and Sato studied the cathodic dissolution of the passive film on iron<sup>14</sup>. Their paper mentioned the work done by Agius and Siejka, who found that electronic charge of 1.38e associated with each ion of oxygen passing into the solution during cathodic protection of passive ion. Ogura and Majima further explained the value of 1.38e electronic charge mechanism, which is pH dependent using the following equation:





In the year 2002, Chastukhin and group studied the dissolution kinetics of magnetite and hematite in HCl and H<sub>2</sub>SO<sub>4</sub> solutions at different concentrations and under different temperatures. They also studied the effect of oxide synthesis on the dissolution mechanism of the above mentioned iron oxides using chain mechanism model. From their study they concluded that the dissolution kinetics of iron oxides is depended on the difference between the concentrations of the dislocations and other defects on the particle surface<sup>15</sup>.

Atenas and Mielcazski studied oxidation reaction of iron in aqueous solutions. They studied the effect of the particle surface, structure and composition of the surface on dissolution mechanism of iron in air and aqueous solution<sup>16</sup>.

### 2.2.2. Phase Transformation

One of the characteristic of the iron oxide system is the variety of possible transformation between the different phases. Corrosion products on steel components include: a) common iron oxides such as magnetite, hematite and maghemite and b) iron oxyhydroxides and c) iron hydroxides. The concentration of precursor iron species in the feedwater is typically 2 to 10 ppb which is below the solubility limit of Fe<sub>3</sub>O<sub>4</sub> (magnetite) in water at both 300°C and 60°C. The solubility of magnetite decreases with increasing pH and increasing temperature. Although iron oxides are in principle simple inorganic compounds, they exhibit a wide range of crystal morphologies both in their man-made and natural forms<sup>8, 10</sup>.

The presence of maghemite (γ-Fe<sub>2</sub>O<sub>3</sub>) and hematite (α-Fe<sub>2</sub>O<sub>3</sub>) or even the presence of iron oxyhydroxides such as α-FeOOH and γ-FeOOH can promote formation of copper oxides when compared to highly reduced magnetite (Fe<sub>3</sub>O<sub>4</sub>). Characterization of deposit samples

including the oxide phase can give very valuable information on the plant operations and maintenance.

Studies performed by Nasrazadani and Raman have showed that transformation of magnetite to hematite goes through the formation of maghemite<sup>17</sup>. Detailed information on iron oxide transformation is given in Figure 2.2. The amount of iron transported in steam generator is dependent on the composition of iron oxides formed in the feed train. Deposits that contain well crystallized magnetite and maghemite are more stable than deposits containing combination of an oxyhydroxides and oxides. The production of maghemite begins with nucleation and growth of goethite or lepidocrocite, followed by dehydration to hematite and then reduction to magnetite<sup>18</sup>.

Magnetite is a well known form of iron oxide that forms both at room temperature in crevices between steel plates at elevated temperature inside boiler tubes, heat exchangers etc. The oxidation product of  $\text{Fe}_3\text{O}_4$  is either  $\gamma\text{-Fe}_2\text{O}_3$  or  $\alpha\text{-Fe}_2\text{O}_3$  depending on the oxidation temperature and or possibly crystallite size of the starting magnetite. Taylor observed that changing the ratio of  $\text{Cl} / \text{Fe}$  during the oxidation of  $\text{Fe}(\text{II})$  chloride changes not only favors the formation of lepidocrocite over magnetite but also affects the crystallinity of lepidocrocite<sup>19, 20</sup>.

Before Meillon's work the transformation from maghemite to hematite was thought to be irreversible. But Meillon and group showed that direct phase transformation takes place from hematite to maghemite by wet grinding of hematite particles in ethanol. The transformation of oxygen framework and iron coordination from HCP to cubic close packing is due to shearing motion caused by wet grinding<sup>21</sup>. Finch and Sinha observed in electron diffraction study, the formation of epitaxial layer of maghemite on pure hematite particles on heating above  $700^\circ\text{C}$ . According to the authors the hematite formed was created via an intermediate state  $\beta\text{-Fe}_2\text{O}_3$ <sup>22</sup>.

Boer and Dekkers performed thermo-magnetic analysis of different types of hematite and concluded that the transformation from hematite to maghemite can occur under suitable

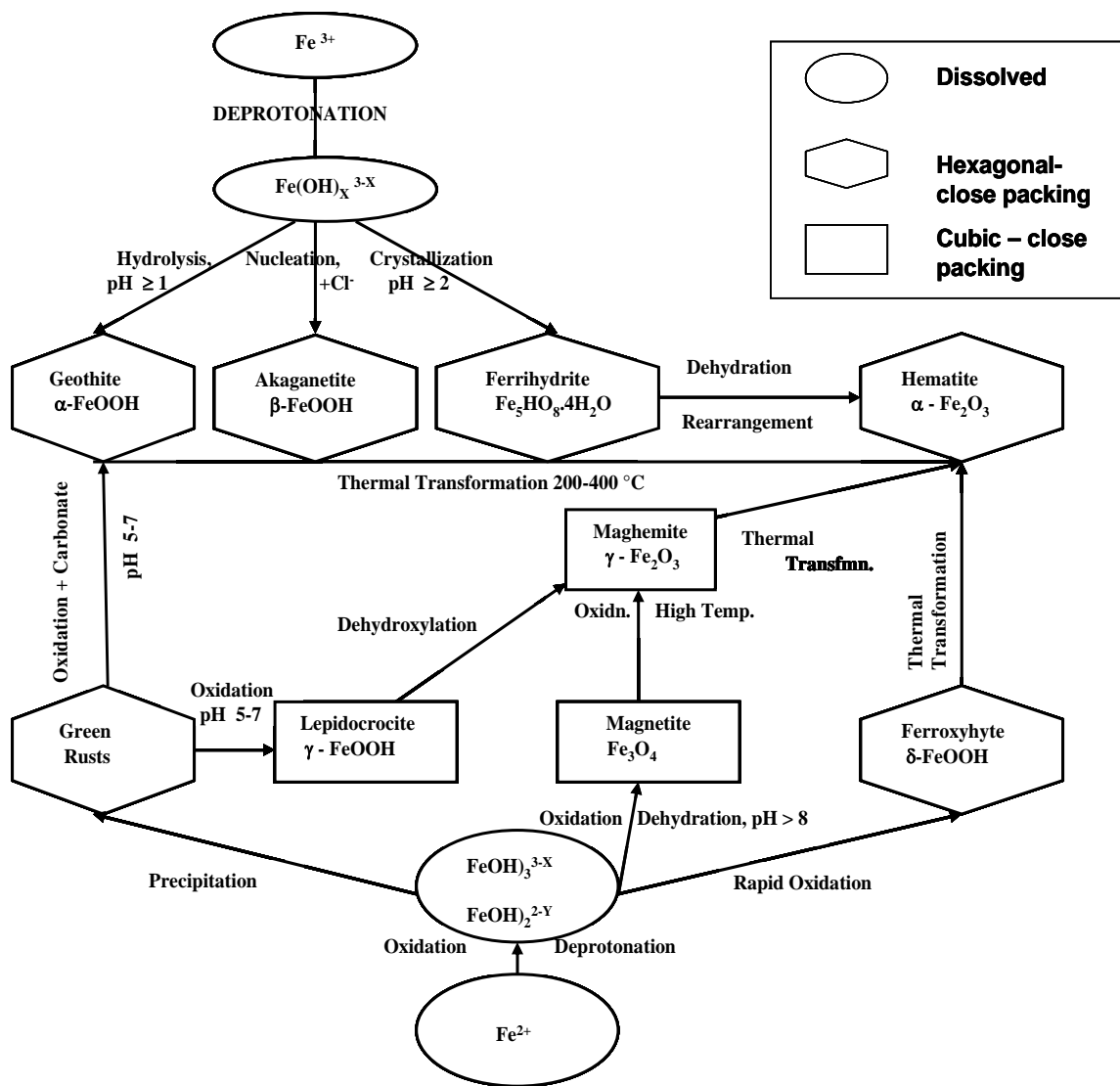


**Figure 2.2. Phase transformation in iron oxides**  
(Reproduced with Permission from Varrin, 1996)

conditions<sup>23</sup>. Randrianantoandro and group also performed similar studies using high energy ball milling<sup>24</sup>. Alcalá and group used micron sized iron and hematite powders to synthesize nanocrystalline magnetite by mechanical alloying<sup>25</sup>.

### 2.2.3. Crystal Structure and Morphology

The structure of iron oxides in general can be described as combination of close packed oxygen atoms and interstitial octahedral and/or tetrahedral sites occupied by iron atoms<sup>26</sup>. The properties of iron oxides such as magnetic and dissolution behavior may be influenced by crystal morphology (growth form) and crystal size. The mechanism of growth and the resulting crystal morphology depends upon solution conditions, in particular the super saturation and also on the structure of the growing crystal surface. Crystal size of the iron oxide reflects the growth conditions and determines the surface area which in turn is important for all types of surface reactions. Usually the crystal size of iron oxides lies in the range of 7 nm to few millimeters<sup>27</sup>. The crystal structure of three iron oxides that are found in steam generator cycle systems is explained in next part of this section.

a) Magnetite: Magnetite is a well known form of iron oxide that forms both at room temperature and also at elevated temperature. Magnetite is a mixed valence iron oxide containing  $\text{Fe}^{2+}$  and  $\text{Fe}^{3+}$  ions in an inverse spinel structure. In each unit cell of magnetite, there are 32 oxygen ions located in close packed planes.  $\text{Fe}^{3+}$  ions occupy eight tetrahedral interstitial sites and eight octahedral sites, whereas  $\text{Fe}^{2+}$  ions occupy eight octahedral sites. Spherical particles are formed when  $\text{Fe}^{2+}$  is in excess over  $\text{OH}^-$  whereas with excess  $\text{OH}^-$ , cubic crystals are formed<sup>28, 29</sup>.

b) Maghemite: Maghemite has similar spinel structure to that of magnetite except that  $2\frac{1}{3}$  sites are occupied by  $\text{Fe}^{3+}$  ions and  $\frac{8}{3}$  sites are cation vacancies. Maghemite is usually formed

by transformation from another iron oxide or iron compound and almost always adopts the morphology of precursor. Porous acicular crystals of maghemite with as long axis form as a result of transformation series involving dehydroxidation of  $\alpha$ -FeOOH to hematite, reduction of hematite to magnetite and finally oxidation to maghemite<sup>30,31</sup>.

c) Hematite: Hematite is rhombohedral in crystal structure where the  $\text{Fe}^{3+}$  cations are located in distorted oxygen octahedra of the rhombohedral lattice. Hematite is typically in rhombohedral, platy and rounded in structure. The plates can vary in thickness and can be round, hexagonal or irregular in shape. Plates of micaceous hematite up to 50  $\mu\text{m}$  across are formed by high temperature oxidation of molten  $\text{Fe}^{3+}$  chloride complexes. Round hematite single crystals upto 800  $\mu\text{m}$  across are formed by chemical vapor transport at elevated temperatures. At higher temperatures these crystals sinter to irregular masses<sup>8</sup>.

When the particle size decreases, the fraction of atoms which lie near the surface increases. Lattice parameter and crystalline size are related by the surface influence (surface stress and energy). Since lattice parameter with variation with grain size cannot be studied, the properties like adsorption, stoichiometry, phase etc. are studied<sup>2</sup>.

Iron (III) oxides and hydroxides are products of forced hydrolysis of  $\text{Fe}^{3+}$  ions. The phase, size and shape of the iron oxide particles depend on the  $\text{FeCl}_3$  and  $\text{HCl}$  concentrations, pH, the presence of complexing agent, temperature and time when produced by forced hydrolysis of  $\text{Fe}^{3+}$  ions. Music and group cited various studies where the size of iron oxide particles depended on the amines and metal ions present in the solution. For example the presence of low concentration metal ions like  $\text{Cu}^{2+}$  in  $\text{FeCl}_3$  hydrolysing solution resulted in inhibiting the growth of  $\beta$ -FeOOH particles. But when the concentration of the metal ions was increased, it resulted in the increase in the growth of  $\beta$ -FeOOH particles<sup>32</sup>.

Schimanke and Martin studied the transition of nanocrystalline maghemite to hematite using XRD. From previous studies it is known that coarse grained maghemite transforms to hematite at temperature above 300°C. It has also been observed that nanocrystalline magnetite produced using reverse micelle method that below a crystal size of 30 nm only maghemite was produced whereas above this size only hematite was produced <sup>33</sup>.

Ayyub and his group discussed the thermodynamics involved in grain size and size dependent phase transitions in iron oxides. They showed that the grain size affects the phase transformation in oxides and called it “size driven phase transition” <sup>34</sup>.

#### 2.2.4. Characterization of Iron Oxides

Different analytical techniques have been used in past to characterize iron oxides. One of the techniques which is widely used in characterizing iron oxide deposits is x-ray diffraction (XRD) <sup>35, 36</sup>. The limitation that XRD poses in characterization of iron oxides is that it cannot efficiently differentiate between magnetite and maghemite. Magnetite and maghemite have similar spinel structure and this makes it difficult to distinguish them using an ordinary XRD. Magnetite is said to have a defect structure with Fe:O ratio that ranges from 0.75 to 0.744. This results in variation of lattice parameter  $a$  from 8.397 to 8.394 Å. Similarly in maghemite, the Fe:O ratio ranges from 0.67-0.72. This results in the variation of lattice parameter  $a$  from 8.33 to 8.38 Å. The small difference in the lattice parameter makes it difficult for ordinary XRD to distinguish between  $\text{Fe}_3\text{O}_4$  and  $\gamma\text{-Fe}_2\text{O}_3$  (Figure 2.3). Another technique that has been used in past to study iron oxides is Mossbauer spectroscopy (MS). This technique is very sensitive in identifying iron oxides but has known to encounter problems in analyzing complex mixtures containing more than one spinel structure. It has been established that FTIR can be used to

efficiently characterize iron oxides. FTIR spectra of oxidized magnetite samples are known to show five absorption bands indicating the different degrees of oxidation and cation vacancy contents of spinel phase<sup>37, 38</sup>. Characterization of iron oxides using FTIR is discussed in detail in chapters 4 and 5.

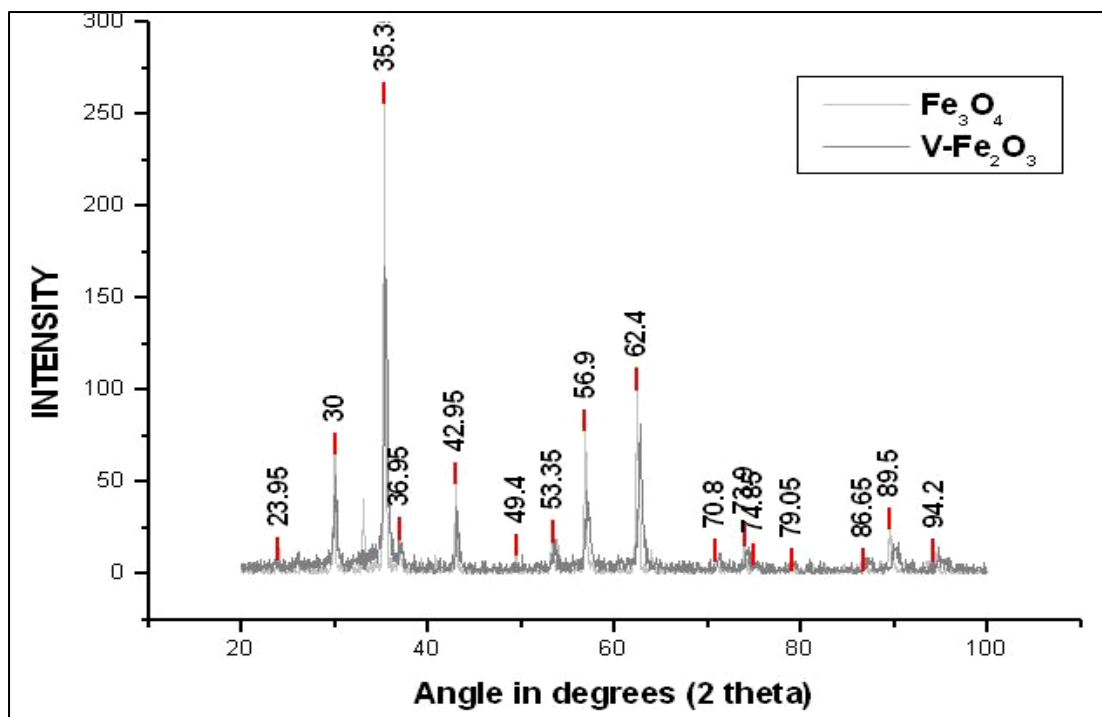


**Figure 2.3. XRD spectra of – synthetic magnetite ( $\text{Fe}_3\text{O}_4$ ) and maghemite ( $\gamma\text{-Fe}_2\text{O}_3$ ) powders**  
(Source: Namduri, MS Thesis, 2003)

### 2.3. Effect of Amines on Iron Oxides

Inhibitors protect the metal by adsorbing onto the surface and reduce corrosion of metal in aggressive environment. So selection of appropriate amine is a very important and this justifies the study of amines and their effectiveness in high temperature and corrosive pressure

environment. Amines study is also important owing to the fact that they effect the corrosion deposits formed in steam generators cycles and also the phase transformation of iron oxides.

There are different kinds of amines: volatile, neutralizing, steam volatile film forming etc. For example volatile amines are added to feed water systems to increase the pH of the water and thereby control corrosion. These amines combine with steam and are carried to turbine and condensers and other parts of secondary side of steam generator, protecting them from corroding under steam-water circuits. Amines have not only been widely used as corrosion inhibitors in nuclear power industry, but have also been used in gas and oil, paper, cooling circuits and many other industries<sup>40, 41</sup>.

In the past, researchers have extensively studied the effects of amines as corrosion inhibitors. Studies have also been performed to understand the mechanism at the metal surface when the metal is exposed to amine solution. This present research mainly focuses on the amines used in nuclear power plants. A new amine DBU (1, 8-diazabicyclo [5.4.0] undec-7-ene) has been studied for its effectiveness as corrosion inhibitor along with commonly used amines in the power industry. The amines used in this research are DBU, DMA, ETA and morpholine. Along with the above mentioned amines, inconel alloy was also exposed to NaOH solution, which would be referred to as control sample in the rest of the report. One of the goals of this research is not only to study the effects of these amines on the metal surface, but also to compare the effectiveness of DBU as corrosion inhibitor to the rest of the amines, which are well established as corrosion inhibitors in the power industry<sup>42-44</sup>.

Hur's group studied the sludge dissolution kinetics and corrosion of materials by using EDTA as a solvent at temperature ranges of 93-150 °C. They observed that the magnetite dissolution increased as the temperature was increased<sup>45</sup>. Ocha's group studied the inhibition



efficiency of fatty amines in combination with phosphonocarboxylic acid and biocide on carbon steel metal surface in a water treatment cooling circuit using electrochemical impedance measurements. They concluded that the phosphonocarboxylic acid salts acted as anodic inhibitors whereas the fatty amines showed mixed reaction. From X-ray photoelectron spectroscopy they also found that the layer formed on the metal surface comprised of an iron oxide and hydroxide mixture along with some complex organic compounds, showing that the organic molecules interact with the iron oxide at the metal and the oxide interface<sup>46</sup>. Olsson et al. have studied the adsorption of carboxylic acid-based inhibitors. They showed that the inhibitor efficiency is dependent on the nature and the concentration of the anions in the solution<sup>47</sup>. Ishikawa and his group studied the effects of amines on formation of iron hydroxides. From the XRD and Infrared analysis they concluded that the crystal phase of air-oxidation products depends on the  $pK_a$  of the amines used in the solution. They were also successful in showing that the transformation of  $\alpha$ -FeOOH to  $\gamma$ -FeOOH was dependent on the  $pK_a$  of the amine<sup>48</sup>. The same group also studied the effect of amines on the formation of  $\beta$ -FeOOH. They showed that the particle size of the hydroxide formed decreased with increase in the concentration of the amine. They were also able to show that certain amines had more effect on the size of hydroxide compared to the other amines used in the study<sup>49</sup>.

Study performed by Bouayed and group on corrosion inhibition of organic compounds on metallic iron surface made an attempt to compare the efficiency of three amines, thiophenol, phenol and aniline. They performed gravimetric and electrochemical experiments to study the bonding interaction between the molecules of the organic compound and the metal surface<sup>50</sup>.

Alkylamines are known to inhibit corrosion on metal (iron) surface by absorbing chemically on the metal surface. Tsuji and his group used FTIR, contact angle measurement and

XPS techniques to study the protective efficiency of N, N –dimethylalkylamine monolayer modified with chlorosilanes for preventing corrosion of iron <sup>51</sup>.

Typically the corrosion product layer on an uninhibited metal is in the order of microns, but the presence of corrosion inhibitor, the inhibitor film is at molecular level whereas the corrosion layer is on a microscopic level<sup>52, 53</sup>.

The corrosion inhibition efficiency of the amine is mainly dependent on the adsorption mechanism of the amine on the metal surface. This occurs when the organic inhibitor molecule replaces the moisture between the organic coating and the metal oxide surface<sup>54</sup>.

To summarize the amines possibly affect the iron oxide particle size and phase transformation. Addition of amines can also affect the porosity of the corrosion scale on the tube surface, scale adhesion, pH and water chemistry in the secondary side of steam generator system.

#### 2.4. Prevention of Corrosion - Role of Protective Oxide Films

The composition and structure of the oxide film determines how different ions are transported through the oxides. This transport of material affects the corrosion rate. The main constituents of alloy 600 and 690 are nickel, chromium and iron. At typical secondary side conditions, nickel, chromium and iron are more stable as oxides than as metals. These elements form thin protective oxide (typically less than 1  $\mu\text{m}$  thick) on the metal surface and reduce the reaction rate of the base metal. One of the main disadvantages of using material that relies on protective film for corrosion resistance is that it makes the material susceptible to modes of corrosion that can affect the integrity of the films.

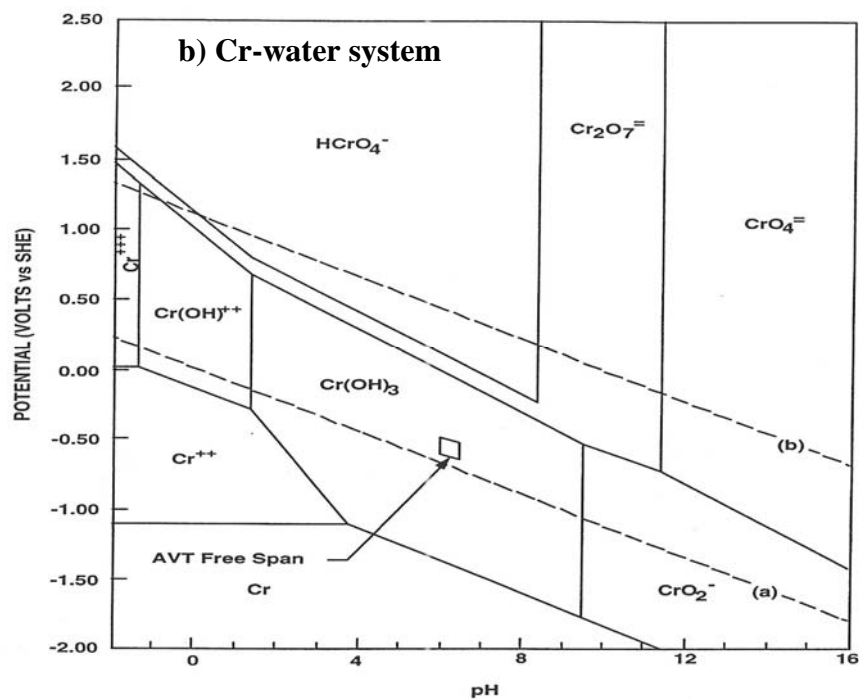
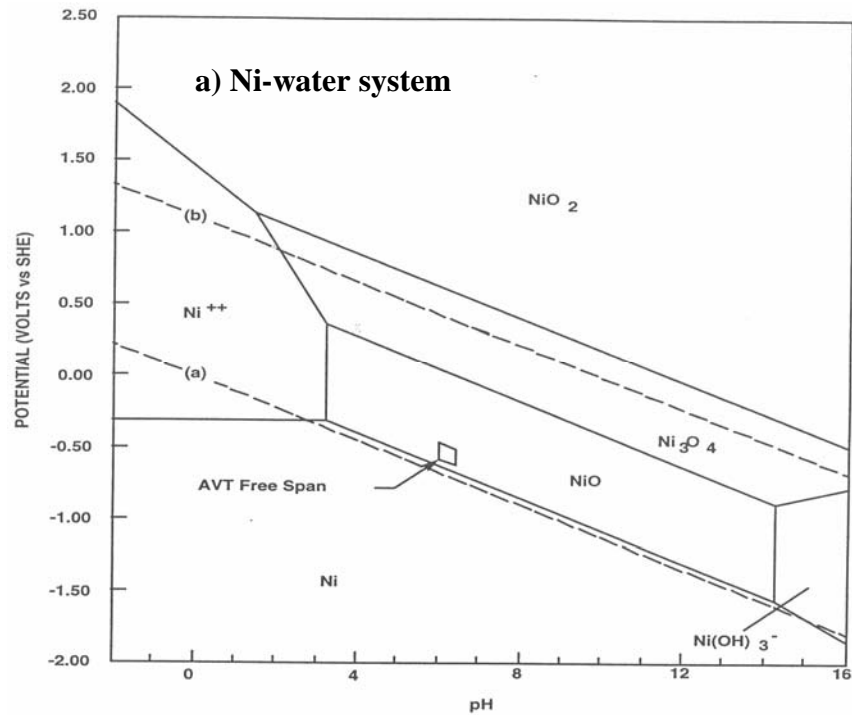
Past researchers have shown that maghemite layer is responsible for passivity in iron. Even though magnetite provides the basis for formation of higher oxidation state but does not

directly contribute to the passivity. Iron is more difficult to passivate than nickel because in iron it is not possible to directly create conditions to form maghemite. First steps have to be taken to form a stable layer of magnetite for a period of time and only then can the conditions can be amicable for formation of a passivating layer of maghemite. In case of nickel,  $\text{Ni}^{2+}$  oxide considered to be  $\text{NiO}$  along with  $\text{Ni}(\text{OH})_2$ , which is the passivating species, does not require any initial oxidation state like iron<sup>55</sup>.

Pourbaix diagrams indicate graphically the conditions of redox potential and pH under which different types of corrosion behavior may be expected. These plots indicate regions of thermodynamic stability of different phases and species of metals and oxides. The potential on the vertical axis is determined by the concentrations of oxygen, hydrogen and other oxidizing and reducing species. Figure 2.4 a shows the stable phases for nickel-water system. The line (a) in this figure indicates the stability region of water and line (b) indicates  $\text{O}_2\text{-H}_2\text{O}$  (oxygen) line. The wetted tube surface conditions are normally between the lines (a) and (b). The regions where free span areas in the steam generator are exposed to All Volatile Treatment (AVT) water operate is also indicated in this figure. One of the observations from the Pourbaix plot of nickel is that the stable form of oxide under AVT conditions is nickel oxide which forms a protective oxide layer on the metal surface. Figure 2.4 b and c show the Pourbaix plots for chromium and iron. In the low potential range where the metal will not corrode in the sense of dissolving but still can be damaged by corrosion processes such as hydrogen embrittlement.

The deposition rate of hematite ( $\alpha\text{-Fe}_2\text{O}_3$ ) is an order of magnitude greater than magnetite ( $\text{Fe}_3\text{O}_4$ ). As seen from the pourbaix diagram of iron, it is important that the reducing conditions be maintained in the steam generators during operation so as to facilitate formation of magnetite. Turner and Klimas showed that lowering the concentration of hematite relatively to magnetite in

the feedwater will significantly lower the rate of tube bundle fouling. Theoretical studies by Jobe showed that magnetite has a very low solubility and a much smaller dissolution rate



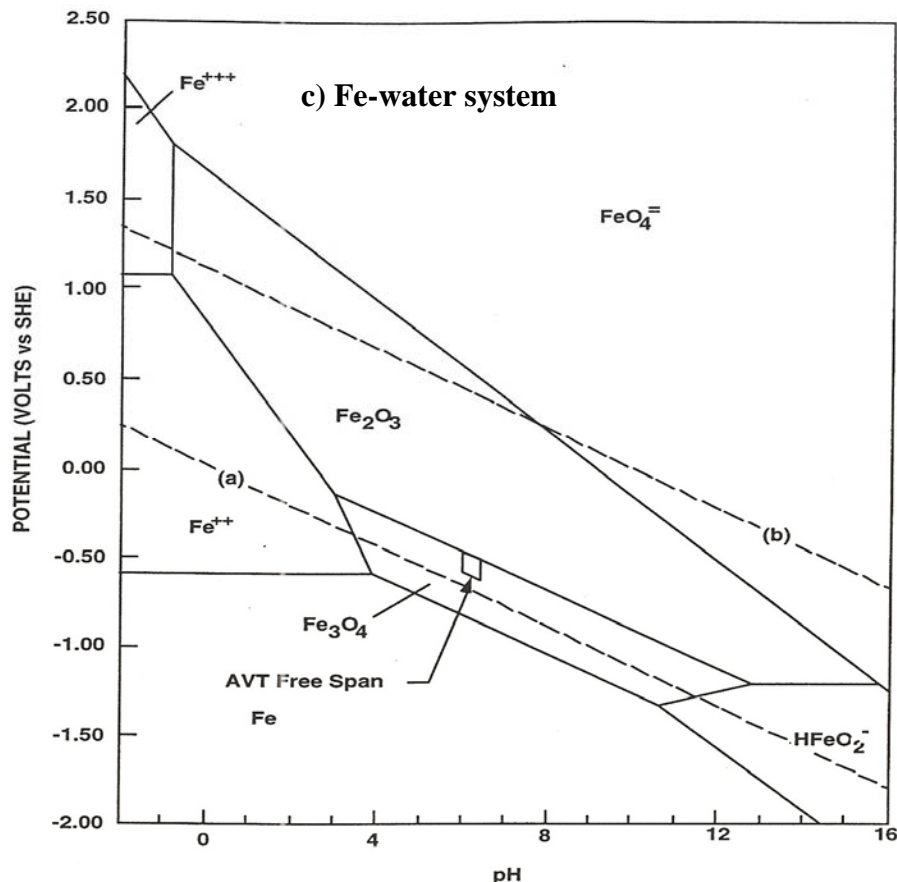


**Figure 2.4 Pourbaix (potential-pH) diagrams for a) nickel-water, b) chromium-water and c) iron-water systems at 288°C (dissolved species activities of  $10^{-3}$  (Reproduced with permission from EPRI, TR-108004)**

than magnetite and lepidocrocite in the presence of 5 ppb of dissolved oxygen. At low pH, Fe(II) species dominate; the total iron solubility is lower for  $\text{Fe}_3\text{O}_4 + \alpha\text{-Fe}_2\text{O}_3$  than  $\text{Fe}_3\text{O}_4 + \text{H}_2$  couple. At high pH, Fe(III) species dominate and the total solubility is higher for the  $\text{Fe}_3\text{O}_4 + \alpha\text{-Fe}_2\text{O}_3$  couple. Solubility of magnetite under reducing conditions may exceed the solubility of  $\gamma\text{-FeOOH}$  under oxidizing conditions at temperatures greater than 185°C. So when hydrazine is added to the system, the sudden shift in the redox reaction may cause the soluble iron concentration to exceed the solubility of  $\text{Fe}_3\text{O}_4$  and force it to precipitate out<sup>2</sup>. Formation of thin layer of maghemite/magnetite is known to act as a very good passive film. The two most prevalent views of passive films on nickel are that it is either entirely NiO or it consists of inner

layer of NiO and an outer layer of Ni(OH)<sub>2</sub>. Addition of chromium can alter the oxide film composition and structure formed on the metal surface. This can result in more disordered (less crystalline) form of oxide film. In other words it can result in formation of an amorphous or less crystalline oxide film which may be more resistant to breakdown compared to crystalline film<sup>6</sup>.

Sulfur is known to adsorb on the magnetite surface (present in steam generator deposits) and possibly reduce to sulfides. This is an important reaction because in past sulfur has been associated with tube corrosion. Presence of nickel in the steam generator system has been found to catalyze Schikorr reaction and result in magnetite on the tube surface. Sulfur can also react with nickel to form nickel sulfides and result in sulfur induced corrosion in secondary side<sup>10</sup>.

Lemire and McRae showed that for alloy 690 under basic oxidizing conditions (pH 8-10) at 573 K, the equilibrium concentration of chromium is higher than that of nickel and iron. They suggested that this could result in leaching of chromium and the oxide surface may contain oxides of iron and nickel. At reducing conditions, the chromium solids are less susceptible to dissolution than those of iron and nickel<sup>56</sup>.

## 2.5. Experimental Methodology

a) Scanning electron microscopy (SEM): SEM is a tool that is widely used in characterization and analysis of materials. The SEM has a resolution which approaches few nanometers and can operate at magnifications in the range of 10-300,000 X. SEM combined with EDS (energy dispersive spectroscopy) can give very valuable chemical and morphological information. SEM is relatively inexpensive when compared to other analytical tools for the wide range of information that it can provide<sup>57</sup>. In the present research SEM has not only been used to study the

morphology of the iron oxides and inconel alloy surface, but also to study the thickness of iron oxide formed on the samples collected from CPSES.

b) Energy dispersive spectroscopy (EDS): EDS combined with SEM can give very valuable chemical information of the specimen. x-rays are produced as a result of ionization of an atom. An inner shell electron is removed and an electron from higher energy level fills the vacancy created by inner electron shell. This process involves emission of excess energy, which is unique for every inner electron shell. This process involves emission of excess energy, which is unique for every atomic transition, which is in the form of x-ray photon or self absorbed or emitted as an auger electron. Even though the sensitivity of EDS is very low for light elements, it is still a powerful analytical technique for a quick and efficient qualitative survey of the elements present in the sample<sup>57</sup>.

c) X-Ray diffraction (XRD): XRD is used to identify crystalline phases present in a material. It is also used to measure the structural properties, grain size, phase composition, epitaxy, preferred orientation, and defect structure for a given specimen. The main limitation of this technique is that it can be used only for crystalline materials<sup>58</sup>. For a single crystal there is only one orientation (hkl) plane where Bragg's law is satisfied. This relation can therefore be used to study the crystal phase, phase transformation, defect structure of a given specimen.

d) Fourier transform infrared spectroscopy (FTIR): It is one of the few non-destructive techniques which can provide information regarding chemical bonding in a material. It is not only used to analyze solid samples but can also be used for liquid samples. The goal of basic infrared experiment is to determine the changes in the intensity of a beam of infrared radiation as a function of wavelength or frequency after it interacts with the sample. The intensity –time

output of the interferometer must be subjected to Fourier transform to convert it into the familiar infrared spectroscopy<sup>59</sup>.

e) Laser induced breakdown spectroscopy (LIBS): In recent years LIBS has been extensively used in the field for elemental analysis due to its advantages which include speed of analysis, simplicity, and capability. It is also a very inexpensive technique to use in the field<sup>60</sup>. The output obtained from LIBS can give very valuable information on the elemental composition and concentrations of the sample under analysis.

f) Electrochemical impedance spectroscopy (EIS): Electrochemical techniques have been used extensively in past for studying the kinetic and mechanism at the metal-oxide interface. The wide application of amines as corrosion inhibitors has further attracted interest in studying the reaction mechanism of these amines at the metal oxide interface. Polarization (DC technique) and impedance (AC technique) methods are the most widely used electrochemical techniques in studying the kinetics between the organic molecules and the oxide layer formed on the metal surface in a corroding environment. Electrochemical impedance spectroscopy (EIS), which is an AC technique, is capable of producing valid measurements of polarization resistance ( $R_p$ ) and corrosion rate from the corrected solution resistance.

## 2.6. Chapter References

1. J.H. Payer, W.K. Boyd, D.G. Lippold, and W.H. Fisher, "NBS-Battelle cost of corrosion study (70 billion!)", Materials Performance, May 1980.
2. David Jobe, "The calculated solubilities of hematite, magnetite and lepidocrocite in steam generator feed trains", AECL, 1997.



3. Bloom, Deborah M. and Daniels, David, “Advance amines cut Condensate Corrosion”, *Power* 145 (2001) 4, pp. 81.
4. Olowe and Génin, “The Mechanism of Oxidation of Ferrous Hydroxide in Sulphated Aqueous Media: Importance of the Initial Ratio of the Reactants”, *Corrosion Science* 32 (1991)9, pp. 965-984.
5. Schneider, V., W. Ruhle, and R. Riess, “Magnetite Deposition in PWR Secondary Systems”, *VGB-Kraftswerktechnik GmbH, Essen* 80(2000)11.
6. Marcus P., and Oudar J., “Corrosion Mechanism in Theory and Practice”, Marcel Dekker, Inc., New york, 1995, ISBN – 0-8247-9592-X.
7. Frattini and Fruzzetti, “Protonation constant of Morpholine, Dimethylamine and Ethanolamine to 290°C and the Effect of Morpholine and Dimethylamine on the surface charge of Magnetite at 150-250°C”, EPRI, 1003179, November 2002.
8. Cornell and Schwertmann, “The Iron Oxides - Structures, Properties, Reactions, Occurrence and Uses”, VCH Publishers, New York, 1996, ISBN – 3-527-28576-8.
9. Sudakar C., Subanna G. N., Kutty T. R. N., “Effect of Anions on the Phase Stability of  $\gamma$ -FeOOH nanoparticles and the Magnetic Properties of Gamma –Ferric Oxide Derived from Lepidocrocite”, *Journal of Physics and Chemistry of Solids* 64 (2003), pp. 2337-2349.
10. Varrin, Jr., “Characterization of PWR steam generator deposits”, EPRI, TR-106048, Research Project S523-01, 1996.
11. R. Torres, M. A. Blesa, and E. Matijevic, “Interactions of Metal Hydrous Oxides with Chelating Agents. IX. Reductive Dissolution of Hematite and Magnetite by Aminocarboxylic Acids”, *Journal of Colloid and Interface Science*, 134 (1990) 2, pp. 475-485.

12. Davranche and Bollinger, "A Desorption-Dissolution Model for Metal Release from Polluted Soil under Reductive Conditions", *Journal of Environmental Quality* 30 (2001), pp. 1581-1586.
13. Garcell L, Morales MP, Andres-Verges M, Tartaj P, and Serna CJ "Interfacial and Rheological Characteristics of Maghemite Aqueous Solutions", *Journal of Colloid and Interface Science* 205 (1998) 2, pp. 470-475.
14. Ogura and Sato, "Cathodic Dissolution of the Passive Film on Iron – I. Kinetics and Mechanism", *Electrochimica Acta* 25 (1979), pp. 857-862.
15. Chastukhin A.E., Izotov A.D., Gorichev I.G., and Kutepov A.M, "Analysis of  $\text{Fe}_2\text{O}_3$  and  $\text{Fe}_3\text{O}_4$  Dissolution Kinetics in Terms of the Chain Mechanism Model", *Theoretical Foundations of Chemical Engineering* 37(2003) 4, pp. 398-406.
16. Atenas and Mielczarski, "Some Aspects about Iron Oxidation Reaction in Aqueous Solutions", *Cabierta, Universidad De Chile*, Vol. 23, ISSN: 0717 8948.
17. Nasrazadani and Raman, "The Application of Infrared Spectroscopy to the study of Rust Systems-II. Study of Cation Deficiency in Magnetite ( $\text{Fe}_3\text{O}_4$ ) Produced During its Transformation to Maghemite ( $\gamma\text{-Fe}_2\text{O}_3$ ) and Hematite ( $\alpha\text{-Fe}_2\text{O}_3$ )", *Corrosion Science* 34 (1993) 8, pp.1355-1365.
18. Domingo and Clementa, "The Pathways to Spinel Iron Oxides by Oxidation of Iron (II) in Basic Media", *Materials Research Bulletin* 26 (1991), pp. 47-55.
19. Taylor, "Influence of Chloride on the Formation of Iron Oxides form Fe (II) Chloride. II. Effect of  $[\text{Cl}^-]$  on the Formation of Lepidocrocite and its Crystallinity", *Clays and Clay Minerals* 32 (1984) 3, pp. 175-180.

20. Taylor, "Influence of Chloride on the Formation of Iron Oxides from Fe (II) Chloride. I. Effect of  $[Cl^-]/[Fe]$  on the Formation of Magnetite", *Clays and Clay Minerals* 32 (1984) 3, pp. 167-174.
21. Meillon S., Dammak H., Flavin E., and Pascard H., "Existence of a Direct Phase Transformation from Hematite to Maghemite, *Philosophical Magazine Letters* 72 (1995), pp. 105-110.
22. Finch and Sinha, "An Electron-Diffraction Study of the Transformation  $\alpha$ -Fe<sub>2</sub>O<sub>3</sub> to  $\gamma$ -Fe<sub>2</sub>O<sub>3</sub>, *Proceedings of Royal Society, London A.*, 241 (1957), pp. 1-8.
23. Boer and Dekkers, "Unusual Thermomagnetic Behaviour of Hematites; Neoformation of a Highly Magnetic Spinel Phase on Heating in Air", *Geophysical Journal of International* 144 (2001), pp. 481-494.
24. Randrianantoandro, Mercier A.M., Hervieu M., and Greneche J.M, "Direct Phase Transformation from Hematite to Maghemite During High Energy Ball Milling", *Materials Letters* 47 (2001) pp. 150-158.
25. Alcalá, J. M. Criado, and C. Real "Synthesis of Nanocrystalline Magnetite by Mechanical Alloying of Iron and Hematite", *Journal of Materials Science* 39 (2004), pp. 2365-2370.
26. Laberty and Navrotsky, "Energetics of Stable and Metastable Low-Temperature Iron Oxides and Oxyhydroxides", *Geochimica et Cosmochimica Acta* 62 (1998) 17, pp. 2905-2913.
27. Melamud, S.F. and Yur'ev B.P., "Study of the Hematite-Magnetite Reduction", *Metally*.1 (2001), pp 3-13.
28. Nasrazadani Seifollah, "Formation and Transformation Characteristics of Magnetite (Fe<sub>3</sub>O<sub>4</sub>) under Different Laboratory and Field Conditions", Ph.D. Dissertation, 1990, Louisiana State University.

29. Zhang J., Wu Z. Y., Ibrahim K., Abbas M. I., and Ju X., "Surface Structure of  $\alpha$ -Fe<sub>2</sub>O<sub>3</sub> Nanocrystal Observed by O K-edge X-ray absorption Spectroscopy", Nuclear Instruments and Methods in Physics Research, Section B; Beam Interactions with Materials and Atoms 199 (2003), pp 291-294.
30. Togawa. T., Sano T., Wada Y., Yamamoto T., Tsuji M., and Tamaura Y. "The Effect of the Crystal Orientation on the Rate of Formation of Cation-Excess Magnetite", Solid State Ionics 89 (1996) 279-286.
31. Hofmann, S J Campbell, W A Kaczmarek, and S Welzel, "Mechanochemical Transformation of Hematite to Magnetite: Structural investigation", Material Science Forum, 228-231(2), pp 607-614, 1996.
32. Music S., Krehula S., Popovic S., and Skoko Z., "Some Factors Influencing Forced Hydrolysis of FeCl<sub>3</sub> Solutions", Materials Letters 57 (2003) 1096-1102.
33. Schimanke and Martin, "In situ XRD study of the Phase Transition of Nanocrystalline Maghemite (Fe<sub>3</sub>O<sub>4</sub>) to Hematite ( $\alpha$ -Fe<sub>2</sub>O<sub>3</sub>)", Solid State Ionics 136-137 (2000), pp. 1235-1240.
34. P Ayyub, M S Multani, M Barma, V R Palkar and R Vijayaraghavan, "Size-induced Structural Phase Transitions and Hyperfine Properties of Microcrystalline Fe<sub>2</sub>O<sub>3</sub>", Journal of Physics C: Solid State Physics 21 (1988), pp. 2229-2245.
35. Sei, Cook, D. C., and Townsend, H. E, "Characterization of Iron Oxides Commonly Formed as Corrosion Products on Steel", Hyperfine Interaction 1998 (1997), pp. 59-65.
36. Friedel et al, "Characterization of Oxidized Steel Surfaces with Microscopic and Analytical Methods", Sonderbaende der Praktischen Metallographie 33 (2002), 59-67.
37. Nasrazadani and Raman, "Application of IR Spectra to Study the Rust Systems", Corrosion Science 34 (1993) 8, pp. 1335-1365.

38. Namduri, Nasrazadani, B. Fellers, Jim Stevens and Robert Theimer, "Application of FTIR in the Analysis of Iron Oxides and Oxyhydroxides Formed in PWR Secondary System", Steam Generator Secondary Side Management Conference (2003), February 10-12.
39. Namduri, Haritha, "Characterization of Iron Oxide Deposits formed at Comanche Peak Steam Electric Station", Masters Thesis, University of North Texas, May 2003.
- 40 A.G. Kumbhar, Narasimhan S.V., and Mathur P.K "Spectrophotometric Method for Determination Parts Per Million Levels of Cyclohexylamine in Water", Talanta 47 (1998) 421-437.
41. Rainer Kadnar, "Determination of Amines used in the Oil and Gas Industry (upstream section) by Ion Chromatography", Journal of Chromatography A, 850, 1999 (289-295).
42. Huanchi Xu , Swarna Addepalli and Jeff Kelber "EQCM studies of Amine Inhibition", Comanche Peak Steam Electric Station, 1996.
43. Addepalli and Kelber, "Effects of Amine Inhibitors on the Corrosion of Iron in Sulfate Media: Weightloss Measurements", Comanche Peak Steam Electric Station.
44. Addepalli and Kelber, "Role of Dissolved Oxygen in the Inhibitor Protection of Iron Films in Sulfate Solutions-Latest Results", Comanche Peak Steam Electric Station.
45. Do Haeng Hur, Hee Lee E., Sik Choi M., Sub Chung H., and Chul Kim U, "High Temperature Application of EDTA Solvents for Iron Oxide Removal", Journal of Nuclear Materials 299 (2001), pp. 271-273.
46. N. Ochaoa, Baril G., Moran F., and Pebere N., "Study of the Properties of a Multi-Component Inhibitor used for Water Treatment in Cooling Circuits", Journal of Applied Electrochemistry 32; 497-504, 2002.

47. C-O.A. Olsson, P. Agarwal, M. Frey, and D. Landolt “An XPS study of the Adsorption of Organic Inhibitors on Mild Steel Surfaces”, Corrosion science 42 (2000) 1197.
48. Ishikawa, H. Nishimori, A. Yasukawa, and K. Kandori “Formation of  $\gamma$ -FeOOH in the Presence of Amines”, Journal of Materials Science Letters 12 (1993) 1359-1361.
49. Ishikawa, T. Takeda, and K. Kandori “Effects of Amines in the Formation of  $\beta$ -Ferric Oxide Hydroxide”, Journal of Materials Science Letters 27 (1992) 4531-4535.
50. M. Bouayed, Rabaa H., Srhiri A., Saillard J.-Y., Ben Bachir A., and Le Beuze A., “Experimental and Theoretical Study of Organic Corrosion Inhibitors on Iron in Acidic Medium”, Corrosion Science 41 (1999) 501-517.
51. Tsuji, Nozawa K., and Aramaki K. “Ultrathin Protective Films Prepared by Modification of an N, N-Dimethylalkylamine Monolayer with Chlorosilanes for Preventing Corrosion of Iron”, Corrosion Science 42 (2000) 1523-1538.
52. Sastri, V.S., “Corrosion Inhibitors”, John Wiley & Sons. Inc., 1998.
53. Marcus, “Corrosion Mechanisms in Theory and Practice”, 2<sup>nd</sup> Edition, Marcel Dekker, Inc., New York, 2002.
54. Chacko and Nikles, “Iron Particle Surface Chemistry and Corrosion Protection by Amino-quinone Polyurethanes”, Applied Physics, 79 (1996) 8, 4863-4865.
55. Turner and Klimas, “The Effect of Alternative Amines on the Rate of Boiler Tube Fouling”, Final Report, TR-108004, EPRI Report, September 1997.
56. Lemire and McRae, “The Corrosion of Alloy 690 in High Temperature Aqueous Media – Thermodynamic Considerations”, Journal of Nuclear Materials 294 (2001), pp. 141-147.
57. Richard Brundle, Evans and Wilson “Encyclopedia of Materials Characterization”, Butterworth, Heinemann Co., 1992, ISBN-0-7506-9168-9.

58. Aaron D. Krawitz, “Introduction to Diffraction in Materials Science and Engineering”, John Wiley & Sons, Inc., 2001, ISBN – 0-471-24724-3.
59. Chevalier, M. Organista, B. Sala, A. Gelpi, and R. Erre, “Study of Deposits and Corrosion Products in the Secondary Side of Steam Generators by Fourier Transform Infrared Spectroscopy. Laboratory Study”, Ninth International Symposium on Environmental Degradation of Materials in Nuclear Power Systems-Water Reactors, TMS 1999, 577-586.
60. I. Whitehouse, J. Young, I. Botheroyd, P. Evans, S. Lawson and J. Wright, In-vessel Material Analysis of AGR Steam Generator Tubes using a Fiber Probe LIBS Instrument, LIBS 2000 Conference, Terrenia, Pisa, (Italy), 8-12 October 2000.

## CHAPTER 3

### CHARACTERIZATION OF CORROSION PRODUCTS FORMED AT COMANCHE PEAK STEAM ELECTRIC STATION (CPSES)

#### 3.1. Introduction

The present chapter summarizes the characterization results of the corrosion products formed on components of unit 1 and unit 2 pressurized water reactors at Comanche Peak Steam Electric Station (CPSES). Physical and chemical analyses were performed on the deposit samples collected from Unit 1 during the April 2004 (1RF10) and Unit 2 during October 2003 (2RF06) refueling outages. Data obtained from the analysis will be compared to data obtained from the similar analysis performed by the author on unit 1 and unit 2 for the outages that took place in 2002 (1RF09 for unit 1) and 2001 (2RF05 for unit 2)<sup>1, 2</sup>. The last section of this chapter quantifies the concentrations of all the major metallic and non-metallic species along with the trace elements for samples collected from unit 1 during 2004 outage and unit 2 during 2005 outage.

Formation and transport of the deposits formed in the secondary systems plays a major role in the corrosion of the steam generators. The corrosion caused by these deposits is a major contributor to the operation and maintenance cost of the steam generators<sup>3</sup>. So characterization of these deposits will be helpful in giving an insight into the different corrosion processes taking place in the secondary side<sup>4, 5</sup>.

Physical and chemical analyses have been performed on different samples collected from unit 1 and unit 2 at CPSES. Scanning electron microscopy (SEM) was used for physical analysis of the samples to study the morphology and thickness of the oxide. Energy dispersive



spectroscopy (EDS) was used to identify different elements present in the deposits which contribute to corrosion and Fourier transform infrared spectrophotometry (FTIR) to determine the iron oxide phases present in the deposit samples.

Impurities and/or the corrosion products are transported due to gradual erosion and corrosion of pressurized water reactor (PWR) feedwater, condensate and drain systems and adhere onto the pressurized boundary surfaces as corrosion layers<sup>6</sup>. These layers may consist of a mixture of iron oxides and hydroxides in ferrous systems or copper and zinc oxides or hydroxides in copper alloy components<sup>7, 8, 9</sup>. These corrosion product layers on system lead to denting, inter-granular attack and stress corrosion cracking (IGA/SCC) and pitting at tube supports and sheet crevices, which in turn lead to high maintenance cost of the secondary systems<sup>10, 11, 12</sup>. So knowledge of the nature of these deposits, which can be obtained from deposit characterization, can help in predicting the effect of these deposits on the steam generator operation. Deposit characterization basically deals with sampling, packaging and laboratory analyses of the deposit samples. Different physical and chemical analyses are performed on these deposit samples to obtain compositional and structural information, oxidation state of the deposit materials etc.

#### 3.1.1. Need for deposit characterization

There are many benefits of deposit characterization. Determining the physical and chemical properties of the deposits formed can help in efficiently planning for mechanical and chemical maintenance. Chemical analysis of deposits can reveal the presence of metals like lead, copper, arsenic which play a vital role in corrosion of secondary system units. Measurement of deposit thickness, composition and morphology can contribute to more accurate calculations of thermal performance of the units. Knowledge of the oxidation state of deposits can help in

assessing the effectiveness of oxygen scavengers. The presence of magnetite ( $\text{Fe}_3\text{O}_4$ ) and hematite ( $\alpha\text{-Fe}_2\text{O}_3$ ) or even the presence of iron oxyhydroxides such as  $\alpha\text{-FeOOH}$  and  $\gamma\text{-FeOOH}$  can promote formation of copper oxides. Characterization of deposit samples in one unit when compared to the other unit can give vital information about the performance of these units.

### 3.2. Experimental Procedure

Figures 3.1 and 3.2 are the schematics of the secondary systems for units 1 and 2 respectively. Samples received were properly identified and marked carefully. Photographs of the samples were taken and recorded carefully. Samples were identified as: a) solid samples (bolts, washers and nuts) and b) powder samples (sludge).

After the samples were identified, the strategy for characterizing of these deposit samples was planned by referring to previous characterization work done in the plant and by referring to the past work done by researchers in this field. Two forms of analysis have been used to characterize the deposit samples. They are a) physical analysis – oxide thickness and morphology and b) chemical analysis – identification of different elements.

### 3.3. Results and Discussion

#### 3.3.1. Thickness Measurements of Deposits on Samples Collected From Unit 1 and Unit 2 Components

Table 3.1 shows measured thickness of scale formed on different components of unit 1. The overall average thickness for all components in unit 1 was  $18.90\text{ }\mu\text{m}$ . Table 3.2 shows the

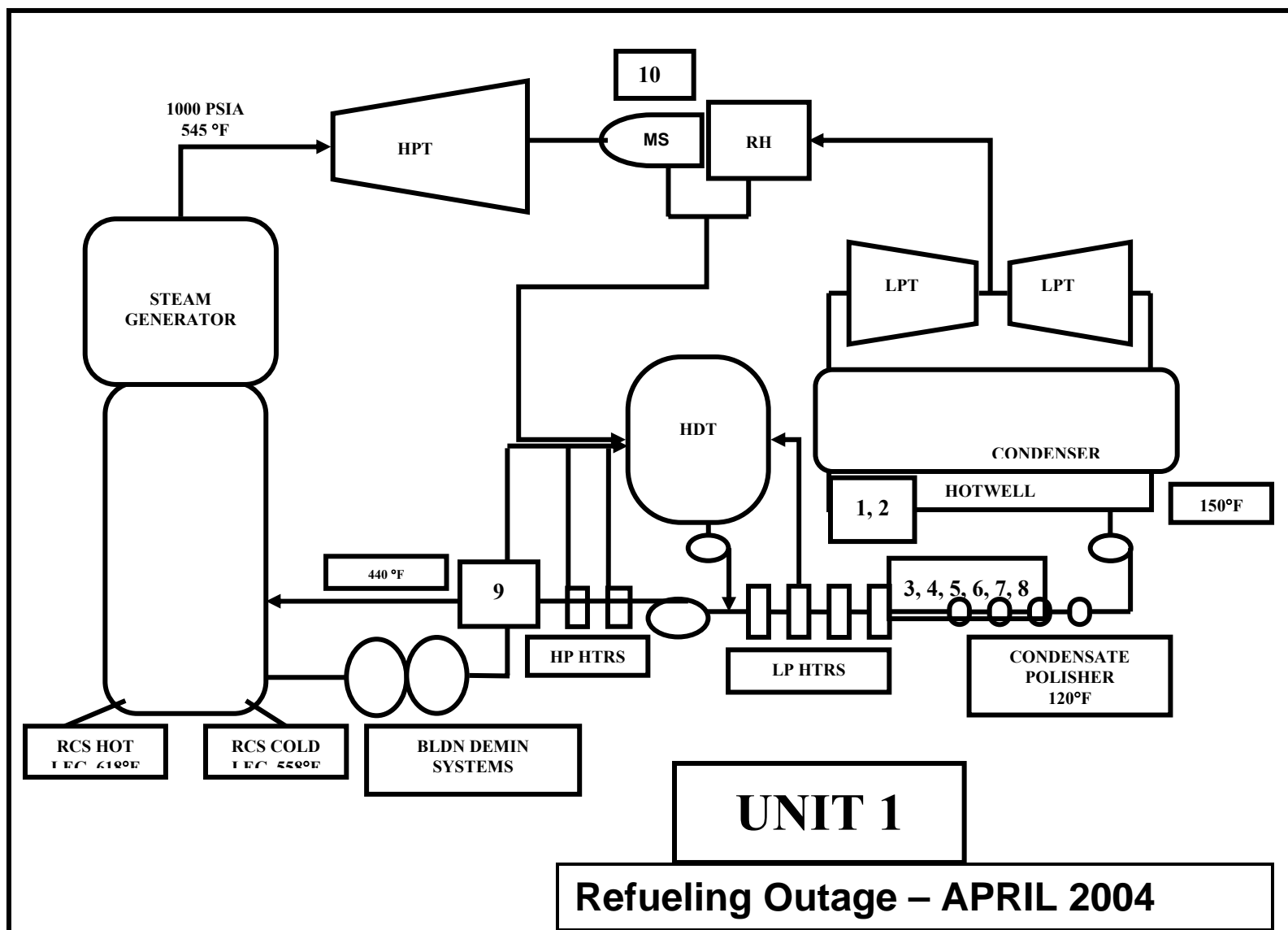


**Figure 3.1. Schematic of sample identification for samples from unit 1**  
 (Reactor coolant system (RCS), blow down de-mineralizing system (BLDN DEMIN SYS), high pressure heaters (HP HTRS), low pressure heaters (LP HTRS), low pressure turbine (LPT), re-heater (RH), moisture separator (MS), high pressure turbine and (HPT), Heater Drain Tank (HDT))

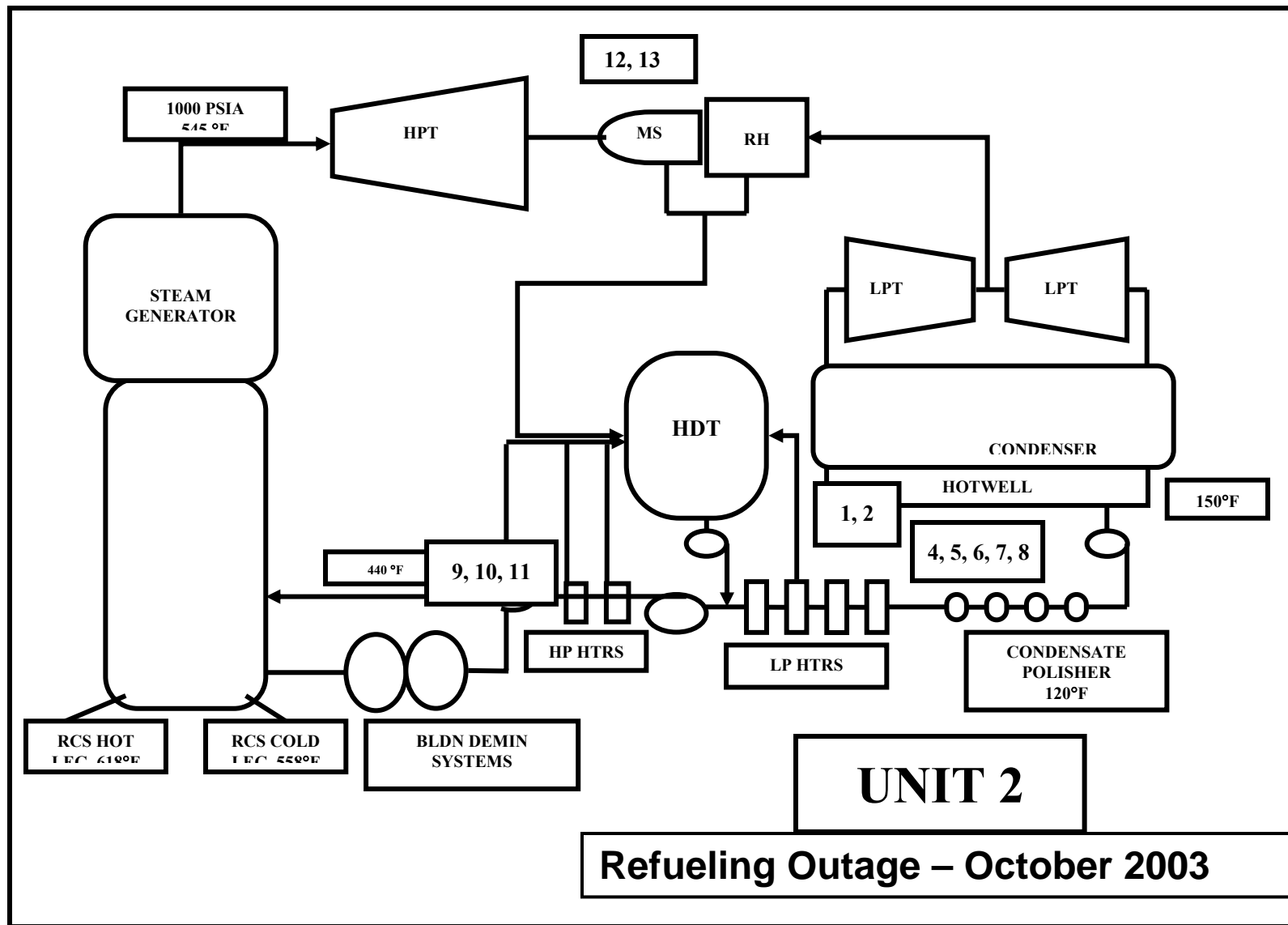


**Figure 3.2. Schematic of sample identification for samples from unit 2**  
 (Reactor coolant system (RCS), blow down de-mineralizing system (BLDN DEMIN SYS), high pressure heaters (HP HTRS), low pressure heaters (LP HTRS), low pressure turbine (LPT), re-heater (RH), moisture separator (MS), high pressure turbine and (HPT), heater drain tank (HDT))

measured thickness of scale formed on different components of unit 2. The overall average thickness for all components in unit 2 was 17.80  $\mu\text{m}$ .

**Table 3.1. Deposit thickness measurement of samples collected from unit 1**

SAMPLE IDENTIFICATION	DESCRIPTION	OXIDE THICKNESS (AVG., $\mu\text{m}$ )
1RF3	Feedwater Heat Exchange	19.8
1RF4	1-6B Feedwater Heat Exchange	19.4
1RF5	1-5 A Feedwater Heat Exchange	39.9
1RF6	1-5B Feedwater Heat Exchange	32.2
1RF7	1-4B Feedwater Heat Exchange	4.0
1RF8	1-3A Feedwater Heat Exchange	19.8
1RF9	1-1B Feedwater Heat Exchange	8.9
1RF10	MSR 1-A Tube side	6.8
<b>AVERAGE THICKNESS</b>		<b>18.9 <math>\mu\text{m}</math></b>

**Table 3.2. Deposit thickness measurement of samples collected from unit 2**

SAMPLE IDENTIFICATION	DESCRIPTION	OXIDE THICKNESS (AVG., $\mu\text{m}$ )
2RF4	Feedwater Heater, 2-6-A, washer	2.1
2RF5	Feedwater Heater, 2-6-B, washer	23.4
2RF6	Feedwater Heater 2-5-A, washer	36.5
2RF7	Feedwater Heater 2-5-B, washer	9.9
2RF8	Feedwater Heater 2-4-B, washers	8.3
2RF9	Feedwater Heater, 2-2B, washers	48.0
2RF12	Moisture Separator Reheater 2-A, tube side	8.3
2RF13	Moisture Separator Reheater 2-B, tubeside, washer	6.1
<b>AVERAGE THICKNESS</b>		<b>17.8 <math>\mu\text{m}</math></b>

### 3.3.2. Deposit Analysis of Different Components For Unit 1 and Unit 2

a) Main condensers: Samples from unit 1 show flaky porous rust with particle sizes ranging from 5-10  $\mu\text{m}$  (Figures 3.3 a and b). EDS spectrum shown in Figure 3.4 indicates mainly the presence of Fe, and O. FTIR analysis shows a clear presence of  $\text{Fe}_3\text{O}_4$ ,  $\alpha\text{-FeOOH}$  and traces of  $\gamma\text{-FeOOH}$  as shown in Figure 3.11.

Samples from unit 2 show flaky porous rust with particles sizes ranging from 2-5  $\mu\text{m}$  (Figures 3.3 c and d). EDS spectrum in Figure 3.4 shows the presence of Fe, O, and Cu as the elements present in these samples. FTIR analysis shows a clear presence of  $\alpha\text{-Fe}_2\text{O}_3$ ,  $\text{Fe}_3\text{O}_4$ ,  $\alpha\text{-FeOOH}$  and  $\gamma\text{-FeOOH}$  as shown in Figure 3.12.

(b) High and low pressure feedwater heaters: The samples collected from low pressure feedwater heaters of both unit 1 and unit 2 showed crystalline grains forming a porous oxide layer (Figure 3.5 (a-d)). The average (6 samples) oxide layer thickness of the samples collected from unit 1 was found to be 22.5  $\mu\text{m}$ . EDS analysis on the samples collected from unit 1 and unit 2 showed the presence of Fe, O, Si, Ni, and Cr. The elemental mapping of the sample collected (Figure 3.6) from unit 1 clearly shows regions with concentrations of Ni. Areas with Ni and Si concentrations were found in unit 2 sample (Figure 3.7). The samples collected from low pressure feedwater heaters of unit 2 showed needle like particles (probably  $\text{FeOOH}$ ) in between the crystalline grains forming a porous oxide layer (Figure 3.5c). The average (5 samples) oxide layer thickness of the samples collected was found to be 16  $\mu\text{m}$ . Ni and Si may be present in the system due to the construction material used in the secondary system, as Inconel is an alloy of Ni, Fe and Cr. Phase analysis using FTIR for unit 1 showed the presence of  $\text{Fe}_3\text{O}_4$ ,  $\gamma\text{-Fe}_2\text{O}_3$ ,  $\alpha\text{-FeOOH}$  and traces of  $\gamma\text{-FeOOH}$  (Figure 3.11) and unit 2 showed  $\alpha\text{-Fe}_2\text{O}_3$ ,  $\alpha\text{-FeOOH}$  and traces of  $\gamma\text{-FeOOH}$  (Figure 3.12).

The samples collected from high-pressure feedwater heaters of unit 1 showed porous layer of oxide with crystalline grains (Figure 3.5b). The oxide thickness was found to be 8.9  $\mu\text{m}$ . Elemental analysis of these samples showed the presence of Fe, O, and Cr. FTIR analysis of the sample collected from the high pressure water heaters did not show any oxide absorption peak. The samples collected from high-pressure feedwater heaters of unit 2 showed porous layer of oxide with crystalline grains (Figure 3.5d). The oxide thickness was found to be 48  $\mu\text{m}$ . Elemental analysis of these samples showed the presence of Fe, O, Na, Ni, Al, Cr, and Cu.

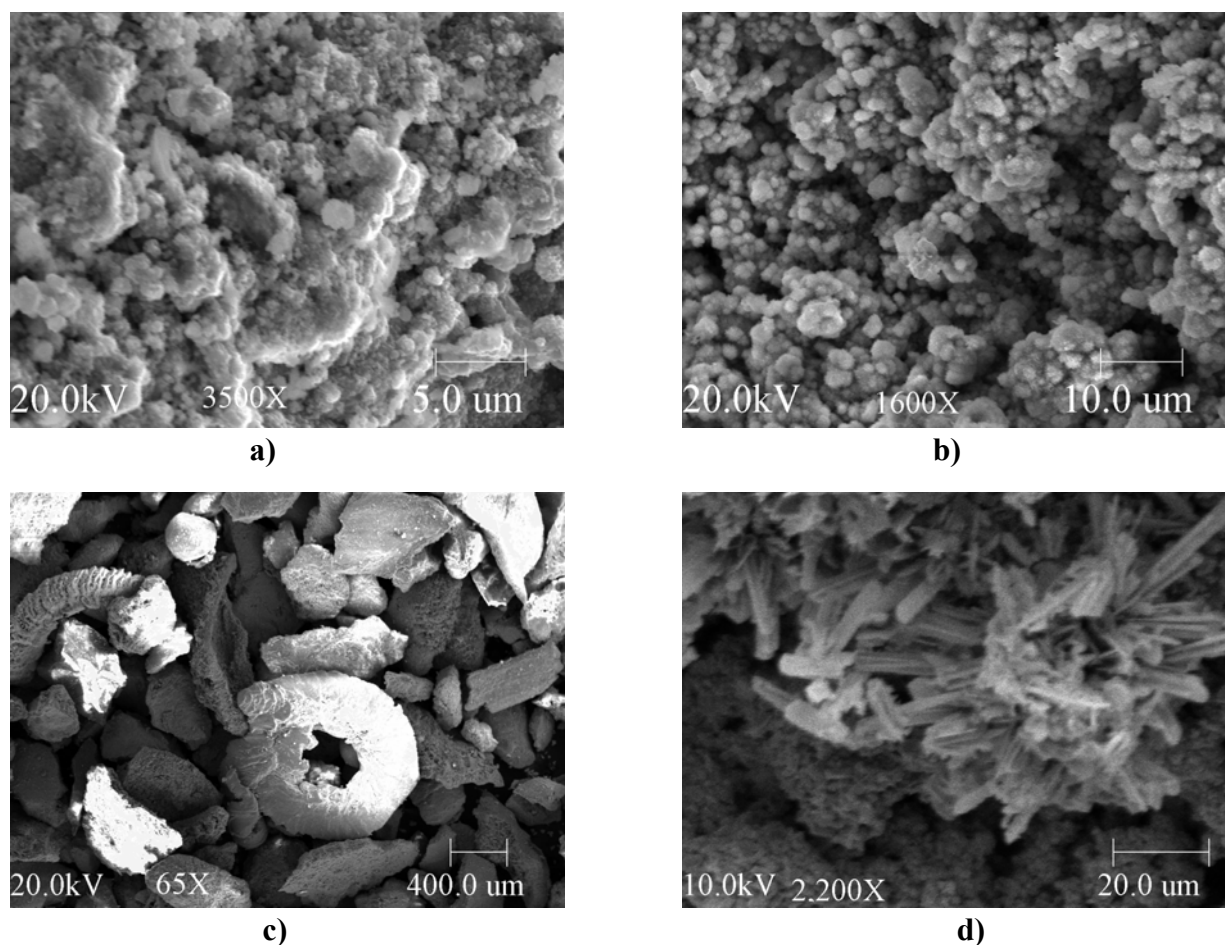


**Figure 3.3. SEM photographs of main condenser sample from a) & b) unit 1 and c) & d) unit 2**

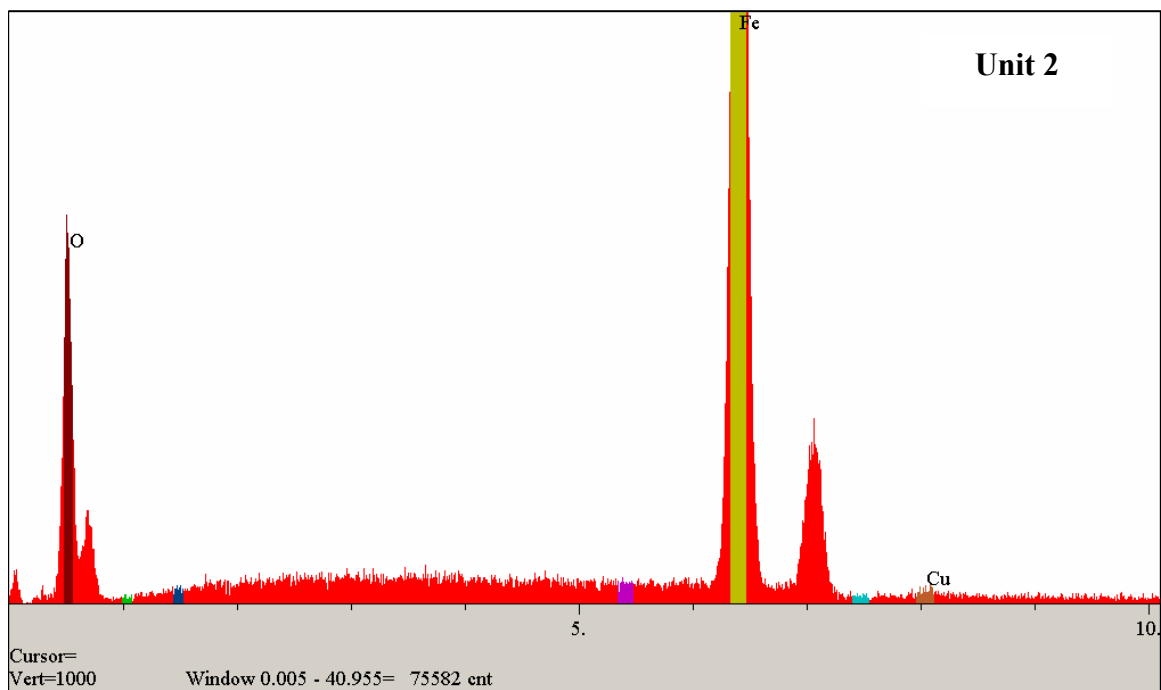
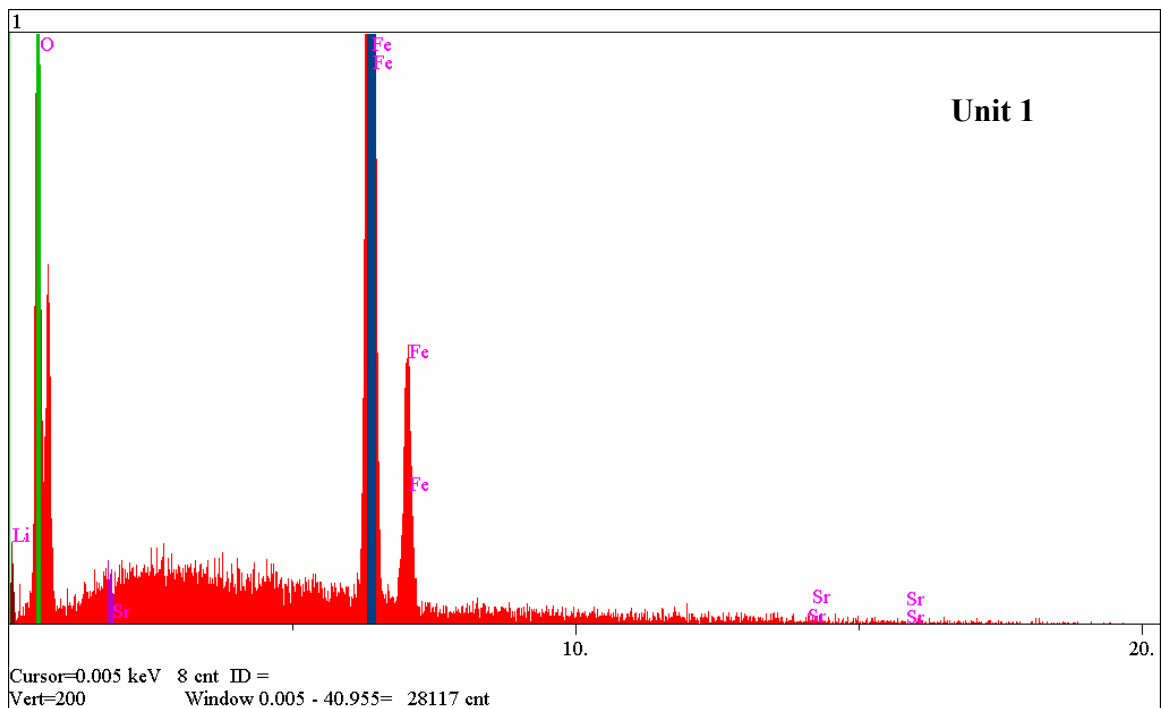
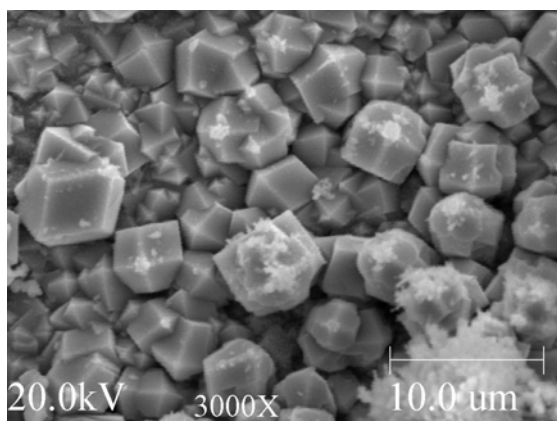
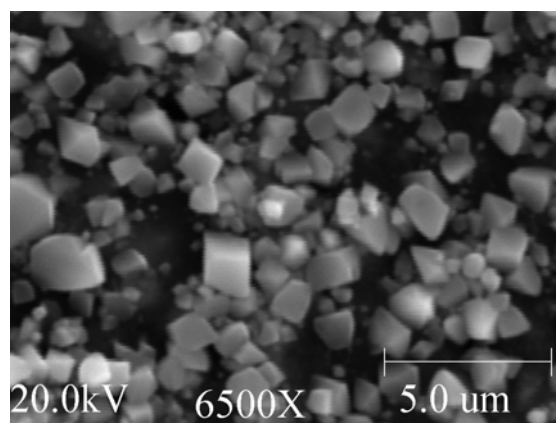


**Figure 3.4. EDS spectra of main condenser sample from a) unit 1 and b) unit 2**

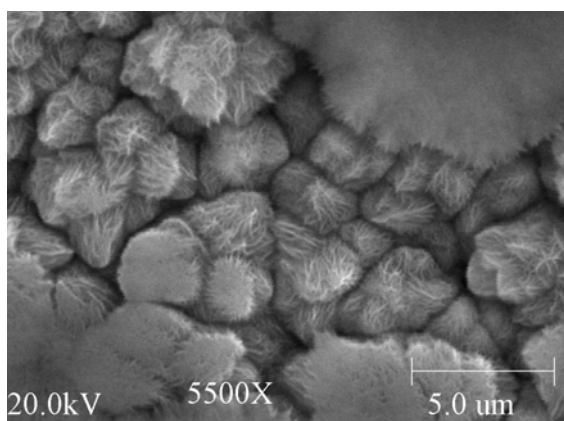




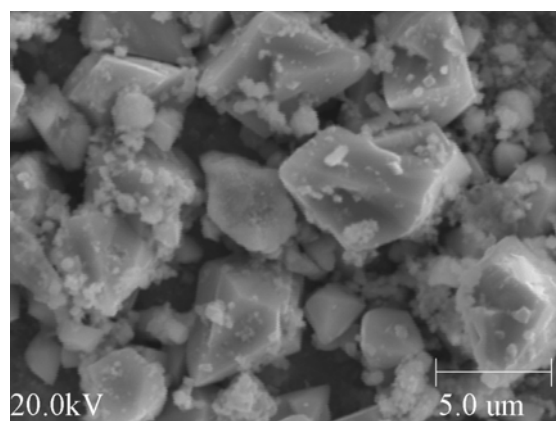
a)



b)



c)



d)

**Figure 3.5. SEM photographs of feedwater heater samples collected from a) & b) unit 1 and c) & d) unit 2**

c) Deposit analysis of moisture separators: SEM analysis of the morphology of the samples collected from moisture separator showed porous oxide layer consisting of crystalline grains (Figure 3.8a). The average oxide layer thickness of the sample collected from unit 1 was found to be 6.8  $\mu\text{m}$ . EDS analysis showed presence of elements like Fe, O, Cr, Ni, and P (Figure 3.9). FTIR analysis of the samples mainly showed presence of  $\gamma\text{-Fe}_2\text{O}_3$  and  $\alpha\text{-FeOOH}$  (Figure 3.11).

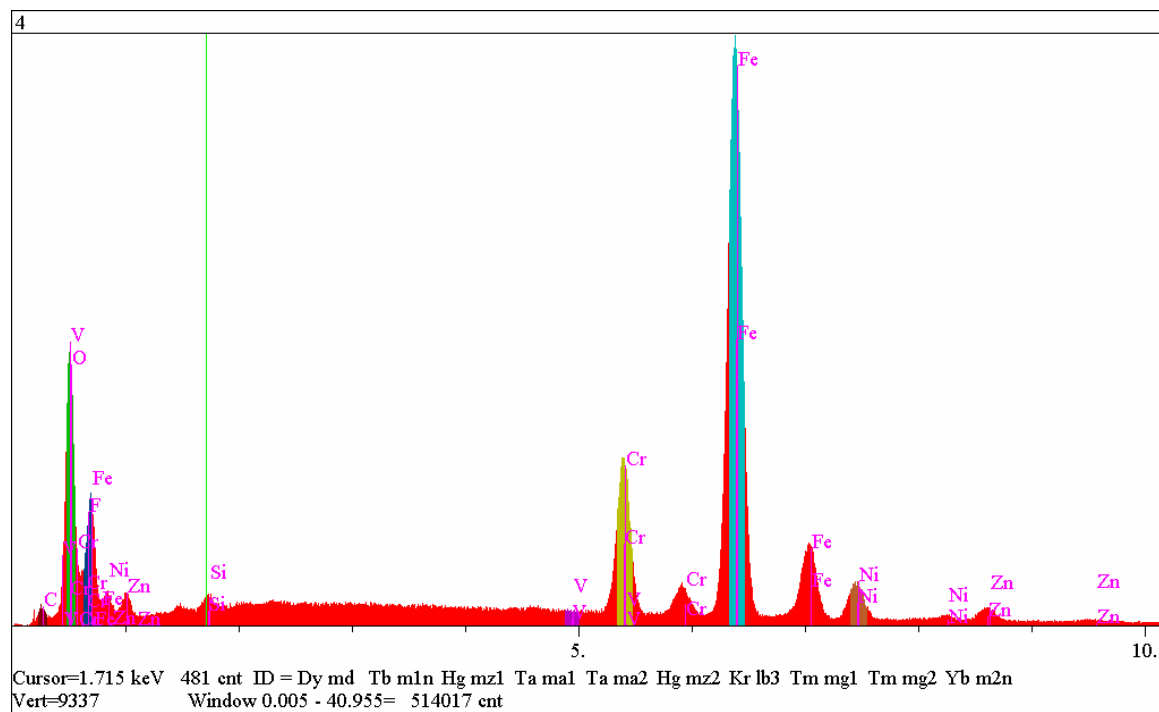
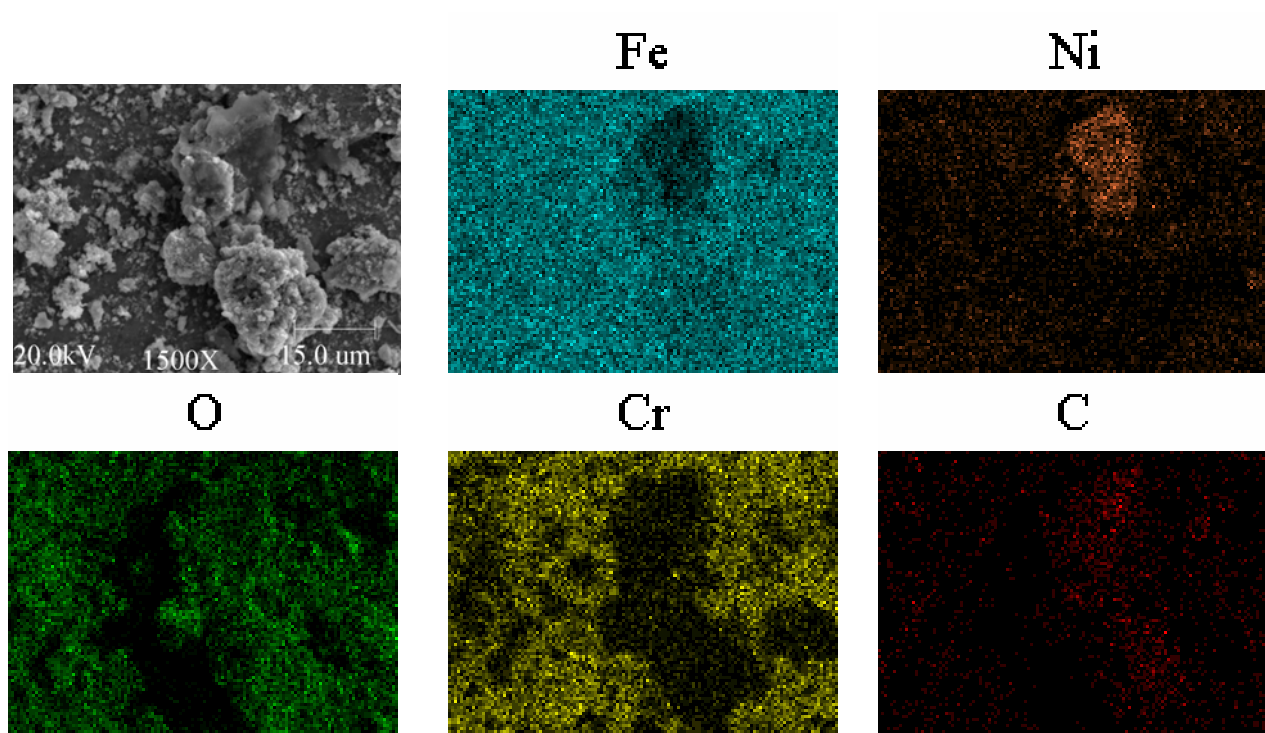


**Figure 3.6. EDS analysis of feedwater heater sample collected from unit 1**

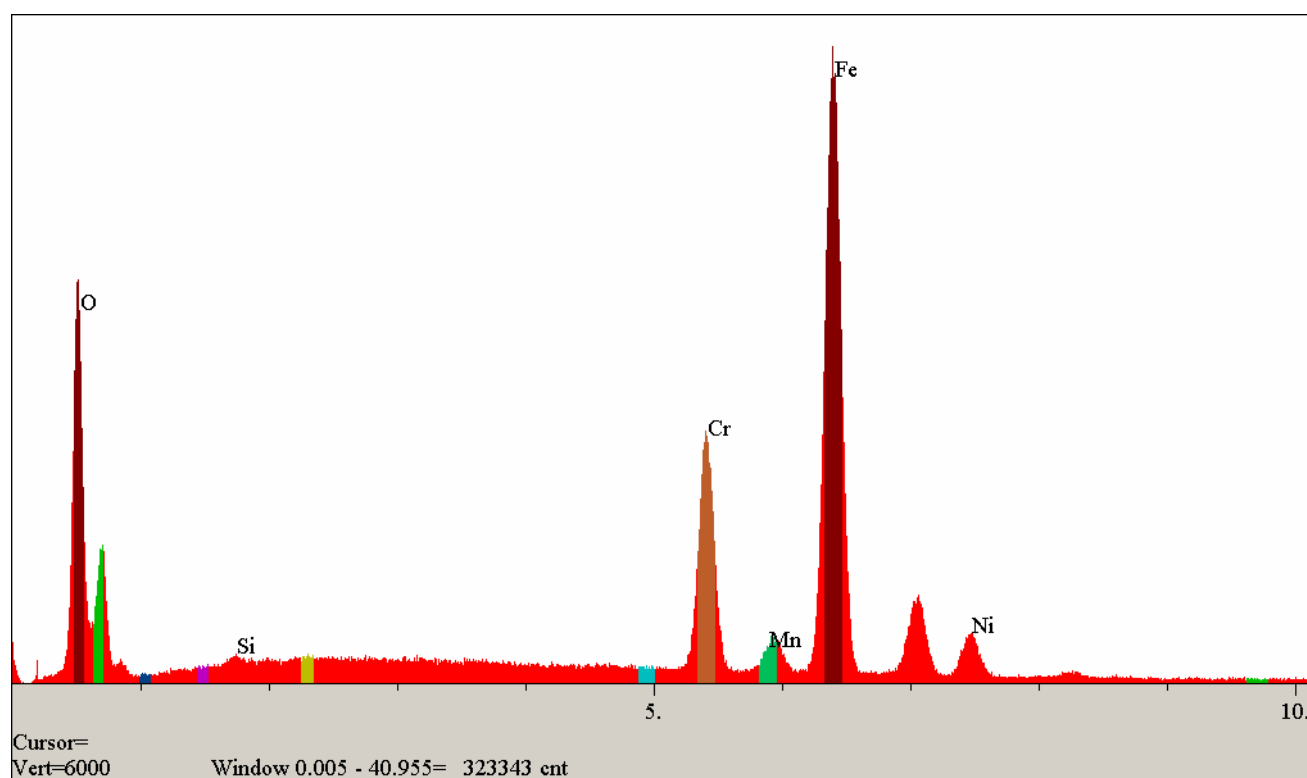
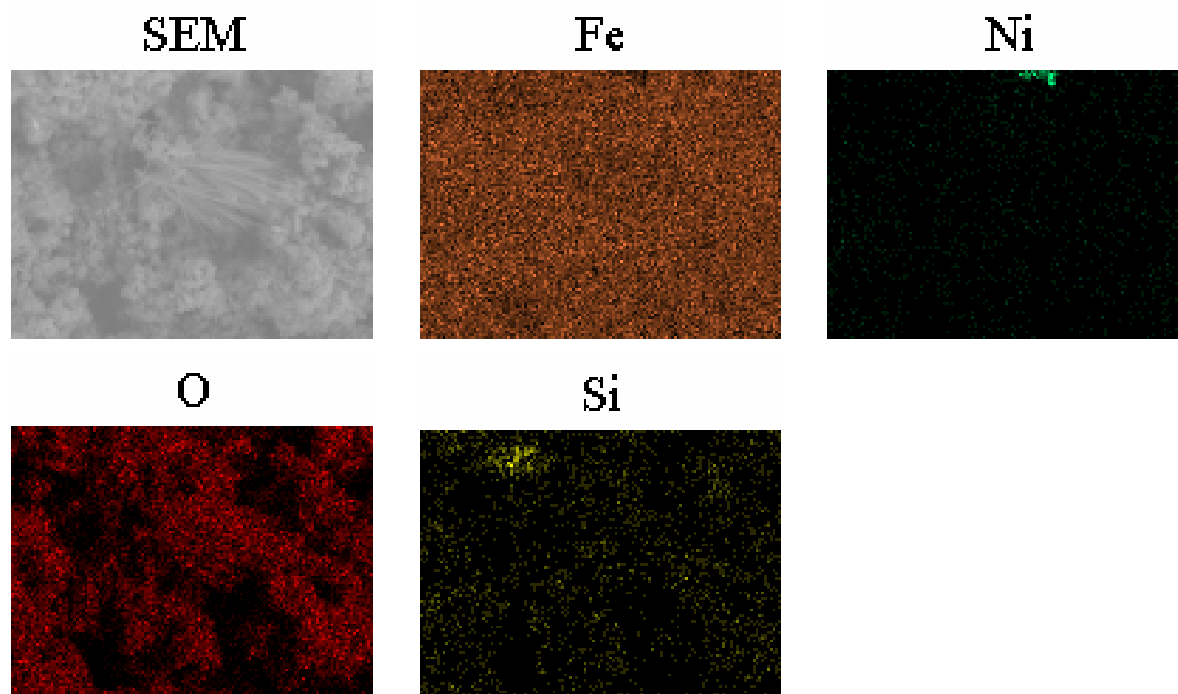


**Figure 3.7. EDS analysis of feedwater heater sample collected from unit 2**

SEM analysis of the morphology of the samples collected from moisture separator showed long platelets on a porous oxide layer consisting of crystalline grains (Figure 3.8b). The average oxide layer thickness of the samples (2 samples) collected was found to be 7.2  $\mu\text{m}$ .

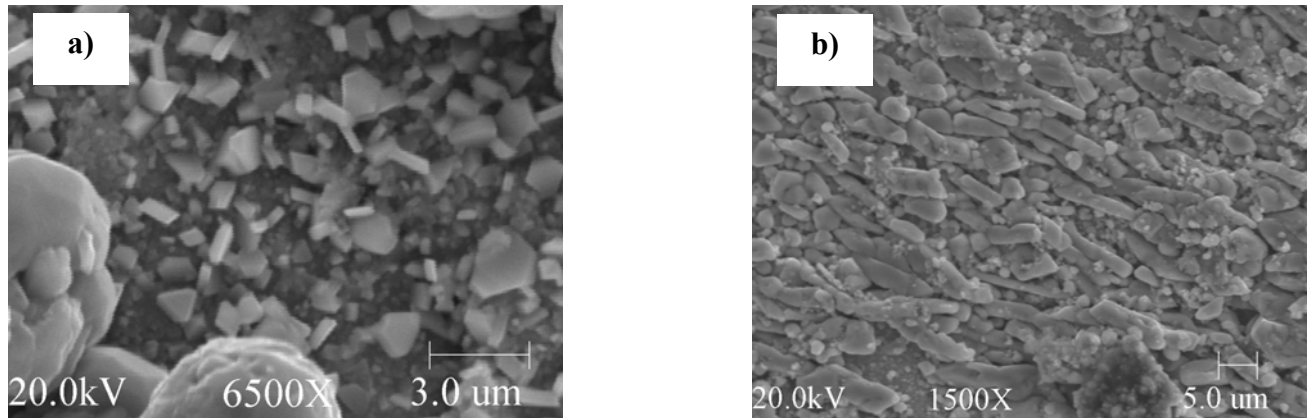


**Figure 3.8.: Moisture separator samples for a) unit 1 and b) unit 2**

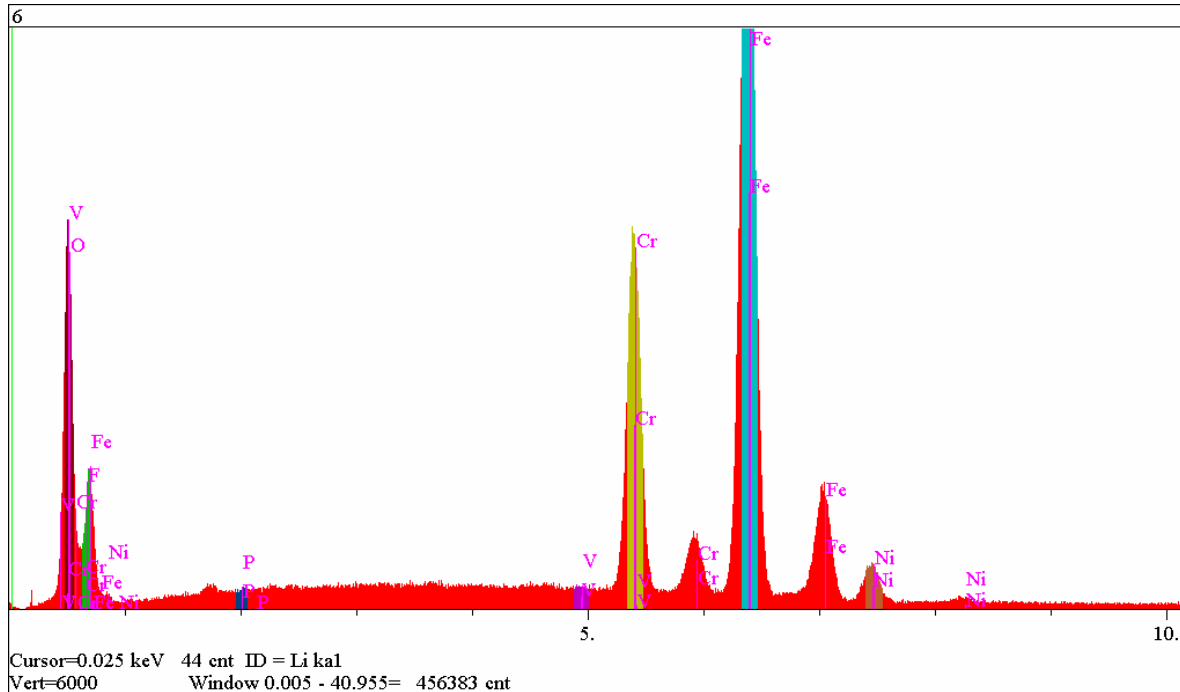


**Figure 3.9.: EDS spectra for moisture separator sample collected from unit 1**

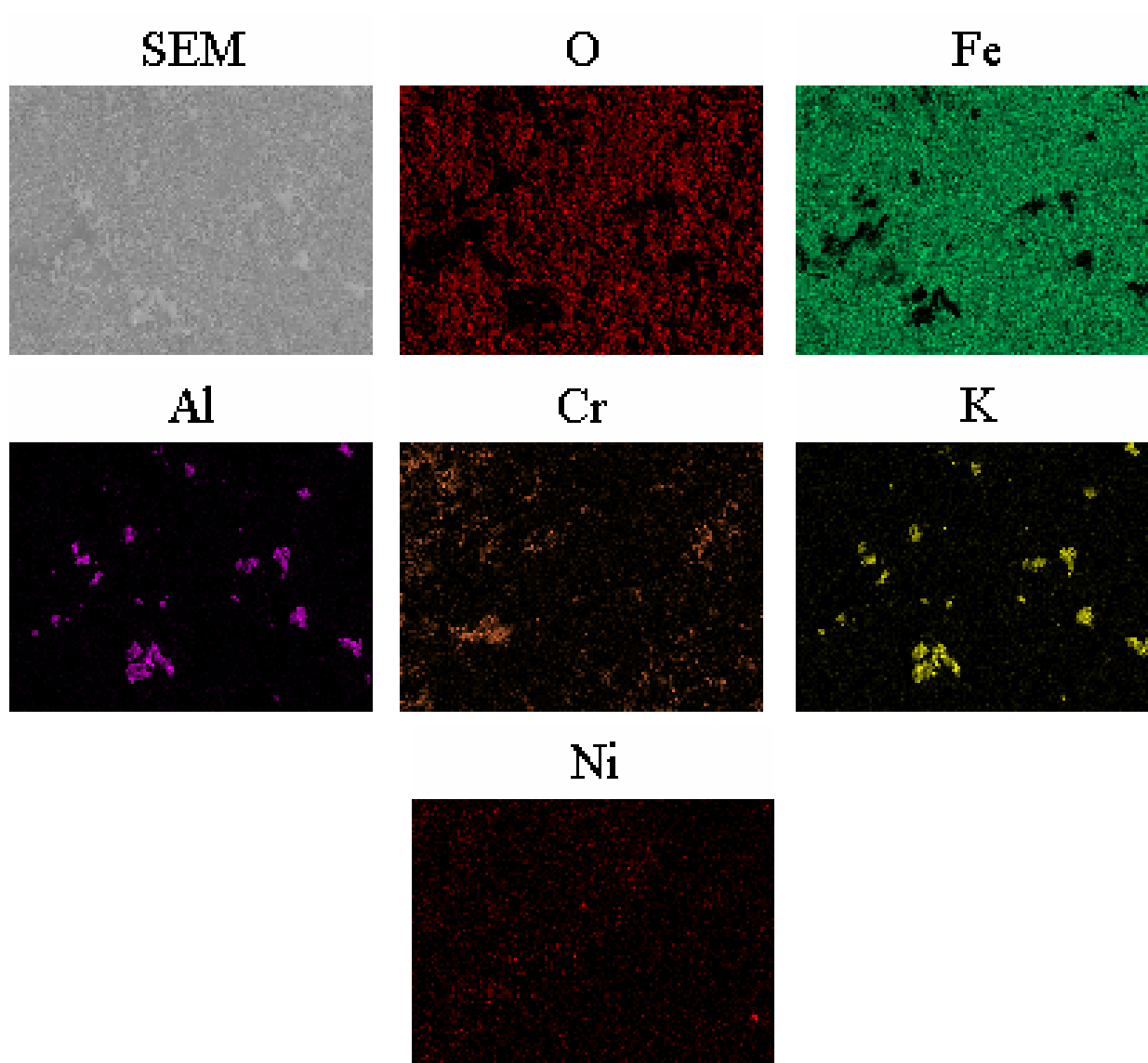
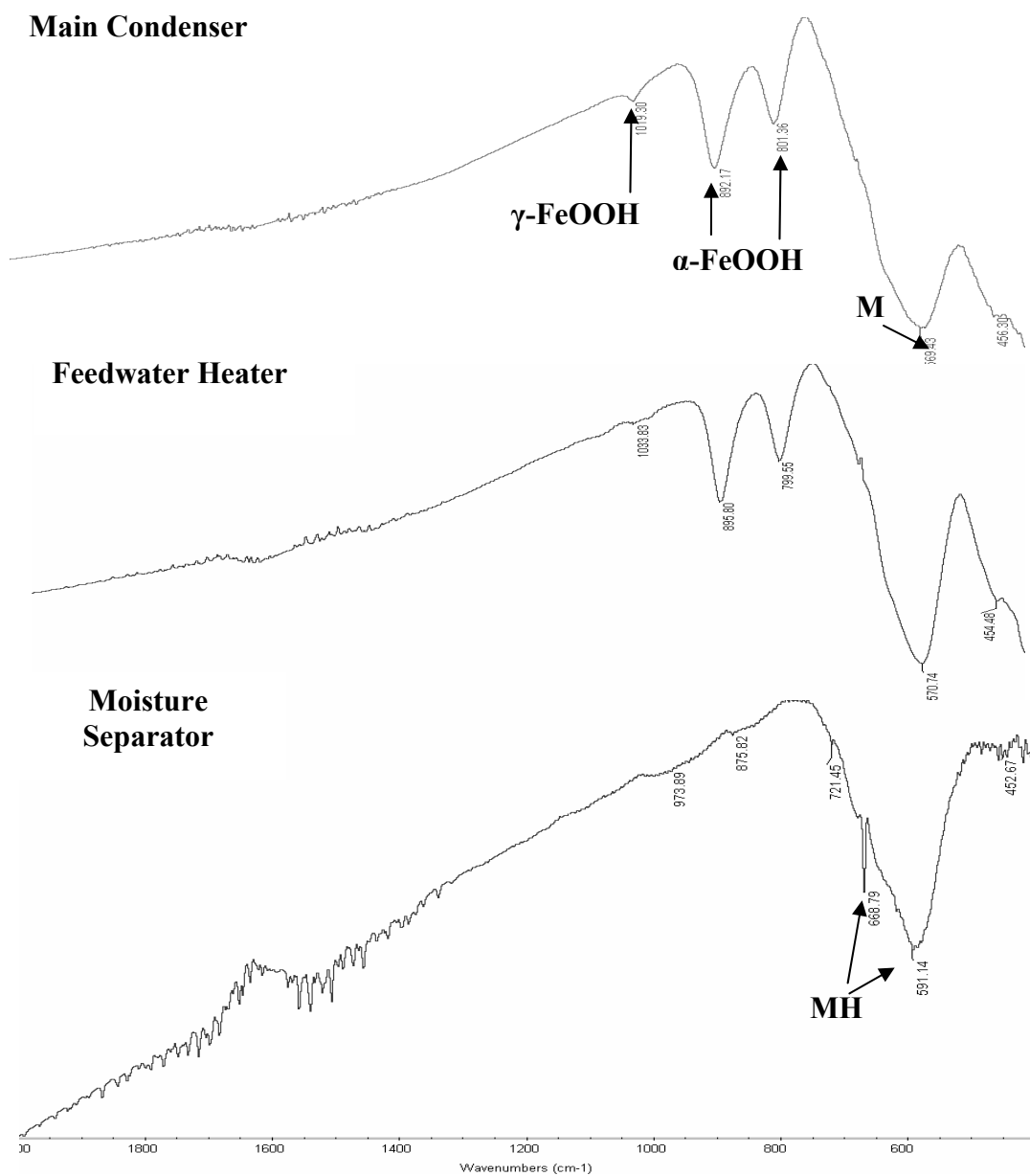


**Figure 3.10. Elemental mapping of moisture separator sample collected from unit 2**

FTIR analysis of the samples mainly showed presence of  $\text{Fe}_3\text{O}_4$  and  $\gamma\text{-FeOOH}$  (Figure 3.12). Elemental mapping of this sample from unit 2 showed the presence of elements like Fe, O, Al, Cu, Ni, and K (Figure 3.10). The elemental mapping showed small areas of concentration of K, Cr and Al.



## Unit 1

**Figure 3.11. FTIR spectra of samples collected from unit 1 (M- magnetite, and MH-maghemite)**

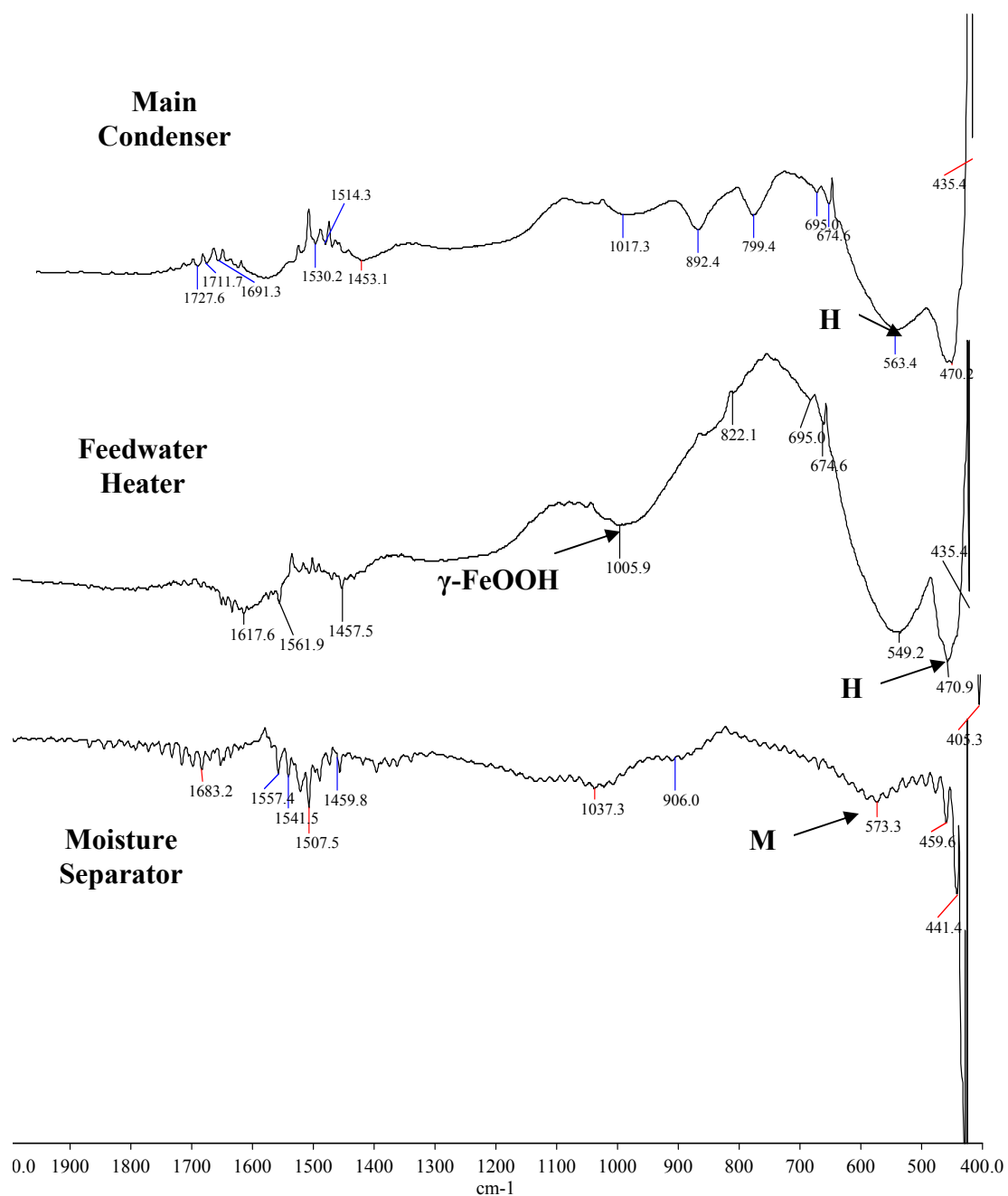


**Figure 3.12. FTIR spectra of samples collected from unit 2 (H- hematite, and M- magnetite)**

### 3.4. Summary and Conclusions

#### 3.4.1. Comparison of Samples for Unit 1 For Years 2002 and 2004 Outages

Table 3.3 shows a comparison between the samples collected during refueling outage 2002 and 2004 from unit 1. The average thickness of the oxide layer of the samples collected during 2002 outage was 92  $\mu\text{m}$  whereas that collected from 2004 outage is 18.9  $\mu\text{m}$ . The samples from 2002 outage showed presence of dominant phases of magnetite along with maghemite. The samples collected from 2004 outage showed mainly  $\alpha\text{-Fe}_2\text{O}_3$ ,  $\alpha\text{-FeOOH}$  and some traces of  $\text{Fe}_3\text{O}_4$  and  $\gamma\text{-FeOOH}$  phases. Elements like Cr, Fe, O and Ni were found to be common in both the cases. F was observed to be present in the samples collected from 2004 outage which was unlike the 2002 outage. Cu was present in most of the samples collected from 2002 outage but samples from 2004 contain very negligible amounts of Cu. The 2004 outage samples were rich in their Cr content (especially the feedwater samples) when compared to 2002 outage samples.

Table 3.4 shows a comparison between the samples collected during refueling outage 2002 and 2003 from unit 2. The average thickness of the oxide layer of the samples collected during 2002 outage was 15  $\mu\text{m}$  whereas that collected from 2003 outage is 17.8  $\mu\text{m}$ . The samples from 2002 outage showed presence of dominant phases of maghemite along with magnetite. The samples collected from 2003 outage showed mainly  $\alpha\text{-Fe}_2\text{O}_3$ ,  $\text{Fe}_3\text{O}_4$  and  $\gamma\text{-FeOOH}$  phases. Elements like Cr, Cu, Mn, Si, Fe, Al and Ni were found to be common in both the cases. Tables 3.5 and 3.6 show the summary of analysis for unit 1 and unit 2 respectively.



**Table 3.3. Comparison of samples for unit 1 for years 2002 and 2004 outages**

<b>Component</b>	<b>Year 2002</b>	<b>Year 2004</b>
<b>Condenser</b>	Fe <sub>3</sub> O <sub>4</sub> +γ-Fe <sub>2</sub> O <sub>3</sub> + traces of α- FeOOH + γ -FeOOH S, Fe, Cu, Mn, Zn, Ca and Si Particle 200-250 μm	Fe <sub>3</sub> O <sub>4</sub> , α-FeOOH, and traces of γ-FeOOH Fe, O, Na, Ni, Al, Cr, and Cu 5-10 μm particle size
<b>LP Heaters</b>	α - Fe <sub>2</sub> O <sub>3</sub> + γ -Fe <sub>2</sub> O <sub>3</sub> + α - FeOOH and traces of Fe <sub>3</sub> O <sub>4</sub> Si, Ca, Cr, Fe, Zn 60 μm	α-Fe <sub>2</sub> O <sub>3</sub> , Fe <sub>3</sub> O <sub>4</sub> , and α - FeOOH Fe, O, Si, S, Mn, V, Na, and Ni 22.5 μm
<b>HP Heaters</b>	γ - Fe <sub>2</sub> O <sub>3</sub> + α- Fe <sub>2</sub> O <sub>3</sub> Fe, Cu 165 μm	Inconclusive Fe, O, Na, Ni, Al, Cr, and Cu 8.9 μm
<b>Moisture Separators</b>	Fe <sub>3</sub> O <sub>4</sub> Fe, Si, Ni, Cu and high Cr 40 μm	Fe <sub>3</sub> O <sub>4</sub> Fe, O, Al, Cu, Ni, Mn, Mg, F, and Na 6.8 μm

**Table 3.4. Comparison of samples for unit 2 for years 2002 and 2003 outages**

<b>Component</b>	<b>Year 2002</b>	<b>Year 2003</b>
<b>Condenser</b>	Fe <sub>3</sub> O <sub>4</sub> +γ-Fe <sub>2</sub> O <sub>3</sub> Fe 14-16 μm	Fe <sub>3</sub> O <sub>4</sub> , α-Fe <sub>2</sub> O <sub>3</sub> , α-FeOOH, and γ-FeOOH Fe, O, Na, Ni, Al, Cr, and Cu 2-5 μm particle size
<b>LP Heaters</b>	α - Fe <sub>2</sub> O <sub>3</sub> + γ -Fe <sub>2</sub> O <sub>3</sub> + α - FeOOH Fe, Ni, Cr, and Si 15 μm	Fe <sub>3</sub> O <sub>4</sub> , α-Fe <sub>2</sub> O <sub>3</sub> , and γ-FeOOH Fe, O, Si, S, Mn, V, Na, and Ni 16 μm
<b>HP Heaters</b>	Fe <sub>3</sub> O <sub>4</sub> , Fe, Si, K, Cr, and Ni 17.5 μm	α-Fe <sub>2</sub> O <sub>3</sub> , γ-FeOOH and α-FeOOH Fe, O, Na, Ni, Al, Cr, and Cu 48 μm
<b>Moisture Separators</b>	α - Fe <sub>2</sub> O <sub>3</sub> + Fe <sub>3</sub> O <sub>4</sub> Fe, Ni, Cr, Si, Al, Zn, Cu, Mn, and S 5 μm	Fe <sub>3</sub> O <sub>4</sub> and some unidentified phases Fe, O, Al, Cu, Ni, Mn, Mg, F, and Na 7.2 μm

Fe, Ni, Cr and Cu were the commonly found elements in the deposit samples. The presence of Ni, Fe and Cr is expected in the deposit samples collected from the SG system as the constructional material used for tubing is alloy 600. Alloy 600 is an alloy of Ni, Cr and Fe. The major element in this alloy is Nickel. Therefore the presence of these elements in the deposit samples is justified. Copper is known for its excellent heat transfer properties and is commonly used in PWR steam cycles. The major source of Cu is from the feedwater, condensate and drain systems. However, when these systems are operated at pH is greater than about 9.3, the corrosion of the copper bearing material increases<sup>5</sup>. Very small quantity of Cu is added to alloy 600. Also, the presence of Cu in the deposit samples can be attributed to the fact that the blowdown efficiency for copper is low. Minor species like Zn, Mn, Mg, Si, S etc have been found to be present in the deposit samples.

FTIR technique has proven to be an efficient tool in identifying different iron oxides and hydroxides present in the deposit samples. XRD technique has been traditionally used in the identification of iron oxide phases by the power industry. XRD analysis is based on the crystal structure of the sample. Since magnetite and maghemite have similar crystal structure, it is very difficult to resolve between these two iron oxides. So FTIR technique has been used successfully in identifying these phases. The absorbance peak of magnetite is  $570\text{ cm}^{-1}$  whereas that of maghemite is  $600\text{ cm}^{-1}$ . Therefore one can easily differentiate between these two iron oxides

**Table 3.5. Summary of characterization results for the samples collected from unit 1 (2004 Outage)**

Sample Identification	Description	SEM	FTIR	EDS
1RF1	Main Condenser 1-A hotwell, sediment	Porous, round particles	$\alpha$ -Fe <sub>2</sub> O <sub>3</sub> , $\alpha$ -FeOOH	Fe, and O
1RF2	Main Condenser hotwell, 1-B, deposit	Porous and round particles	$\alpha$ -Fe <sub>2</sub> O <sub>3</sub> , $\alpha$ -FeOOH and traces of $\gamma$ -FeOOH	Fe, and O
1RF3	Feedwater Heater 1-6A, washers	Porous upper layer with needle like particles at the bottom layer Oxide thickness 19.8 $\mu$ m	$\alpha$ -Fe <sub>2</sub> O <sub>3</sub> , $\alpha$ -FeOOH and traces of $\gamma$ -FeOOH	Fe, O, F, and P
1RF4	Feedwater Heater , 1-6-B , washers	Porous oxide layer with crystalline particles Oxide thickness: 19.4 $\mu$ m	$\alpha$ -Fe <sub>2</sub> O <sub>3</sub> , $\alpha$ -FeOOH	Fe, O, F and S
1RF5	Feedwater Heater, 1-5-A, washer	Porous layer with crystalline particles Oxide thickness: 39.9 $\mu$ m	$\alpha$ -Fe <sub>2</sub> O <sub>3</sub> , $\alpha$ -FeOOH	Fe, O, C, Si, S, F, and K
1RF6	Feedwater Heater 1-5-B,	Crystalline and hexagonal particles Oxide thickness: 32.2 $\mu$ m	Fe <sub>3</sub> O <sub>4</sub> , and $\alpha$ -FeOOH	Fe, O, F, and Hg
1RF7	Feedwater Heater 1-4-B, washer	Porous crystalline grains Oxide thickness: 4 $\mu$ m	$\alpha$ -Fe <sub>2</sub> O <sub>3</sub> , $\alpha$ -FeOOH and traces of $\gamma$ -FeOOH	Fe, O, Cr, C, V, F, Zn and Ni
1RF8	Feedwater Heater 1-3-A, washers	Porous crystalline grains Oxide thickness: 19.8 $\mu$ m	$\alpha$ -Fe <sub>2</sub> O <sub>3</sub>	Fe, O, and F
1RF9	Feedwater Heater 1-1B, washers	Crystalline grains forming a porous layer on the surface Oxide thickness: 8.9 $\mu$ m	Inconclusive	Fe, O, Ni, Cr, Cl, V, and F

1RF10	MSR 1-A Tube side	Crystalline particles Oxide thickness: 6.8 $\mu\text{m}$	$\text{Fe}_3\text{O}_4$	Fe, O, Ni, Cr, P, V, and F
1RF11	Main condenser tube side deposit from lower tubes	N/A	$\alpha\text{-FeOOH}$ and $\gamma\text{-FeOOH}$	N/A
1RF12	Station service water line SW-1-003 at 8” flange	Porous layer with sheet like layer	$\alpha\text{-FeOOH}$ and $\gamma\text{-FeOOH}$	O, P, Cl, and Mn

**Table 3.6. Summary of characterization results for the samples collected from unit 2 (2003 Outage)**

Sample Identification	Description	SEM	FTIR	EDS
2RF1	Main Condenser 2-A hotwell, sediment	Porous, flaky particles	$\alpha\text{-Fe}_2\text{O}_3$ , $\text{Fe}_3\text{O}_4$ , $\alpha\text{-FeOOH}$ , and $\gamma\text{-FeOOH}$	Fe, O, Na, Ni, Al, Cr, and Cu
2RF2	Main Condenser 2-B, Supports, deposit	Porous and round particles	$\text{Fe}_3\text{O}_4$	Fe, O, Na, Ni, Al, Cr, and Cu
2RF3	Main Condenser Shell 2-B upper area, metal piece	Porous upper layer with needle like particles at the bottom layer	$\text{Fe}_3\text{O}_4$ and $\alpha\text{-Fe}_2\text{O}_3$	Fe, O, Na, Ni, Al, Cr, Cu, Pb, and Si
2RF4	Feedwater Heater , 2-6-A , washer	Porous top surface covered with platy and round particles with needle like particle at the bottom surface Oxide thickness: 2.1 $\mu\text{m}$	$\text{Fe}_3\text{O}_4$ and $\gamma\text{-FeOOH}$	Fe, O, Si, S, Mn, V, Na, and Ni
2RF5	Feedwater Heater, 2-6-B, washer	Porous layer with platy and needle like particles Oxide thickness: 23.4 $\mu\text{m}$	$\text{Fe}_3\text{O}_4$ , $\alpha\text{-Fe}_2\text{O}_3$ , and $\gamma\text{-FeOOH}$	Fe, O, Cr, Cu, F, Na , and Si,

2RF6	Feedwater Heater 2-5-A, washer	Porous platy particles on the surface with small fibrous like particles underneath the layer Oxide thickness: 36.5 $\mu\text{m}$	$\text{Fe}_3\text{O}_4$ , $\alpha\text{-FeOOH}$ , and $\gamma\text{-FeOOH}$	Fe, O, Na, Cr, Cu, F and Ni
2RF7	Feedwater Heater 2-5-B, washer	Porous crystalline grains with needle or flower like particles present in between the crystalline grains Oxide thickness: 9.9 $\mu\text{m}$	$\alpha\text{-Fe}_2\text{O}_3$	Fe, O, Cr, Cu, F, Na, Ni, Al S, Ti and Si
2RF8	Feedwater Heater 2-4-B, washers	Porous crystalline grains with needle like particles present in between the crystalline grains Oxide thickness: 8.3 $\mu\text{m}$	$\text{Fe}_3\text{O}_4$ , $\alpha\text{-Fe}_2\text{O}_3$ , $\gamma\text{-FeOOH}$ and traces of $\alpha\text{-FeOOH}$	Al, Cr, Fe, Mn, Ni, O, V, Cr, Cu, F, Na and S
2RF9	Feedwater Heater 2-2B, washers	Crystalline grains forming a porous layer on the surface Oxide thickness: 48.0 $\mu\text{m}$	Inconclusive	Fe, O, Na, Ni, Al, Cr, and Cu
2RF10	Feedwater Heater 2-2-B, deposit	N/A	$\alpha\text{-Fe}_2\text{O}_3$ and $\gamma\text{-FeOOH}$	N/A
2RF11	Feedwater Heater 2-2-A, metal piece	Crystalline grains forming a porous layer on the surface	$\alpha\text{-Fe}_2\text{O}_3$ , $\text{Fe}_3\text{O}_4$ , $\alpha\text{-FeOOH}$ , $\gamma\text{-FeOOH}$ and traces of $\gamma\text{-Fe}_2\text{O}_3$	Fe, O, Na, Ni, Al, Cr, and Cu
2RF12	Moisture Separator Reheater 2-A, tube side	Porous layer with crystalline grains on the surface Oxide thickness: 8.3 $\mu\text{m}$	Inconclusive	Fe, O, Al, Cu, Ni, Mn, Mg, Na and Si
2RF13	Moisture Separator Reheater 2-B, tubeside , washer	Long platelets on the surface with cubic crystalline grains at the bottom surface Oxide thickness: 6.1 $\mu\text{m}$	$\text{Fe}_3\text{O}_4$	Fe, O, Al, Cu, Ni, Mn, Mg, F, Na, and K

### 3.5. EDS Quantification of Corrosion Deposits

Deposits consist of different impurities, which include metals like copper, lead, sulfur etc. These metals form different ionic species and some of these species combine with iron oxides and form complex spinels leading to increase in the deposit formation. Ionic species formed in the steam cycle system by some of the major metallic impurities.

This section of the chapter is an attempt to quantify the concentration of the different species (metallic and non-metallic) present in the corrosion deposits from unit 1 (during 2004 refueling outage) and unit 2 (during 2005) outage. These samples were analyzed using EDS system, which was appended to the SEM (JEOL T30). EDS 2004 software provided with EDS set up was used for quantifying the atomic concentrations of elements present in the field samples for unit 1 and unit 2. The total concentration was normalized to 100 weight percent. All the lines (K, L, and M) were used in quantification. ZAF correction along with Gaussian deconvolution (95 % confidence limit) was used in the quantification process. Concentrations of the samples for unit 1 are shown in Table 3.7 and unit 2 is shown in Table 3.8<sup>13</sup>.

The quantification of the major elemental constituents of both units is displayed in Figure 3.12 (a-d). Elemental forms of Fe, Ni and Cr were the major constituents in the deposit samples. Presence of Ni, Fe and Cr is expected in the deposit samples collected from the steam generator system, as the material used in construction is inconel alloy 600 (Ni-65 %, Cr-14 to 17 %, Fe-6 to 10 % and other trace elements like Mn, Si, S and C). The major element in alloy 600 is nickel. Along with the above mentioned elements, Zn, Mg, Si etc were also found in the deposit samples.

Unit 2 main condenser samples showed relatively high concentrations of Ni and Cr when compared to unit 1. Similar contrast was observed between both units in case of low pressure

**Table 3.7. EDS analysis of unit 1, 2004 outage samples**

<b>Sample Identification</b>	<b>Description</b>	<b>Fe</b>	<b>O</b>	<b>Cr</b>	<b>Cu</b>	<b>P</b>	<b>S</b>	<b>Ni</b>	<b>Si</b>	<b>Zn</b>
<a href="#"><u>1RF1</u></a>	Main Condenser 1-A hotwell, sediment	19.7	34.5							
<a href="#"><u>1RF2</u></a>	Main Condenser hotwell, 1-B, deposit	39.5	59.5	0.4	0.5					
<a href="#"><u>1RF3</u></a>	Feedwater Heater 1-6A, washers	25	58.7			8.5				
<a href="#"><u>1RF4</u></a>	Feedwater Heater , 1-6-B , washers	25.8	73.9				0.1			
<a href="#"><u>1RF5</u></a>	Feedwater Heater, 1-5-A, washer	19	58.3				0.1	0.1		
<a href="#"><u>1RF6</u></a>	Feedwater Heater 1-5-B,	24.2	57.4	1.7					7.8	2.8\
<a href="#"><u>1RF7</u></a>	Feedwater Heater 1-4-B, washer	31.5	52.6	2.3				1.7		
<a href="#"><u>1RF8</u></a>	Feedwater Heater 1-3-A, washers	36.5	54.8							
<a href="#"><u>1RF9</u></a>	Feedwater Heater 1-1B, washers	23.8	53	10.2				1.9	0.3	
<a href="#"><u>1RF10</u></a>	MSR 1-A Tube side	25	61.4	6.3		4.7		2.3		

*Note: All the concentrations are in atomic % units*

**Table 3.8. EDS analysis of unit 2, 2005 outage samples**

<b>Sample Identification</b>	<b>Description</b>	<b>Fe</b>	<b>O</b>	<b>Cr</b>	<b>Cu</b>	<b>Mn</b>	<b>Ni</b>	<b>Si</b>	<b>Zn</b>	<b>Cl</b>	<b>Ti</b>
<a href="#"><u>2RF81</u></a>	Main Condenser 2-B hotwell, bolt	15.1	58.1	17.5			9.1				
<a href="#"><u>2RF82</u></a>	Low Pressure Heater 2-4A, washer	22.8	59.2	1.0	2.2	3.9	5.3	0.5	3.1		
<a href="#"><u>2RF83</u></a>	High Pressure Heater 2-1A	1.9	68.6	2.2		2.6	1.1	10.1		1.5	
<a href="#"><u>2RF84</u></a>	High Pressure Heater 2-1B	9.3	61.4	10.7		12.8	5.6				
<a href="#"><u>2RF85</u></a>	SG#1, Steam Drum Deposit	1.0	66	1.1		1.4	0.6				
<a href="#"><u>2RF86</u></a>	SG#2, Steam Drum Deposit	1.0	65.8			1.3	0.5			0.8	1.7
<a href="#"><u>2RF87</u></a>	SG#3, Steam Drum Deposit	1.0	66.2			1.3	0.6				1.8
<a href="#"><u>2RF88</u></a>	SG#4, Steam Drum Deposit	1.0	66.2			1.4	0.6				
<a href="#"><u>2RF89</u></a>	Moisture Separator Reheater 2-A, tube side	9.3	61.4	10.7		12.8	5.6				
<a href="#"><u>2RF810</u></a>	Moisture Separator Reheater 2-B, tube side	0.8	66.1	1.0		1.2	0.5	4.6			

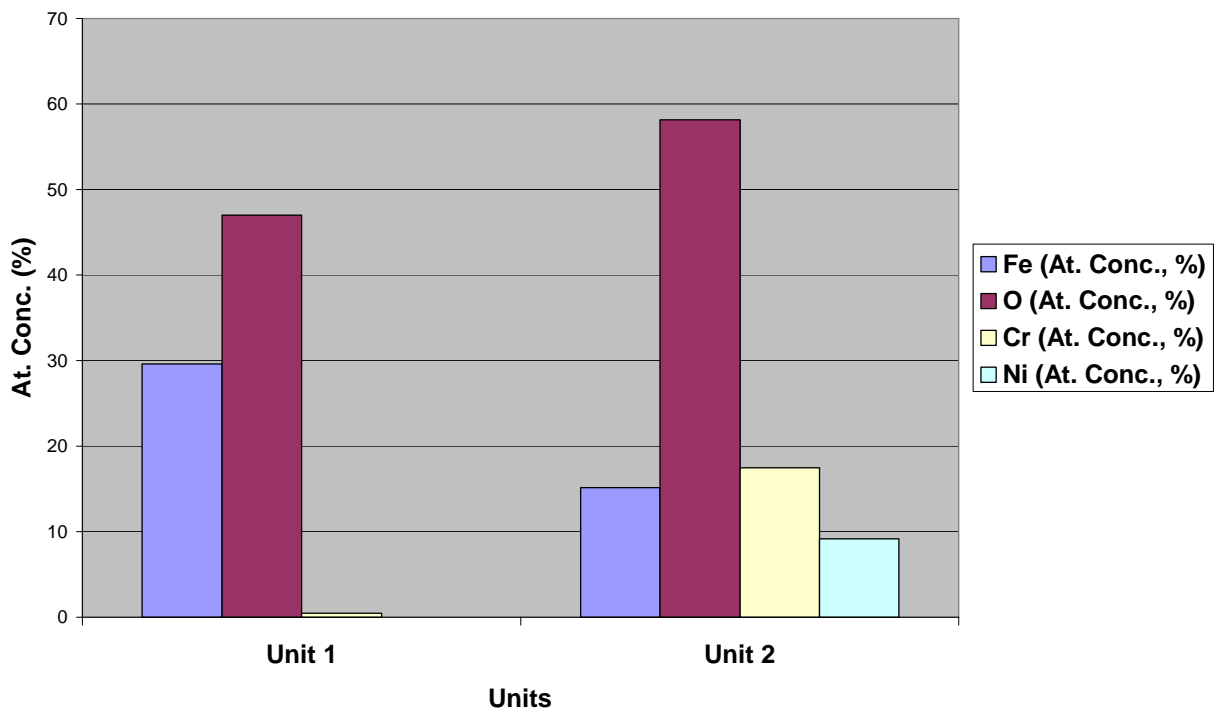
*Note: All the concentrations are in atomic % units*



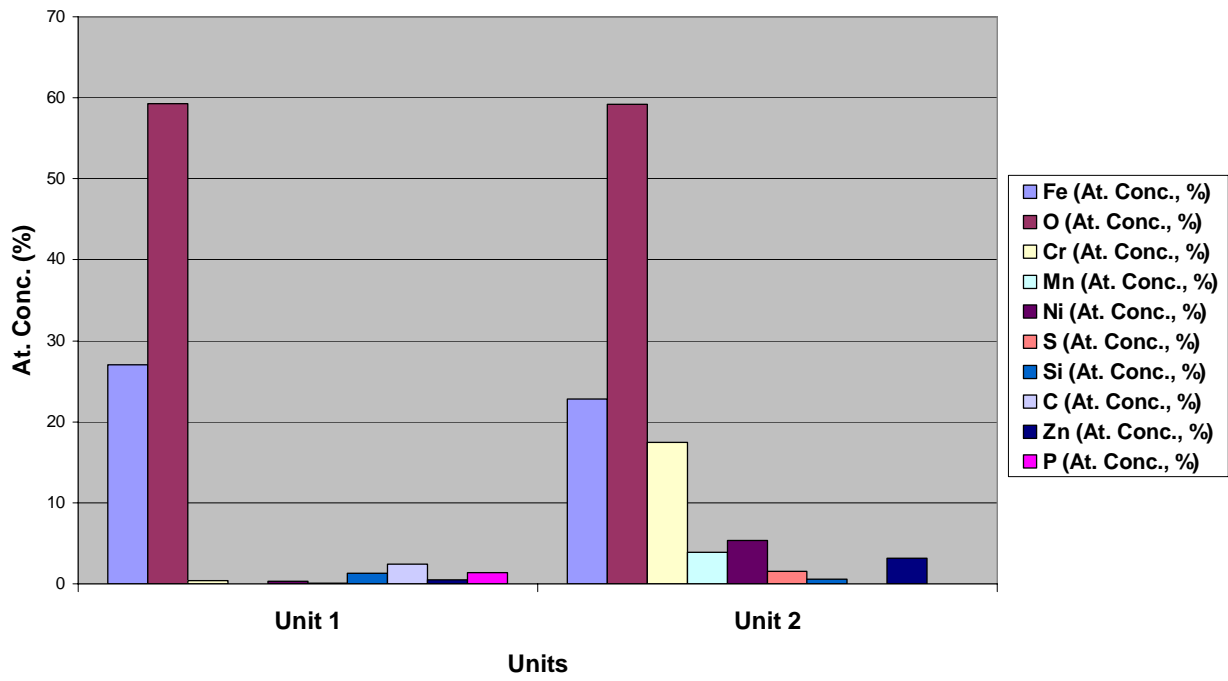
feedwater heaters. Feedwater heaters and moisture separator showed more number of trace elements compared to main condenser in both units 1 and 2.

As discussed in previous sections, the results from EDS analysis reveals that constituents of steam generator tubing and other ferrous and non-ferrous materials used in the construction of the steam generator can be expected to be present in the oxides of the secondary system, though not in homogenous fashion.

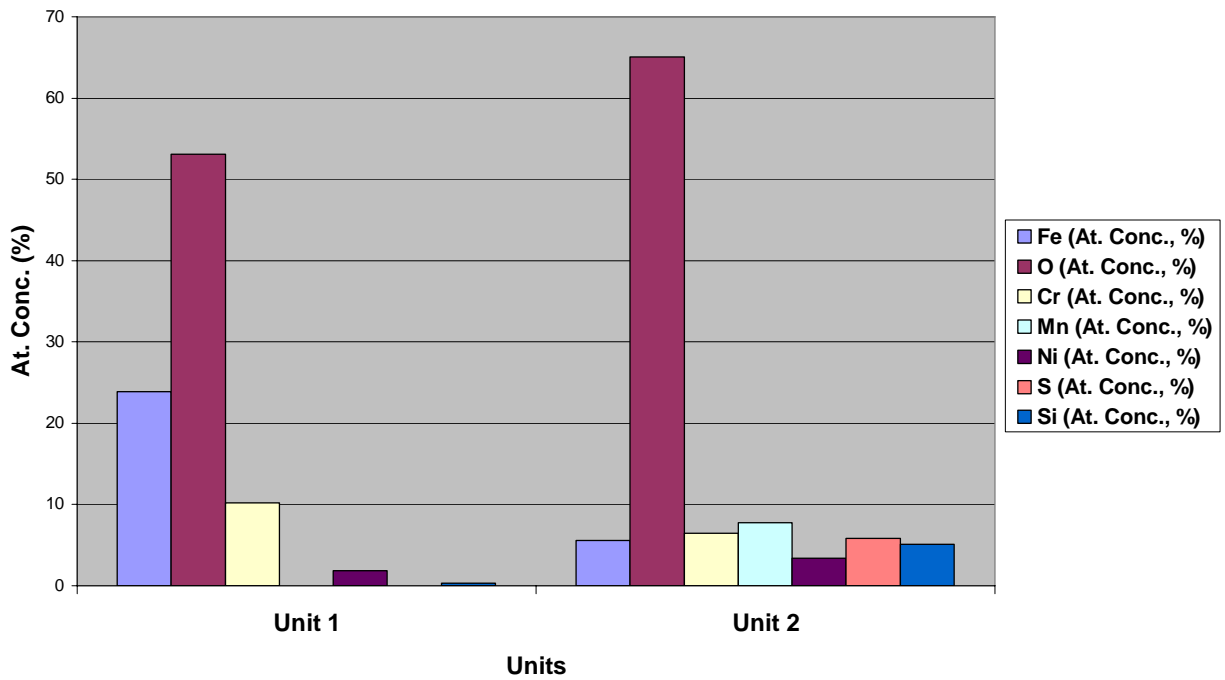
One main reason that justifies EDS quantification of the deposit sample is in documenting the concentrations of the elements for both steam generator units. Any major change in the concentrations for a given unit from one outage to the next outage if analyzed carefully can give very valuable information on corrosion deposits and plant chemistry.



a)



b)



c)

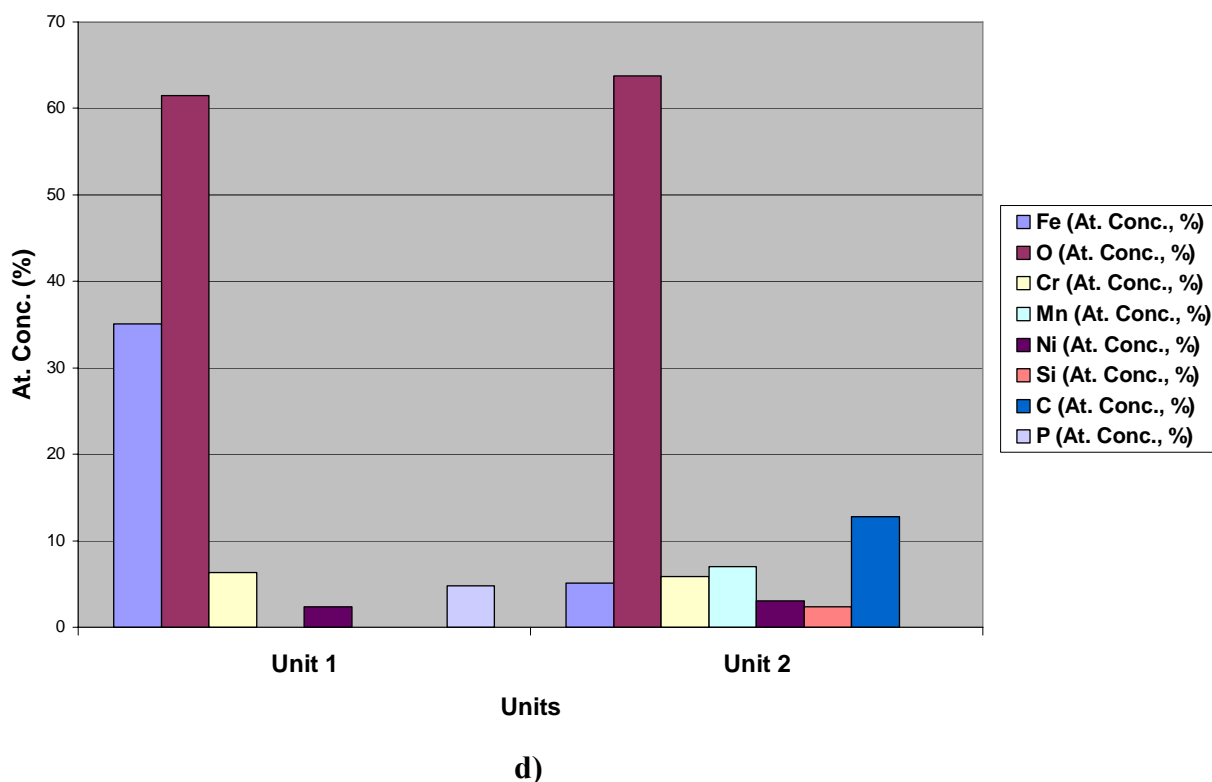


**Figure 3.13. EDS quantification of samples collected from a) condenser, b) LP heaters, c) HP heaters and d) moisture separator)**

### 3.6. Chapter References

1. S. Nasrazadani, and H. Namduri, "Characterization of Iron Oxide Deposits Formed at Comanche Peak Steam Electric Station (CPSES)", Final Report, 2002.
2. Namduri, Haritha, "Characterization of Iron Oxide Deposits formed at Comanche Peak Steam Electric Station", Masters Thesis, University of North Texas, May 2003.
3. Millett, "Recent Advances in Water Chemistry Control at US PWRs", Proceedings of 58<sup>th</sup> International Water Conference, Pittsburgh, October, 1997.
4. R. Varrin, Jr., "Characterization of PWR Steam Generator Deposits", TR-106048, Research Project S523-01, 1996.

5. Millett, "PWR Secondary Water Chemistry Guidelines", TR-102134-R5, Final Report, 2000.
6. Srikantiah.G, Chappidi. P.R., "Particle Deposition and Fouling in PWR Steam Generators", Nuclear Engineering and Design 200 (2000), pp. 285-294.
7. Raymond, De Murcia, A. and Dhaunut, S., "Speciation and Analysis of Corrosion Products in the Primary Coolant of Pressurized Water Reactors", Analytica Chimica Acta 195 (1987), pp. 265-273.
8. Nordmann and Fiquet, "Selection Criteria for the Best Secondary Water Chemistry", Nuclear Engineering and Design 160 (1996), pp. 193-201.
9. Passell, C. S. Welty and S. and A. Hobart "Use of Organic Amines in Water Chemistry Control for Pressurized Water Reactor Secondary Systems", Progress in Nuclear Energy 20 (1987) 3, pp 235-254.
10. Turner and Klimer, "The Effect of Alternative Amines on the Rate of Boiler Tube Fouling", EPRI, 1997, TR-108004.
11. B. Fellers and Jim Stevens, and Orbon, "Strategic Elements of Steam Cycle Control Practices at TXU'S Comanche Peak Steam Electric Station", Chimie 2002, France.
12. B. Sala, P. Combrade, R. Erre, and A. Gelpi, "Local Chemistry and Formation of Deposits on the Secondary Side of Steam Generators. A Laboratory Study", Sixth International Symposium on Environmental Degradation of Materials in Nuclear Power Systems-Water Reactors, San Diego, Aug 1-5, 1993.
13. Stevens, Robert Theimer, Nasrazadani and Namduri, "Secondary System Oxide and Lead Study at Comanche Peak", International Water Conference, October 2006, Juju island, Korea.

## CHAPTER 4

### STUDY OF PHASE TRANSFORMATION IN IRON OXIDES USING LASER INDUCED BREAKDOWN SPECTROSCOPY (LIBS) <sup>1</sup>

#### 4.1. Introduction

Recently laser induced breakdown spectroscopy (LIBS) has gained popularity for elemental analysis of deposits formed in steam generators<sup>1</sup> due to its advantages including speed of analysis, simplicity of sampling and capability of in-situ analysis. The technique involves focusing a laser beam onto a sample to generate spark-induced plasma. Although laser-sample and laser-plasma interactions are not well understood it is known that when the laser pulse of sufficient energy strikes a spot on the sample, the spot temperature instantly increases past its vaporization temperature and results in single or multiple photon absorptions. A portion of the material, which is ablated by the laser, is in the form of particles, free electrons and highly ionized atoms. This expanding plume of material interacts with the laser radiation and forms the plasma. After several microseconds this plasma slows down due to collisions with ambient gas species and starts to decay through radiative, quenching, and electron-ion recombination processes leading to formation of high density neutral species. Atomic and ionic emissions of the plasma are collected by a suitable optical arrangement and analyzed using a time-gatable detector. The output is in the form of spectral lines, which give information on the elemental composition and concentrations<sup>2,3</sup>.

In the past, researchers have studied iron and iron oxides in geological materials using the LIBS technique and were successful in reliably identifying using statistical correlation methods

---

<sup>1</sup> This entire chapter is reproduced with permission from Elsevier. Nasrazadani and Namduri, *Spectrochimica Acta Part B* 61 (2006), pp. 565-571.

over a short spectral window 230-277 nm<sup>4</sup>. Weins et al, showed the presence of dolomite and traces of iron oxides using remote sensing LIBS while studying the rock and soil specimens collected during the May 2000 rover trials at Black Rock Summit, Nevada. The data acquired by LIBS as a function of depth and spatial location was very vital in understanding the extent of sample coatings and compositional and mineralogical diversity in targets during the Mars Exploration Program<sup>5</sup>.

LIBS temporal behavior of many elements for the purpose of elemental identification and quantification has been studied in the past. Radziemski studied temporal history of a laser spark on solid samples in vacuum<sup>6</sup>. Due to the high initial density of free electrons and ions, the spectral broadening is dominated early on by stark effect and as time progresses, the electron density decreases, and recombination occurs and so pressure broadening affects the line width. They also concluded that local thermodynamic equilibrium, which is an essential condition to obtain analytical information from the LIBS was realized after 1  $\mu$ s. Hohreiter and his group explained that the changes in the electron density and plasma absorptivity during the first few nanoseconds affect the interactions between the laser induce plasma and the particle<sup>7</sup>. Sdorra and Niemax studied the neutral and ionic resonance lines of Mg as a function of gate delay for different argon pressures. They observed that the magnesium is strongly ionized within the first microsecond as the vapor pressure of magnesium is relatively high and so evaporates very fast into the plasma when it is still very hot. They also observed that ratio of Mg II line to Mg I line measured in the first microseconds was a direct indication of plasma temperature<sup>8</sup>. Ko et al. used an internal standardization to study the binary alloys using LIBS. They found that the internal standards can be used if the intensities are measured after a certain gate delay, allowing the

atomization of the sample material to be completed. They also found that the gate delay was longer for Cu/Zn alloys (largely different vapor pressures) when compared to Fe/Cr alloys<sup>9</sup>.

Castle and et.al performed time resolved measurements of the intensity variations of five Pb atomic lines along the height of a LIBS plasma at atmospheric conditions. They investigated the temporal and spatial development of lead atomic emission and inferred the populations of these distributions of the upper levels from which the transitions originate<sup>10</sup>. Liu et al measured plasma temperature and electron density using relationship between gate delay vs. irradiance and compared with crater volume measurements<sup>11</sup>.

K. Meissner and his group conducted trace element analysis on solid matrix samples consisting of KBr and two oxides using LIBS. They concluded that the difficulties in quantifying the data were related to matrix effects and self-absorption, but the influence of sample preparation was negligible when compared to LA-ICP-MS (laser ablation inductively coupled plasma, mass spectrometry) technique. So LIBS could be used as an alternative or a complimentary technique to a more precise and sensitive LA-ICP-MS<sup>12</sup>. Galbács and group calculated linear correlation coefficient between spectra of range of certified standards and the spectrum of a reference sample to analyze binary alloys<sup>13</sup>.

Literature indicates applications of LIBS for detection and quantification of elements of industrial importance like Fe<sup>14</sup>, Pb<sup>15</sup>, Al<sup>16</sup>, S<sup>17</sup>, and precious metals<sup>18</sup>. However, little or no information is available for phase identification of oxides<sup>19</sup>. In this research LIBS temporal behavior of each iron oxide is documented to show that iron oxides posses uniquely identifiable LIBS fingerprints. Following sections present LIBS temporal spectra of iron oxides that are complemented with well established FTIR and XRD spectra of the corresponding samples to justify analytical value of LIBS for phase identification of iron oxides.

## 4.2. Experimental Procedure

Synthetic magnetite powder (Iron (II, III) oxide, Puratronic®, 99.997% (metal basis)) was heated at different temperatures: 185-500 °C for different time periods. Tracer 2100 Laser Element Analyzer (see Table 4.1. for LIBS system operational parameters) was used for LIBS analysis. Figure 4.1 shows the LIBS set-up used in this study. LIBS analysis was performed on commercial synthetic magnetite, maghemite, hematite, and wustite powders that were used as reference oxides. Samples were in the form of pellets where 0.62 g of oxide and 0.137 g of KCl ground and pressed using a hydraulic press under a pressure of 4,000 psi. Statistical correlation technique given by Winefordner<sup>4</sup>, the relation between variables with the linear correlation coefficient, has been used to compare the spectra of oxidized samples to those of the standard powders. The equation is:

$$R = \sum_i (x_i - \bar{x})(y_i - \bar{y}) / \sqrt{\sum_i (x_i - \bar{x})^2} \sqrt{\sum_i (y_i - \bar{y})^2}$$

where  $\bar{x}$ , the average of  $x_i$  values and  $\bar{y}$ , the average of  $y_i$  values. The  $R^2$  value that is actually the square of the correlation coefficient,  $R$ , gives the measure of the reliability of the linear relationship between the  $x$  (intensity measured for sample) and  $y$  (intensity measured for standard sample). A value of  $R = 1$  indicates an exact linear relationship between the sample and standard powders.

A ThermoNicolet Avatar 370DTGS FTIR system in transmission mode and Scintag 500 x-ray diffractometer with Cu-K $\alpha$  radiation were used to performed phase identification on these samples as complementary to LIBS.



**Table 4.1.: LIBS system operational parameters**

Type of laser	Nd: YAG
Laser Energy	200 mJ
Spectral range	360-385 nm
Grating	2400 l/mm
Detector gate Width	100 $\mu$ s
Gate delay	1-50 $\mu$ s range
Number of spots or number of laser target areas	6
Number of shots on each spot	9

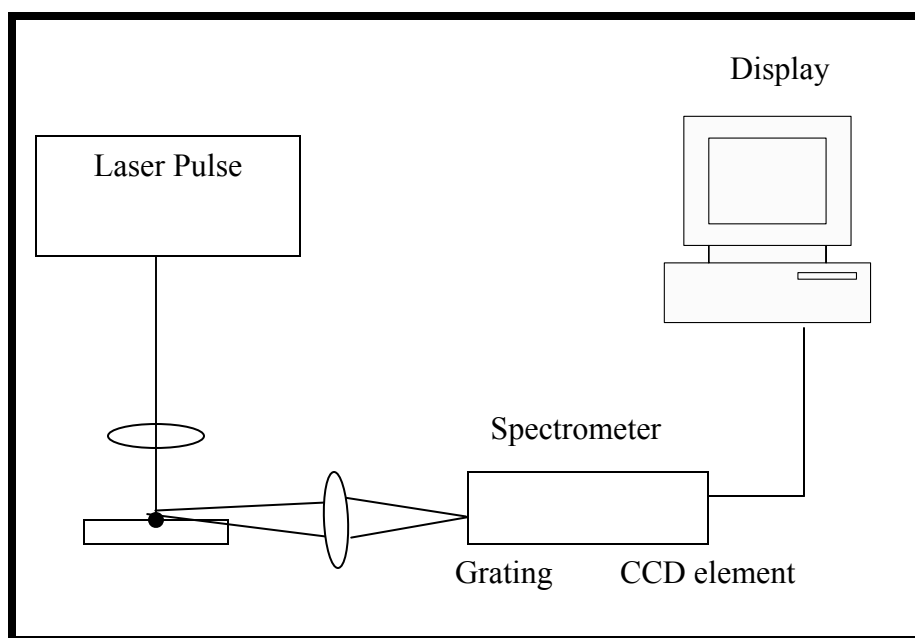


**Figure 4.1. Schematic of laser set-up**

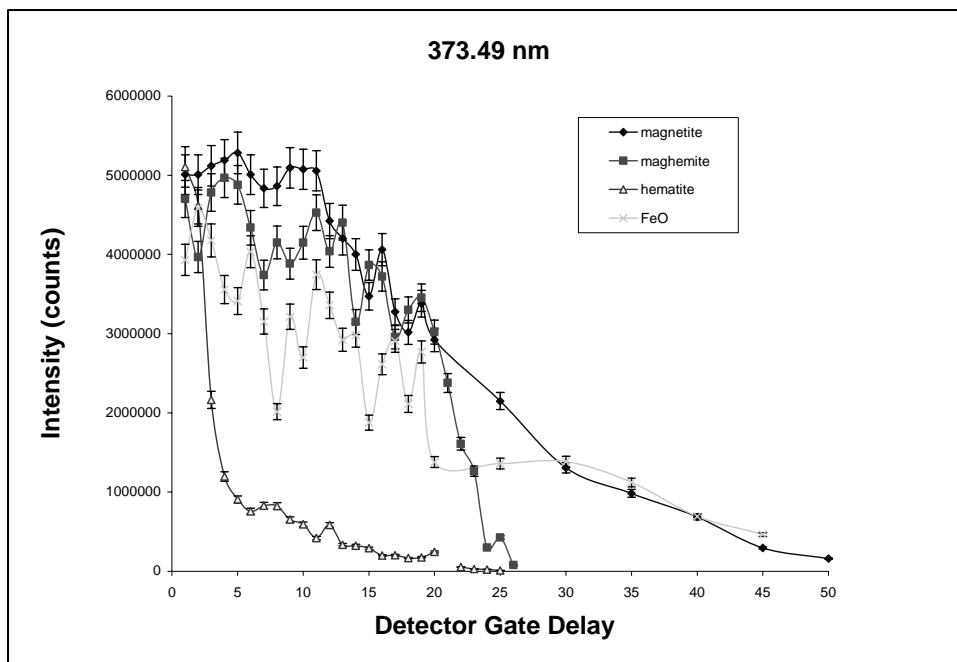
### 4.3. Results and Analysis

#### 4.3.1. Laser Induced Breakdown Spectroscopy

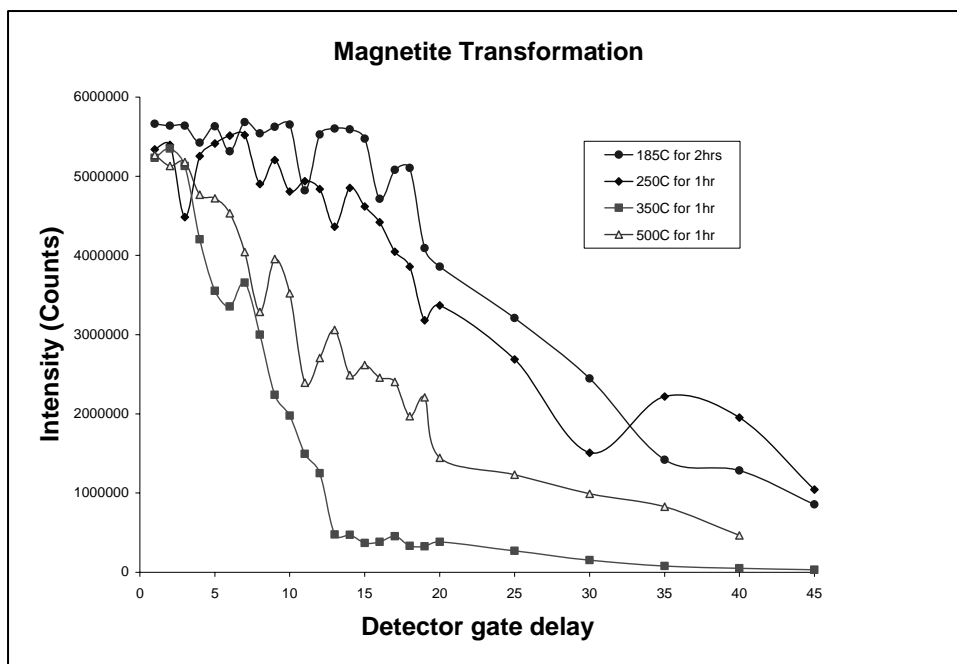
LIBS temporal response of oxides was analyzed in the spectral range from 360-385 nm for gate delays ranging from 1  $\mu$ s to 50  $\mu$ s to identify oxides of iron with the central line being 374 nm wavelength. This wavelength is close to one of the stronger emission lines of Fe I ( $\lambda = 373.48$  nm)<sup>2</sup>. Firstly standard powders of magnetite, maghemite, hematite and FeO were shot with laser beam for the spectral range of 360-385 nm. Figure 4.2 shows the difference in the LIBS spectra for these oxides at 373.49 nm wavelength at pulse width of 100  $\mu$ s. From data presented in Figure 4.2 it was noticed that LIBS spectra of FeO,  $\alpha$ -Fe<sub>2</sub>O<sub>3</sub>,  $\gamma$ -Fe<sub>2</sub>O<sub>3</sub>, and Fe<sub>3</sub>O<sub>4</sub> phases exhibit a number of humps indicating many possible physical processes including radiative, electron-ion recombination, and quenching taking place. LIBS spectrum of hematite ( $\alpha$ -Fe<sub>2</sub>O<sub>3</sub>) showed a remarkably different pattern compared to other oxides possibly because of its crystal structure and absence of ferrous cations in its structure. Major differences in abovementioned iron oxides is the fact that FeO contains only Fe<sup>2+</sup> cations where as  $\alpha$ , and  $\gamma$ -Fe<sub>2</sub>O<sub>3</sub> contains only Fe<sup>3+</sup> cations. The  $\alpha$ -Fe<sub>2</sub>O<sub>3</sub> has hexagonal crystal structures while  $\gamma$ -Fe<sub>2</sub>O<sub>3</sub> has cubic structure. Fe<sub>3</sub>O<sub>4</sub> is a mixed cubic oxide which contains 2/3 Fe<sup>3+</sup> and 1/3 Fe<sup>2+</sup> cations. It is not known if crystal structure, grain size, absorptivity, optical and physical properties of oxides affect the characteristics of the oxide LIBS spectrum but electronic configurations of the oxide must be of prime importance in this regard. Pure iron oxides are very rare and normally iron oxides contain certain degree of atomic vacancies and other structural defects. Variations in oxidation state and presence or absence of structural defects in these oxides are responsible for variation in their LIBS, and FTIR spectra.

Figure 4.2 shows unique steep emission intensity decrease at a particular gate delay for each iron oxide. The gate delay at which this sharp decrease in intensity observed for hematite appeared after 1-2  $\mu\text{s}$  where as other oxides showed a less drastic intensity reduction at gate delay of around 20  $\mu\text{s}$ . Similar data was obtained for all the four commercial oxides at different wavelengths.

Figure 4.3 shows the LIBS data for air-oxidized samples at different temperatures at 373.39 nm wavelength. From the data obtained one can clearly observe that as the oxidizing temperature and time were increased the emission intensity showed a down fall at lower gate delays indicating oxidation of ferrous cations to ferric cations and in turn transformation of magnetite to maghemite before complete transformation to hematite. Specifically, air oxidized samples at 185°C after 2 hours and at 250 °C after 1 hours did not transform magnetite to hematite but it indicated start of transformation as confirmed by  $R^2$  factor shown in Figure 4.4. Figure 4.4 shows correlation of LIBS spectra of oxidized samples to those of commercial oxides



**Figure 4.2. Detector gate delay ( $\mu\text{s}$ ) Vs intensity (counts) for different iron oxides at wavelength  $\lambda = 373.39$  nm at gate width 100  $\mu\text{s}$**



**Figure 4.3. LIBS analysis for magnetite samples treated at a) 185°C, b) 250°C, c) 350°C and d) 500°C at  $\lambda = 373.39$  nm**

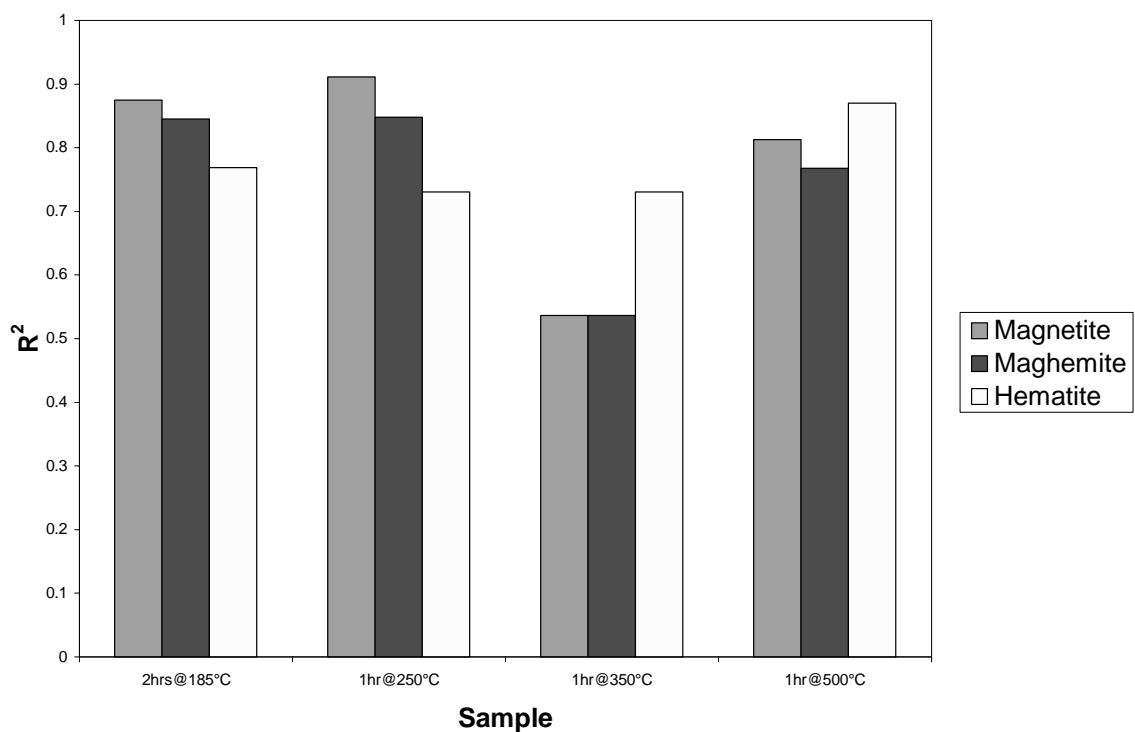


**Figure 4.4. Sample Vs standard oxide,  $R^2$  = correlation coefficient (magnetite/ maghemite/hematite)**

before oxidation. Better correlation of LIBS spectra of the above two oxidized samples to magnetite and maghemite was observed. Oxidized sample at 350 °C for 1 hour produced a better correlation with hematite and a weaker correlation with magnetite as anticipated. Finally oxidized sample at 500 °C for 1 hour showed the best fit to hematite although still no complete transformation to hematite was observed.

Samples heated at 350°C and 500°C showed patterns which were close to standard hematite pattern. Although the sample heated to 350°C for 1 hour showed a decrease in the intensity at a lower gate delay when compared to 500°C sample heated for 1 hour, which was a slight discrepancy from the expected outcome, the above analysis clearly shows that the correlation of the sample at higher temperature was close to unity for hematite when compared to other oxides.

#### 4.3.2. Fourier Transform Infrared Spectroscopy

FTIR spectra of iron oxides are well established<sup>20</sup>. FTIR spectra for magnetite exhibit two strong infrared absorption bands at 570 cm<sup>-1</sup> ( $\nu_1$ ), and 390 cm<sup>-1</sup> ( $\nu_2$ ). According to Ishii et al these bands can be assigned to Fe-O stretching mode of the tetrahedral and octahedral sites for the  $\nu_1$  band at 570 cm<sup>-1</sup> and the Fe-O stretching mode of the octahedral sites for the  $\nu_2$  band at 390 cm<sup>-1</sup> provided that Fe<sup>3+</sup> ion displacements at tetrahedral sites are negligible. FTIR spectrum of magnetite exhibits two other absorption bands at 268 cm<sup>-1</sup> and 178 cm<sup>-1</sup> which were beyond detection limit of our instrument<sup>21</sup>. Maghemite that is defective form of magnetite has absorption bands at 630 cm<sup>-1</sup> and 430 cm<sup>-1</sup>. Previous research shows that the band at 630 cm<sup>-1</sup> was developed from broadening and splitting of 570 cm<sup>-1</sup> band as magnetite was air oxidized at different temperatures<sup>22</sup>. Similar observations are noticed in Figure 4.5.

Magnetite samples heated in air at 185-500 °C for different durations show progression of magnetite transformation to maghemite (250 °C for 1 hour) before it transform to hematite (500 °C for 1 hour). All heated samples show absorption band broadening as well as band splitting in varying degrees when compared with un-oxidized magnetite sample (Figure 4.5). FTIR spectra of Hematite shows absorption band at 540  $\text{cm}^{-1}$  (very broad), and 470  $\text{cm}^{-1}$  (medium broad)<sup>20</sup>.

#### 4.3.3. X-Ray Diffraction

Magnetite samples oxidized at different temperatures were analyzed using XRD as a complementary technique. Figure 4.6 (a-d) shows XRD spectra of oxidized samples documenting transformation of magnetite to hematite. M represents magnetite, MH represents maghemite and H represents Hematite phases in Figure 4.6. Figure 4.6a shows a strong (311) diffraction intensity indicative of strong magnetite presence. Sample heated at 200 °C for 1 hour (Figure 4.6b) shows a reduction in intensity of (311) peak and development of maghemite and hematite peaks. It must be mentioned that XRD is not sensitive enough to differentiate between magnetite and maghemite phases due to extreme similarity in crystal structure of these two phases. Samples heated at 350 °C and 500 °C for 1 hour (Figure 4.6 c-d) are dominated by hematite phase indicated by presence of strong (104), (110), and (116) peaks. Comparing XRD, FTIR, and LIBS spectra of oxidized samples it is observed that there exists a harmony in all three spectroscopic analysis. Magnetite sample heated for 2 hours at 185 °C shows minimal hematite indicated by a minor (104) hematite peak in the XRD spectra and its corresponding FTIR spectrum that shows a minimal hematite absorption band at 444  $\text{cm}^{-1}$ . Correspondingly LIBS pattern does not show an abrupt intensity drop at low gate delays that is a typical hematite

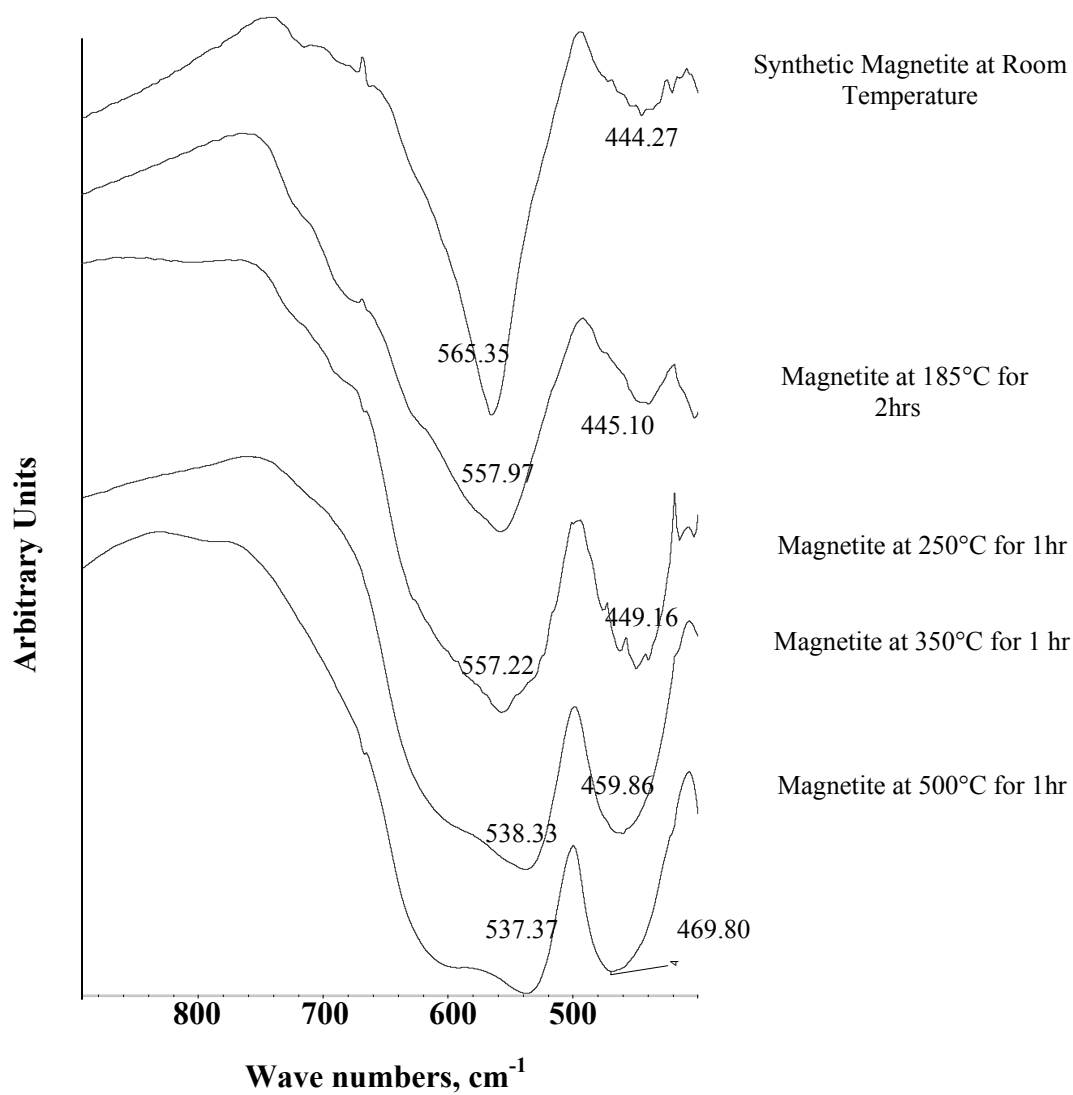


**Figure 4.5. FTIR spectra of magnetite powder heated to different temperatures**

signature in LIBS analysis. On the other hand, highly oxidized sample heated at 500 °C for 1 hour showed an XRD pattern indicating almost complete transformation of magnetite to hematite. Corresponding FTIR pattern shows a band broadening and splitting of 570 cm<sup>-1</sup> band to form two bands at 600 and 630 cm<sup>-1</sup> with increasing intensity in 470 cm<sup>-1</sup> band. LIBS

spectrum of this sample showed a sudden reduction in intensity indicating a strong presence of hematite. There appears to be an anomaly in LIBS spectra of samples heated at 350°C and 500°C heated for the same time period. Figure 4.3 shows an abrupt reduction in intensity for both samples with spectrum of 350 °C samples lying below that of 500 °C sample. It is conceivable that degree of transformation from one sample to the next may vary slightly that leads into an observed variation. However both samples clearly showed a sudden intensity fall out in their LIBS spectra proving the consistency of the analysis.

Therefore one can conclude that LIBS can be used as an alternative or as a complementary technique to FTIR and XRD in identifying the oxides. The main advantage of using LIBS technique for oxide characterization over conventional techniques like FTIR and XRD is that the former can also be used in trace element analysis.

#### 4.4. Summary and Conclusions

According to LIBS correlation data, as the oxidation temperature, time or both increased, the transformation of magnetite to maghemite and then to hematite took place. Good agreement exists in LIBS, FTIR, and XRD data. The in-situ nature, remote analysis and speed of analysis of LIBS can be used in power industries for a better understanding of deposit formation. The future work will involve applying this technique to other metal oxides and complexes not only in the corrosion deposits but also to extend it to different field of studies like environmental and geological.



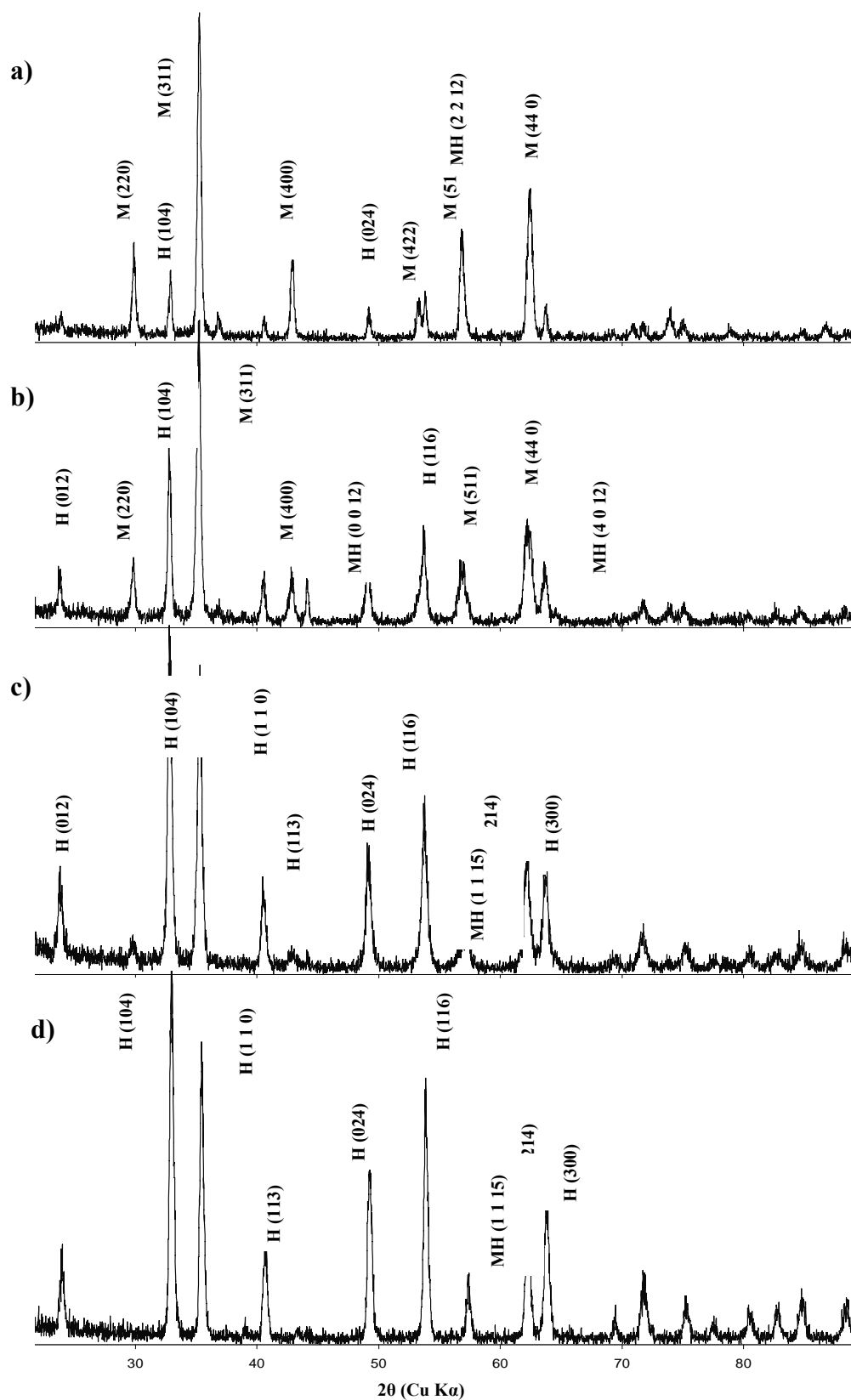


**Figure 4.6. XRD analysis of magnetite samples treated at different temperatures a) 185°C for 2 hrs, b) 250°C for 1 hr c) 350°C for 1 hr and d) 500°C [M-magnetite, MH-maghemite and H- hematite]**

#### 4.6. Chapter References

1. Simon Lawson, Jim Wright, Jim Young, and Andy Whitehouse “In-vessel Material Analysis of AGR Steam Generator Tubes Using a Fiber Probe LIBS Instrument”, LIBS 2000 Conference, Terrenia, Pisa, (Italy), 8-12 October 2000.
2. D. A. Rusak, B. C. Castle, B. W. Smith, and J. D. Winefordner, “Recent Trends and the Future of Laser Induced Plasma Spectroscopy”, Trends in Analytical Chemistry 17 (1998) 8+9, pp. 453-461.
3. J. Lucas, M. Sabsabi, and R. Héon, “Laser –induced breakdown spectroscopy: A New Tool for Process Control”, 16th WCNDT 2004, Montreal, Canada, Aug 30 - Sep 3, 2004, paper code: 679.
4. I. B. Gornushkin, A. Ruíz-Medina, J. M. Anzano, B. W. Smith and J. D. Winefordner “Identification of Particulate Materials by Correlation Analysis Using a Microscopic Laser Induced Breakdown Spectrometer”, Journal of Analytical Atomic spectroscopy, 15 (2000), pp. 581-586.
5. Wiens R.C., Seelos F.P. IV, Ferris M.J., Arvidson R.E., Cremers D.A., Blacic J.D., and Deal K, “Combined Remote Mineralogical and Elemental Identification from Rovers: Field and Laboratory Tests Using Reflectance and Laser-Induced Breakdown Spectroscopy”, Journal of Geophysical research 107 (2002) E11, pp-8003.
6. Leon J. Radziemski, “Review of Selected Analytical Applications of Laser Plasmas and Laser Ablation”, Microchemical Journal 50 (1994), pp. 218-234.
7. V. Hohreiter, J.E. Carranza, and D.W. Hahn “Temporal Analysis of Laser-Induced Plasma Properties as Related to Laser-Induced Breakdown Spectroscopy”, Spectrochimica Acta Part B 59 (2004), pp. 327-333.

8. W. SDorra and K. Niemax, "Temporal and Spatial Distribution of Analyte Atoms and Ions on Microplasmas Produced by Laser Ablation of Solid Samples", *Spectrochimica Acta* Vol. 45B (1990)8, pp. 917-926.
9. J.B. KO, "On the Internal Standardization in Optical Emission Spectrometry of Microplasmas Produced by Laser Ablation of Solid Samples", *Fresenius Z. Analytical Chemistry*, 335 (1989), pp. 648-651.
10. Castle B.C., Visser K., Smith B.W., and Winefordner J.D., "Level Populations in a Laser-Induced Plasma on a Lead Target", *Spectrochimica Acta Part B* 59 (1997), pp.1995-2009.
11. Liu H.C., Mao X.L., Yoo J.H., and Russo R.E., "Early Phase Laser Induced Plasma Diagnostics and Mass Removal during Single-Pulse Laser Ablation of Silicon", *Spectrochimica Acta Part B* 54(1999), pp. 1607-1624.
12. K. Meissner, T. Lippert, A. Wokaun, and D. Guenther, "Analysis of Trace Metals in Comparison of Laser-Induced Breakdown Spectroscopy with LA-ICP-MS", *Thin solid films* 453-454 (2004), pp. 316-322.
13. G. Galbács, Gornushkin I.B., Smith B.W., and Winefordner J.D, "Semi-quantitative Analysis of Binary Alloys using Laser-Induced Breakdown Spectroscopy and a New Calibration Approach Based on Linear Correlation", *Spectrochimica Acta Part B* 56 (2001), pp. 1159-1173.
14. A.I.Whitehouse, J Young, I M Botheroyd, S Lawson, C P Evans, and J Wright, "Remote Material Analysis of Nuclear Power Station Generator Tubes by Laser-Induced Breakdown Spectroscopy", *Spectrochimica Acta part B* 56 (2001), pp. 821-830.
15. R.T. Wainner, R.S. Harmon, A.W. Miziolek, K.L. McNesby, and P.D. French, "Analysis of Environmental Lead Contamination: Comparison of LIBS Field and Laboratory Instruments", *Spectrochimica Acta Part B* 56 (2001), pp. 777-793.

16. Igor V. Cravetchi, Taschuk Mike, Tsui Ying Y., Fedossejevs Robert, “Scanning Microanalysis of Al alloys by Laser –Induced Breakdown Spectroscopy”, *Spectrochimica Acta Part B*, 59 (2004), pp. 439-1450.
17. F. Weritz, Ryahi S., Schaurich D., Taffe A., Wilsch G, “Quantitative Determination of Sulfur Content in Concrete with Laser Breakdown Spectroscopy”, *Spectrochimica Acta Part B* 60(2005) 7-8, pp.1121-1131.
18. M. Corsi, G. Cristoforetti, V. Palleschi, A. Salvetti, E. and Tognoni, “A Fast and Accurate Method for the Determination of Precious Alloys Caratage by Laser Induced Plasma Spectroscopy”, *The European physical journal D* 13 (2001), pp. 373-377.
19. H. Bette and R. Noll, “High Speed Laser-Induced Breakdown Spectrometry for Scanning Microanalysis”, *Journal of Applied Physics* 37 (2004), pp.1281-1288.
20. S. Nasrazadani, and A. Raman, “The Application of Infrared Spectroscopy to the Study of Rust Systems”, *Corrosion Science* 34 (1993) 8, pp. 1355-1365.
21. M. Ishii and M. Nakahira, “Infrared Absorption Spectra and Cation Distribution in (Mn, Fe)<sub>3</sub>O<sub>4</sub>”, *Solid State Communications* 11 (1972), pp. 209-212.
22. S. Nasrazadani and A. Raman, “Formation and Transformation of Magnetite (Fe<sub>3</sub>O<sub>4</sub>) on Steel Surfaces under Continuous and Cyclic Water Fog Test”, *Corrosion*, 49 (1993) 4, pp. 294-300.

## CHAPTER 5

### QUANTITATIVE ANALYSIS OF IRON OXIDES USING FOURIER TRANSFORM INFRARED SPECTROSCOPY

#### 5.1. Introduction

Mixtures of iron oxides were prepared with known compositions containing magnetite ( $\text{Fe}_3\text{O}_4$ ), maghemite ( $\gamma\text{-Fe}_2\text{O}_3$ ), and hematite ( $\alpha\text{-Fe}_2\text{O}_3$ ) for calibration purposes. Calcium oxide (lime) was added to all samples as a standard reference in obtaining the calibration curves. Using regression analysis, relationships were developed for intensity versus concentration for absorption bands corresponding to each phases in their corresponding Fourier transform infrared Spectrophotometer (FTIR) spectrum. Calibration curves so generated were used to quantify unknown field samples that were obtained from components (moisture separators, condensers, and high and low pressure heaters) of the two units (units 1 and 2) of Comanche Peak pressurized water reactor (PWR).

Deposits consist of different impurities, which include metals like copper, lead, sulfur etc<sup>1</sup>. These metals form different ionic species and some of these species combine with iron oxides and form complex spinels leading to increase in the deposit formation. Ionic species formed in the steam cycle system by some of the major metallic impurities are tabulated as shown in the Table 5.1. This attempt to characterize iron oxides can be extended to other metal oxides mentioned in Table 5.1 and can give very valuable information on corrosion deposits.

Legodi and his group performed quantitative analysis on calcium carbonate present in different cement blends using FTIR<sup>2</sup>. Reig and group performed quantitative FTIR analysis on calcium carbonate and silica (quartz) using constant ratio method. The group used potassium ferricyanide as standard and successfully showed the accuracy of quantifying the concentration

of silica and quartz in geological samples using FTIR<sup>3</sup>. The same group also successfully showed that FTIR can be used to quantify butyl acetate and toluene in binary and ternary mixtures using constant method ratio. They used valeronitrile as standard and they also showed that the above method is independent of optical path length<sup>4</sup>. Krivacsy and Hlavay performed four different calibration methods using FTIR for quantifying quartz and calcite in atmospheric aerosols using diffuse reflectance infrared fourier transform spectroscopy. First method involved in calibrating by using single measurement, internal standard for second method, multiple calibrations for third method and the final method involved multiple calibration followed by references reflectance correction. After analyzing the results, they concluded that the final method using reference reflectance correction resulted in the most precise results<sup>5</sup>.

Baucells and group showed that the concentration of caffeine in pharmaceutical mixture can be directly determined using FTIR<sup>6</sup>. Bogard and group developed a method to quantify nitrate ions in ambient aerosols using FTIR. They used calibration standards made from nitrates of ammonium, sodium, calcium, and magnesium. They showed that the absorbance at  $1384\text{ cm}^{-1}$  can be effectively used to quantify nitrates down to  $0.1\text{ }\mu\text{g}$  and  $2430\text{ cm}^{-1}$  peak can be used for samples containing milligrams of nitrate<sup>7</sup>

XRD has been traditionally used to identify mineral samples. One of the limitations of XRD is that it cannot provide accurate quantitative information on amorphous and poorly crystalline samples. Xu and group showed that FTIR can be efficiently used for quantifying minerals. They used a multifunctional analysis which is based on Beer's law to quantify different minerals present in oil wells. In this method the absorbance at a specific wave number is sum of the absorbance of all sample components at that wavenumber<sup>10</sup>.

### 5.1. Major metallic impurities found in steam generator cycle

(Source: (Cornell, 1996), (Ishikawa and others, 2002))

Element	Deposit	Chemical	Ionic species
Iron	Magnetite	$\text{Fe}_3\text{O}_4$	$\text{Fe}^{2+}$ , $\text{Fe}(\text{OH})^+$ , $\text{Fe}(\text{OH})^{3-}$
	Maghemite	$\delta\text{-Fe}_2\text{O}_3$	$\text{Fe}^{3+}$ , $\text{Fe}(\text{OH})_2$ , $\text{Fe}_3(\text{OH})_2^{4+}$
	Hematite	$\alpha\text{-Fe}_2\text{O}_3$	Similar to magnetite
	Ferrous Hydroxide	$\text{Fe}(\text{OH})_2$	Semi-solid (not stable above 125°C)
Copper	Copper oxide	$\text{CuO}$	$\text{Cu}^{2+}$ (pH<6), $\text{CuOH}$ (pH 6 to 9) and $\text{Cu}(\text{OH})_3^-$ (pH >9)
Nickel	Nickel oxide	$\text{NiO}$	$\text{Ni}^{2+}$ , $\text{Ni}(\text{OH})^+$ , $\text{HniO}_2^-$
Chromium	Chromium oxide	$\text{Cr}_2\text{O}_3$	Chromate ions in the presence of $\text{O}_2$
Calcium	Calcium oxide	$\text{CaO}$	$\text{Ca}^+$ , $\text{CaO}$
Aluminum	Alumina	$\text{Al}_2\text{O}_3$	$\text{Al}^{3+}$
Manganese	Magnosite	$\text{MnO}$	$\text{MnO}$
Lead	Litharge	$\text{PbO}$	$\text{Pb}^{2+}$ , $\text{Pb}(\text{OH})_2$
Phosphorus	Phosphorus Pentaoxide	$\text{P}_2\text{O}_5$	$\text{p}^{5+}$
Sulfur	Forms sulfates with all other elements mentioned in the table		
Silicon	Cristobalite	$\text{SiO}_2$	$\text{Si}^{2+}$

Formation and transformation of iron oxides is of interest to a wide variety of industries including steel making, power generating, paint systems, pharmaceutical, petrochemical, to name a few. Standard methods for identifications and characterizations of iron oxides have traditionally been either x-ray diffraction (XRD) or Mössbauer spectroscopy (MS)<sup>11</sup>.

Although these techniques have served industry well in the past they suffer from shortcomings that could be replaced with more recently developed technique of Fourier

transform infrared spectrophotometry (FTIR). MS is a technique that utilizes a live radioactive source, which makes the technique relatively unsafe from operational point of view and poses potential health risk to the operator. Level of operator expertise requirements and along with complexity of spectra interpretation is limitations of the MS technique. XRD that is somewhat easier to operate and interpret its spectra suffers from lack of its ability in differentiating magnetite and maghemite. On the other hand FTIR technique is a fast and reliable method that is widely used for characterization of organic matters but its potentials, as a characterization tool for inorganic materials is untapped. Author has demonstrated applicability of FTIR for qualitative analysis of iron oxides and oxyhydroxides in the past and this paper extends application of FTIR for quantitative evaluation of these materials.

FTIR spectra of iron oxides are well established<sup>12</sup>. It is been observed that the absorption band at high wave number region is due to OH stretching and at lower wave number is because of Fe-O lattice vibration. FTIR spectrum of magnetite exhibits two strong infrared absorption bands at  $570\text{ cm}^{-1}$  ( $\nu_1$ ), and  $390\text{ cm}^{-1}$  ( $\nu_2$ ). According to Ishii et al these bands can be assigned to Fe-O stretching mode of the tetrahedral and octahedral sites for the  $\nu_1$  band at  $570\text{ cm}^{-1}$  and the Fe-O stretching mode of the octahedral sites for the  $\nu_2$  band at  $390\text{ cm}^{-1}$ , provided that  $\text{Fe}^{3+}$  ion displacements at tetrahedral sites are negligible<sup>13</sup>. FTIR spectrum of magnetite exhibits two other absorption bands at  $268\text{ cm}^{-1}$  and  $178\text{ cm}^{-1}$  which were beyond the detection limit of our instrument. Maghemite, (a defective form of magnetite) has absorption bands at  $630\text{ cm}^{-1}$ ,  $590\text{ cm}^{-1}$  and  $430\text{ cm}^{-1}$ . Table 5.2 summarizes possible FTIR peaks for different iron oxides.

The  $\alpha\text{-Fe}_2\text{O}_3$  is easily discerned from  $\gamma\text{-Fe}_2\text{O}_3$  and other spinels using XRD. However, since  $\gamma\text{-Fe}_2\text{O}_3$  and ferrites all have spinel structure; it would be difficult to distinguish from each



other only by means of XRD. Even Mossbauer spectroscopy, which is very sensitive in identifying individual iron oxides, encounters difficulties in analyzing such complex mixtures<sup>14</sup>.

**Table 5.2. Infrared bands of different iron oxides**  
(Source: Cornell and Schwertmann 1996) (Nasrazadani and Raman, 1993)

Iron oxide / Hydroxide	Wave numbers of bands (cm <sup>-1</sup> )
Magnetite (Fe <sub>3</sub> O <sub>4</sub> )	Broad bands at 570 and 400 cm <sup>-1</sup>
Maghemite (γ-Fe <sub>2</sub> O <sub>3</sub> )	700, 640-660, 630, 690 range (Fe-O range)
Hematite(α-Fe <sub>2</sub> O <sub>3</sub> )	540, 478 and 352 cm <sup>-1</sup>
Goethite (α-FeOOH)	1124, 890 and 810 cm <sup>-1</sup> for OH stretch
Lepidocrocite (γ-FeOOH)	1018 cm <sup>-1</sup> (in plane vibration) and 750 cm <sup>-1</sup> (out of plane vibration)

Magnetite is a well known form of iron oxide that forms both at room temperature in crevices between steel plates at elevated temperature inside boiler tubes, heat exchangers etc. The oxidation product of Fe<sub>3</sub>O<sub>4</sub> is either γ-Fe<sub>2</sub>O<sub>3</sub> or α-Fe<sub>2</sub>O<sub>3</sub> depending on the oxidation temperature and or possibly crystallite size of the starting magnetite. Both Fe<sub>3</sub>O<sub>4</sub> and γ-Fe<sub>2</sub>O<sub>3</sub> has the same spinel structure and it is very difficult to differentiate between them using XRD<sup>15, 16</sup>.

FTIR instrumentation that is available in most labs is fairly easy to use and the spectra of spinel samples obtained can provide valuable information in this regard<sup>17</sup>. It has been shown in previous studies that FTIR spectra of oxidized magnetite samples are known to show five variations in their absorption bands indicating the different degrees of oxidation and the cation vacancy contents of the spinel phase.

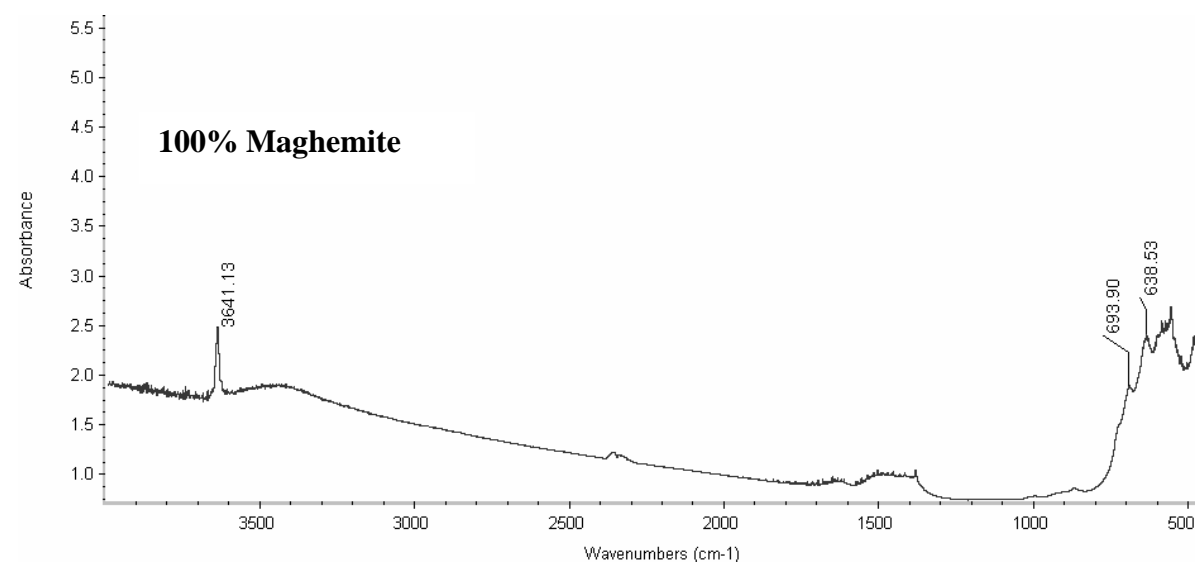
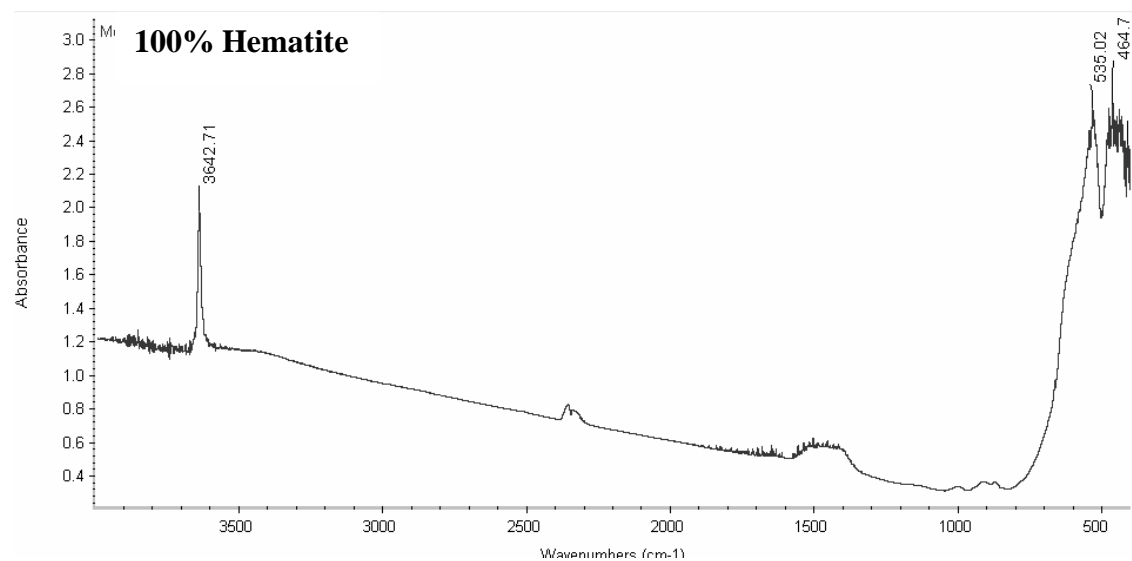
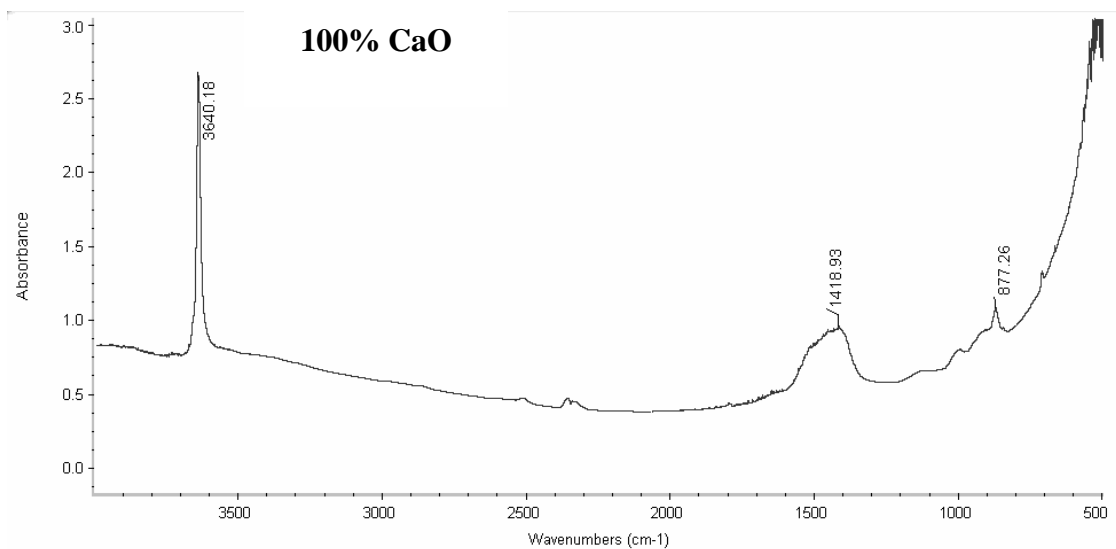
## 5.2. Experimental Procedures

Three sets of samples were prepared. The first set consisted of samples where known concentrations of synthetic magnetite were added to known concentration of synthetic maghemite powder. Similarly the second set consisted of samples where maghemite was added to hematite. The third set consisted of samples where magnetite was added to hematite. All the samples were added to KBr powder and compressed into pellets using hydraulic press. Care was taken to make sure sample preparation was consistent for all the samples. Nicolet Avatar 370 DTGS FTIR was used to quantify iron oxides. The samples consisted of 85-90% of KBr and the rest consisted of equal amounts of CaO (lime) and iron oxide. A resolution of  $2\text{ cm}^{-1}$  was used and the spectra were accumulated over 32 scans. Once all the spectra for the samples were obtained three calibration curves were drawn for the three sets of samples. To set the calibration curve for known amounts of iron oxide (magnetite, maghemite and hematite) in each mixture,  $I/I_0$  ratio was used. Here  $I$  represents the intensity of the iron oxide peak (hematite- $540\text{ cm}^{-1}$  and maghemite  $630\text{ cm}^{-1}$ ) and  $I_0$  represent the intensity of  $3640\text{ cm}^{-1}$  peak of CaO. This particular peak of CaO used primarily because it does not interfere with any of the iron oxide peaks. Even though this peak is close to OH band, it has very distinct peak and can be easily discerned (Figure 5.1).  $\text{CaCO}_3$  ( $894\text{-}865\text{ cm}^{-1}$  peak) has been previously used as a standard reference in quantifying the amount of limestone in different cement blends<sup>2</sup>. Linear fit was used to obtain the calibration curve. This calibration curve was used to quantify the amount of iron oxides present in the field samples collected from the secondary side of Comanche Peak Steam Electric Station (CPSES).

### 5.3. Results and Discussions

Figure 5.1 shows FTIR spectra of hundred percent calcium carbonate, hematite, magnetite and maghemite. A sharp peak at  $3640\text{ cm}^{-1}$  belonging to calcium oxide was observed in all the spectra of iron oxides. The peak intensity was fairly constant in all the spectra.

Calibration curves were obtained for combination of two phases of iron oxides. A correlation factor of 0.933 (magnetite added to maghemite, Figure 5.2), 0.9305 (maghemite added to hematite, Figure 5.3) and 0.8622 (magnetite added to hematite, Figure 5.4) was obtained. A confidence limit of 95% was used in the calculations. The values of  $I/I_0$  for mixture with different concentrations of iron oxides is shown in the Table 5.3. Hematite peak at  $540\text{ cm}^{-1}$  intensity was used for  $I$  value for mixtures containing hematite and magnetite, and maghemite and hematite. Peak at  $630\text{ cm}^{-1}$  was used for  $I$  values in case of mixture containing magnetite and maghemite. These calibration curves were then used to quantify the iron oxide phases present in the field samples collected from secondary side of unit 1 and unit 2 of CPSES. Figure 5.5 shows the spectra for the samples collected from moisture separator, main condenser, main feedwater heater, high and low pressure feedwater heaters. The percentage concentrations of the iron oxides present in the selected field samples is given in Table 5.4. The samples from moisture separator mainly showed hematite and magnetite. The main feedwater heater sample showed almost equal concentrations of magnetite and maghemite. The high pressure feedwater heater sample showed mostly hematite whereas low pressure feedwater heater sample showed hematite and magnetite. Presence of magnetite and hematite is expected in feedwater systems due to the transformation of hydroxides and other hydrated iron species, which move through the feedwater system, into stable iron oxides (Schikorr reaction). The two samples from main condenser mainly consisted of hematite and magnetite with traces of maghemite.



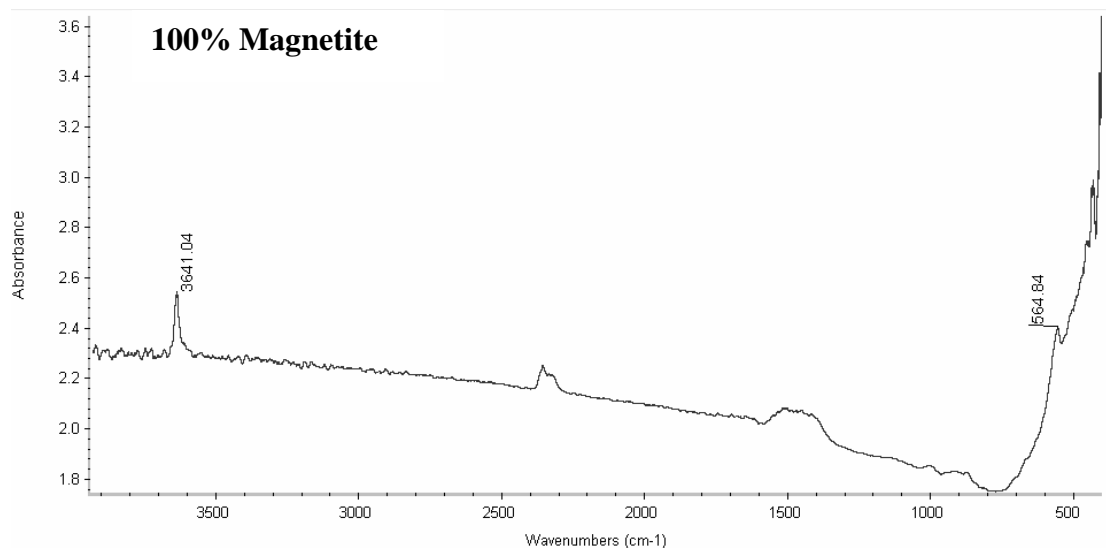
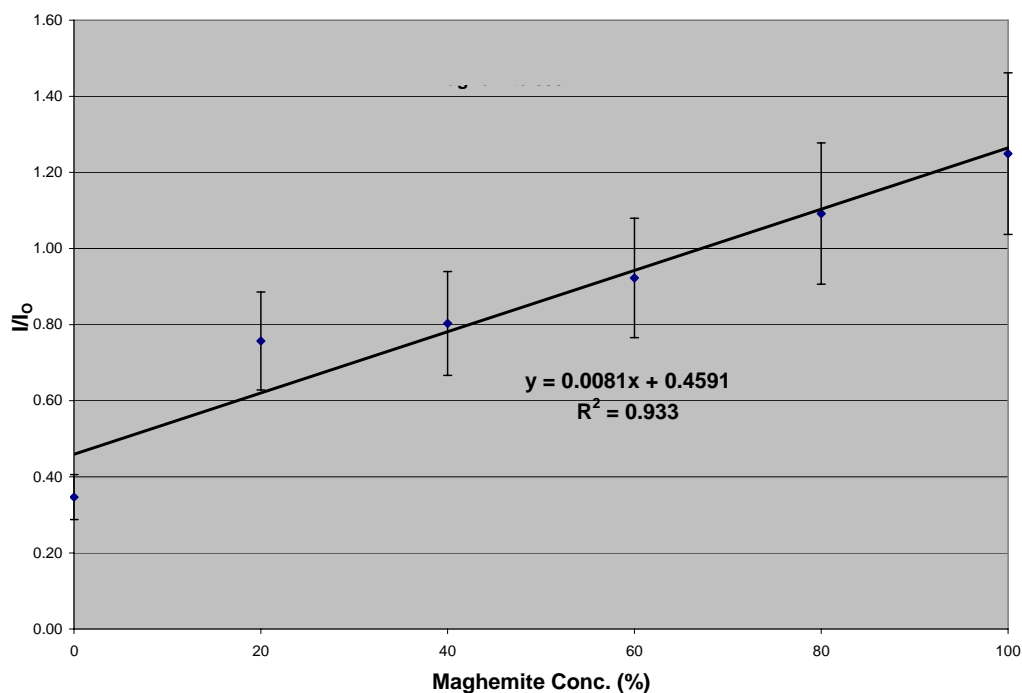


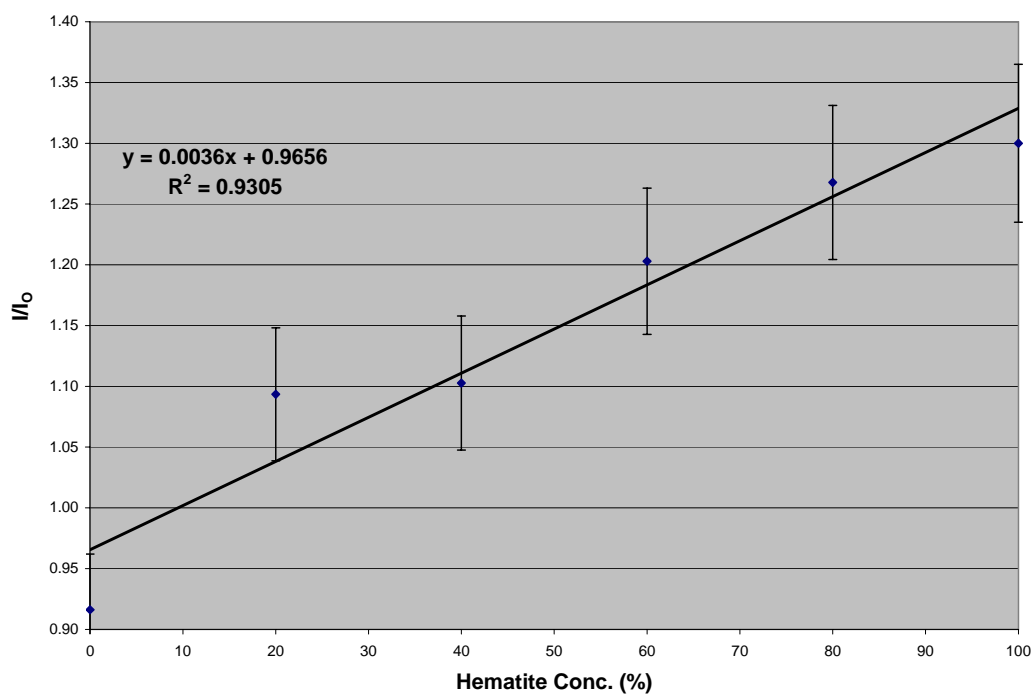
**Figure 5.1. FTIR spectra of 100% CaO, hematite, maghemite and magnetite**

**Table 5.3. FTIR intensities for different known concentrations of iron oxides used in calibration curves ( $I$  = intensity of iron oxide mixture, and  $I_0$  = intensity of  $3640\text{ cm}^{-1}$  peak of CaO)**

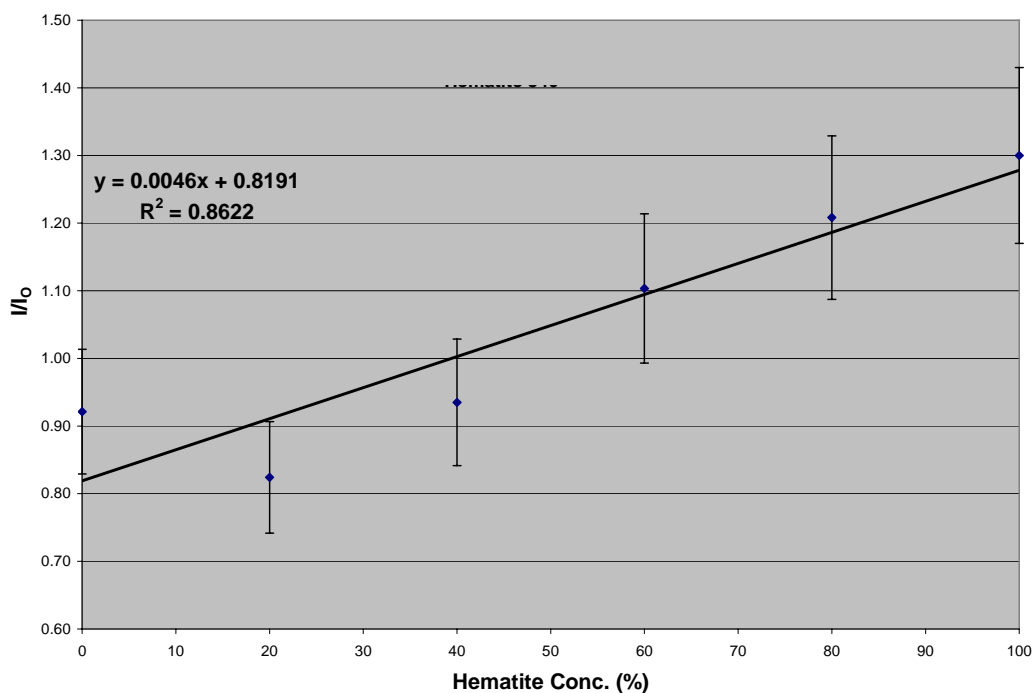
Hematite (%)	Magnetite (%)	Maghemite (%)	$I/I_0$
100			1.30
	100		0.92
		100	0.92
80	20		1.21
60	40		1.10
40	60		0.94
20	80		0.82
80		20	1.27
60		40	1.20
40		60	1.10
20		80	1.09
	20	80	1.09
	40	60	0.92
	60	40	0.80
	80	20	0.76



## 5.2. FTIR calibration for mixture containing magnetite and maghemite (630 $\text{cm}^{-1}$ peak for maghemite)



## 5.3. FTIR calibration for mixture containing hematite and maghemite (540 $\text{cm}^{-1}$ peak for hematite)

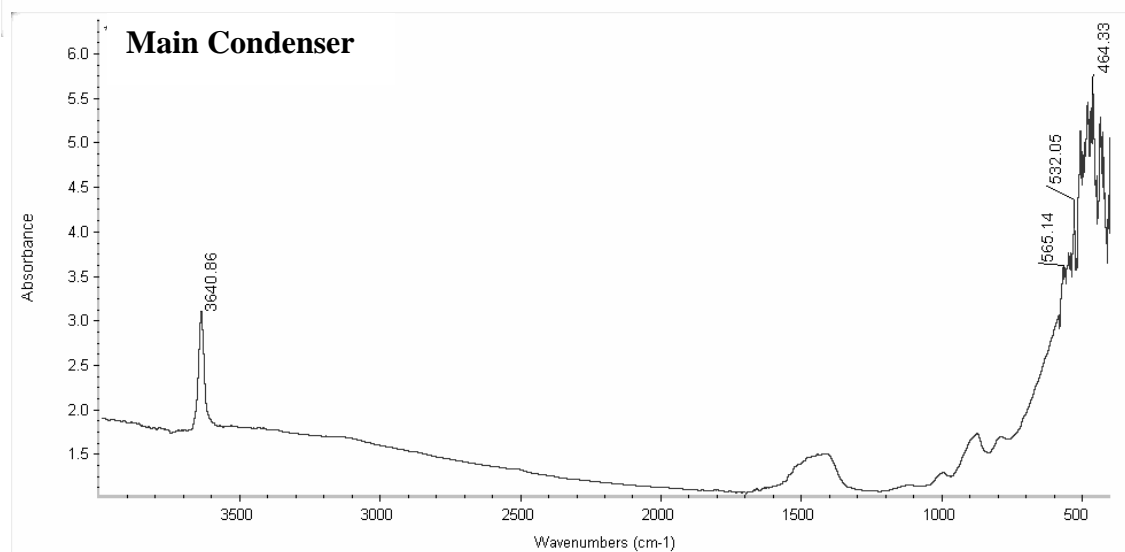
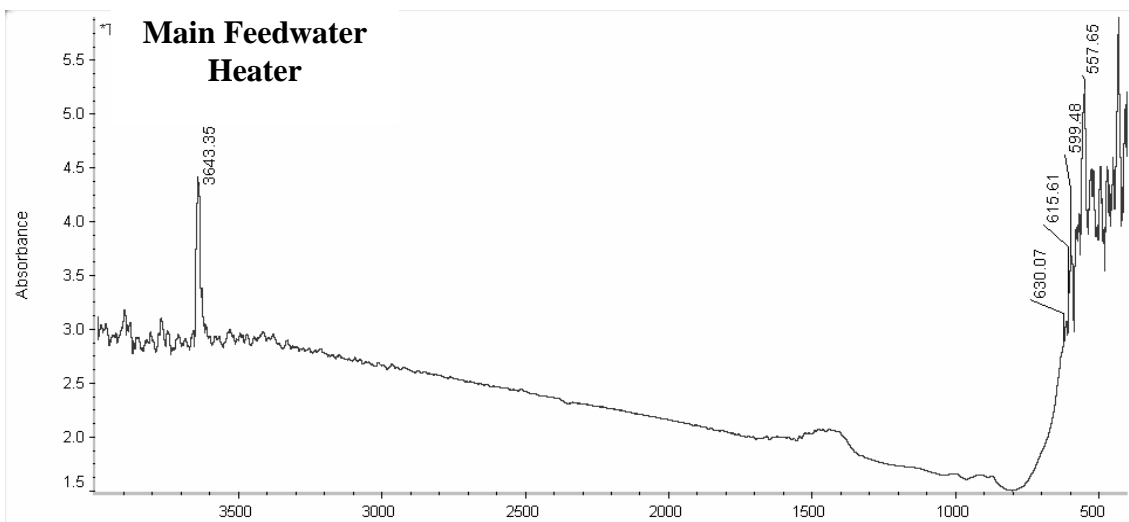
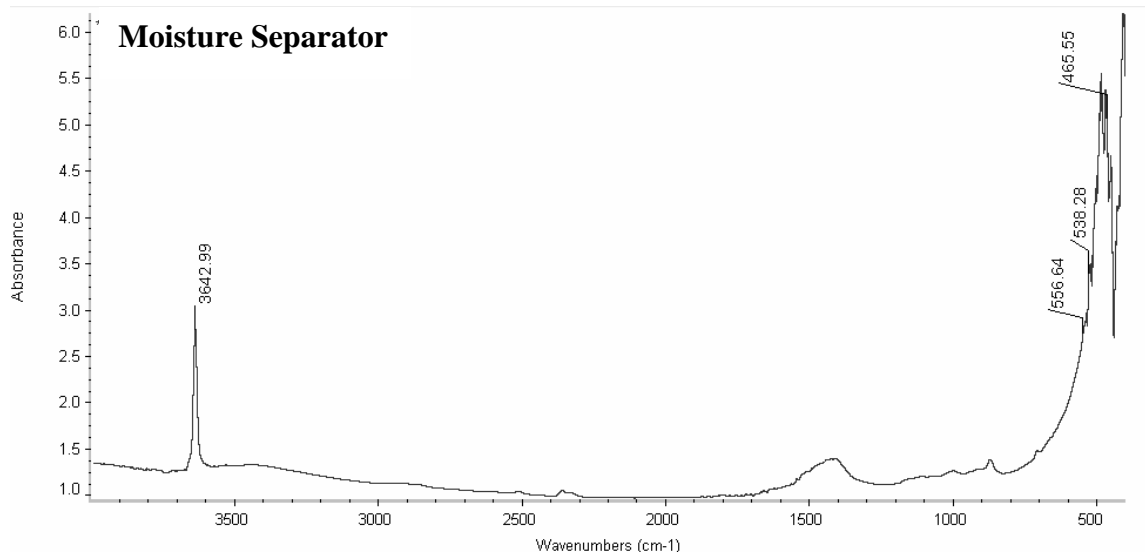


#### 5.4. FTIR calibration for mixture containing magnetite and hematite (540 cm<sup>-1</sup> peak for hematite)

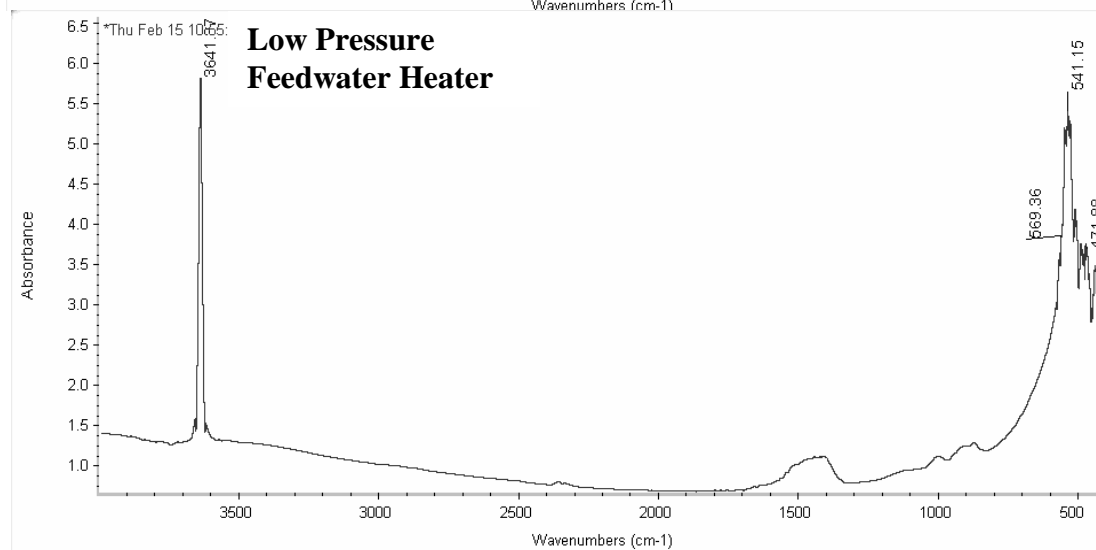
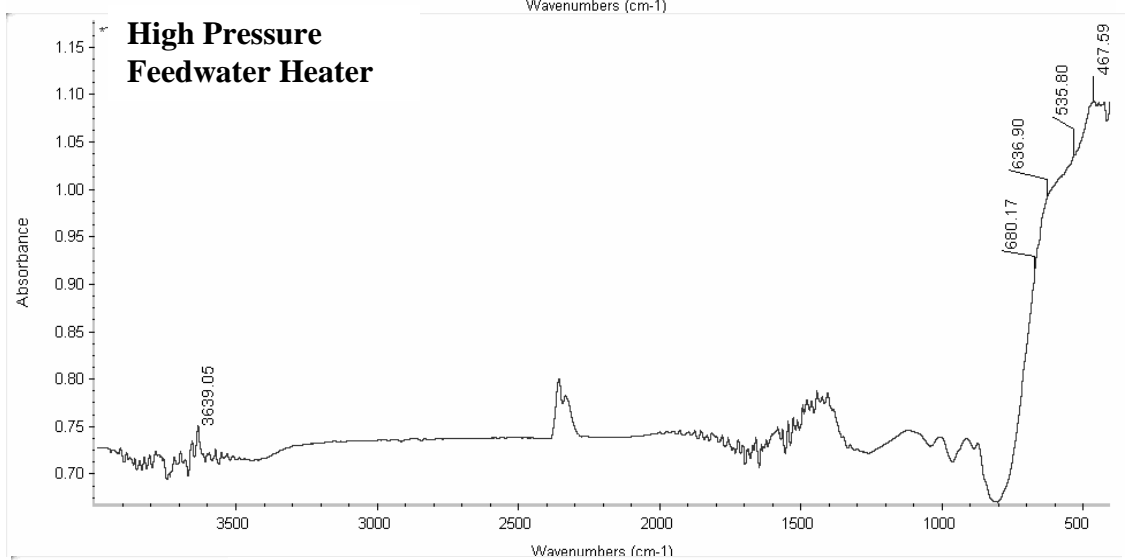
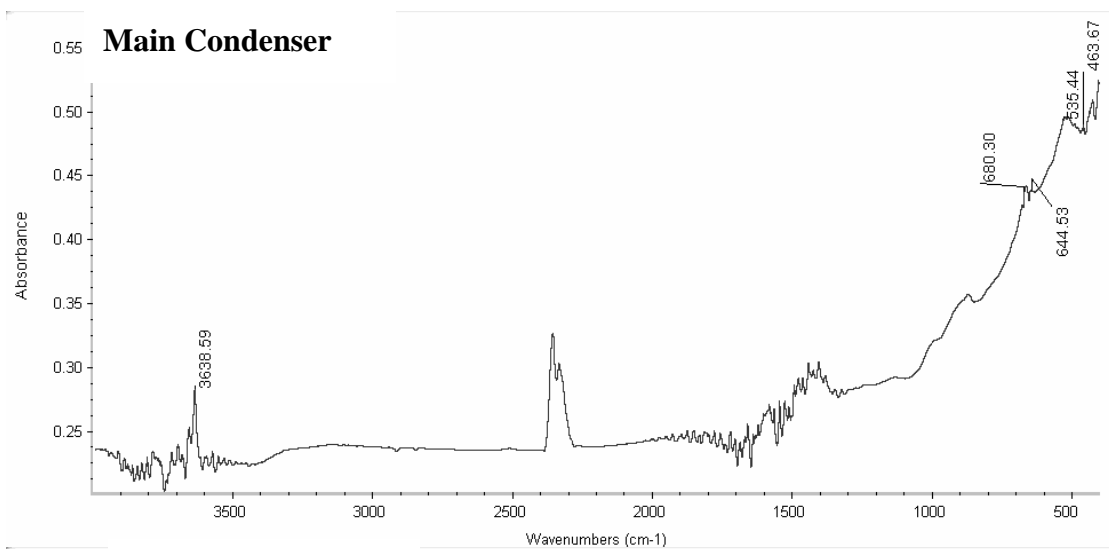
#### 5.4. Summary and Conclusions

A quantitative determination of iron oxides can be quickly and relatively accurately performed using FTIR technique. The technique involves taking mid infrared measurements with samples in the form of KBr pellets. By using a standard reference like CaO normalization can be performed. The peak 3450 cm<sup>-1</sup> is free from interference with any of the major iron oxide peaks considered in this study. This method makes it a very suitable method in quickly determining the concentrations of major iron oxides in the power industry.

Fourier transform infrared spectrophotometry (FTIR) technique was reconfirmed to be a valuable tool to differentiate between Fe<sub>3</sub>O<sub>4</sub> and γ-Fe<sub>2</sub>O<sub>3</sub>. It is also been shown that this technique can be used in quantifying iron oxides.







## 5.5. FTIR spectra for samples collected from secondary side of SG at CPSES

**Table 5.4. Concentration of field sample collected from different components of secondary side of unit 1 and unit 2 steam generator system of CPSES**

<b>Field Samples</b>	<b>Sample Description</b>	<b>Oxides Present</b>	<b>I<sub>o</sub></b>	<b>Magnetite (I)</b>	<b>Maghemite (I)</b>	<b>Hematite (I)</b>	<b>I/I<sub>o</sub></b>	<b>Final Concentrations</b>
1	Moisture Separator	Magnetite and Hematite	3.02	2.48		2.851	0.94	83 % Hematite and 17 % Magnetite
2	Main Feedwater Heater	Magnetite and Maghemite	4.29	5.206	2.811		0.66	54% Magnetite and 46% Maghemite
3	Main Condenser, Hotwell	Magnetite and Hematite	3.08			4.016	1.3	18 % Magnetite and 82 % Hematite
4	Main Condenser	Maghemite and Hematite	0.28			0.4916	1.74	3% Maghemite and 97% Hematite
5	High Pressure Feedwater Heater	Maghemite and Hematite	0.75			1.0352	1.38	3% Maghemite and 97% Hematite
6	Low Pressure Feed Water Heater	Magnetite and Hematite	5.81			5.376	0.93	18% Magnetite and 82% Hematite

It has also been shown that the infrared active mode of calcium oxide can be efficiently used in quantification process. The FTIR quantification method performed in this study can be further fine-tuned and extended to other major metallic oxides like chromium oxide, nickel oxide, lead oxide, silicon dioxide and etc.; can give very valuable information on corrosion deposits formed in nuclear power plants.

### 5.5. Chapter References

1. Cyrus .B.H and Maggi. R. J Jr., “Steam Generator Deposit Trends and Characterizations for Operating Nuclear Power Stations”, 2003 Steam Generator Secondary Side Management Conference, February 10-12, 2003.
2. Legodi, D. De Waal, and J. H. Potgieter “Quantitative Determination of  $\text{CaCO}_3$  in Cement Blends by FT-IR”, Society for Applied Spectroscopy 55 (2001) 3, pp. 361-365.
3. Reig, Adelantado J.V.G., and Moya Moreno M.C.M, “FTIR Quantitative Analysis of Calcium Carbonate(calcite) and Silica (quartz) Mixtures Using the Constant Ratio Method. Application to Geological Samples”, Talanta 58 (2002), pp. 811-821.
4. Reig, Gimeno Adelantado J. V., Peris Martinez V., Moya Moreno M. C. M., and Domenech Cerbo M. T., “FT-IR Quantitative Analysis of Solvent Mixtures by the Constant Ratio Method”, Journal of Molecular Structure 480-481 (1999), pp. 529-534.
5. Krivacsy and Hlavay, “Comparison of Calibration Methods in Quantitative Diffuse Reflectance Infrared Spectroscopy”, Talanta 42(1995)4, pp. 613-620.
6. Baucells M., Ferrer N., Gomez P., Lacort G., and Roura M., “Quantitative Analysis of Caffeine Applied to Pharmaceutical Industry”, Journal of Molecular Structure 294 (1993), pp. 219-222.

7. James S. Bogard, Stanley A. Johnson, Romesh Kumar, and Paul T. Cunningham, "Quantitative Analysis of Nitrate Ion in Ambient Aerosols by Fourier Transform Infrared Spectroscopy", *Environmental Science and Technology* 16(1982), pp. 138-140.
8. Cornell R.M and Schwertmann. U, "The Iron Oxides", Weinheim, New York, 1996.
9. Ishikawa, Kumagai, Yasukawa, Kandoi, Nakayama, and Yuse, "Influences of Metal Ions on the Formation of  $\gamma$ -FeOOH and Magnetite Rusts", *Corrosion Science* 44 (2002) 1073-1086.
10. Xu, B.C. Cornilsen, D.C. Popko, B. Wei, W.D. Pennington, and J.R. Wood, "Quantitative Mineral Analysis by FTIR Spectroscopy", *The Internet Journal of Vibrational Spectroscopy* 5 (2001) 4, pp. 1-12.
11. Blesa, A. J. G. Maroto, S. I. Passaggio, F. Labenski and C. Saragovi-Badler, "Moessbauer Study of the Behaviour of Synthetic Corrosion Products of Nuclear Power Plants", *Radiation Physical Chemistry* 11(1978), pp. 321-326.
12. S. Nasrazadani, and A. Raman, "The Application of Infrared Spectroscopy to the Study of Rust Systems", *Corrosion Science* 34 (1993), No. 8, pp. 1355-1365.
13. M. Ishii and M. Nakahira, "Infrared Absorption Spectra and Cation Distribution in  $(\text{Mn,Fe})_3\text{O}_4$ ", *Solid State Communications* 11(1972), 209-212.
14. Wen-Qing Xu, Yuan-Gen Yin, Guo-Yin Li, and Shu Chen, "Preparation of Mono-Phasic Iron Oxides and Ferrite Spinel and Analysis of their Mixtures", *Applied Catalysis A: General*, 89 (1992) 117-129.
15. Nasrazadani. S and Raman. A, "Application of IR Spectra to Study the Rust Systems", *Corrosion Science* 34 (1993) 8, pp. 1335-1365.

16. Nasrazadani, Namduri, Steven, Theimer and Fellers, "Application of FTIR in the Analysis of Iron Oxides and Oxyhydroxides Formed in PWR Secondary System", 2003 Steam Generator Secondary Side Management Conference, February 10-12, 2003.
17. Brundle Richard, Charles Evans and Wilson, "Encyclopedia of Materials Characterization", Butterworth-Heinemann, 1992, ISBN 0-7506-9168-9.

## CHAPTER 6

### STUDY OF INTERACTION BETWEEN AMINES AND INCONEL ALLOYS

#### 6.1. Introduction

DMA, ETA and morpholine are three popular amines used in water treatment for controlling corrosion and fouling in recirculating nuclear steam generators. Amines in the past have proven to be effective in inhibiting corrosion in steels. Inhibitors, such as amines, are known to protect the metals by absorbing onto the surface and retard metal corrosion. The presence of nitrogen or a heteroatom in an organic compound with unsaturated bonds causes an adsorption process on the metal surface and therefore reduces the metal dissolution<sup>1, 2</sup>. Du, and et al. <sup>1</sup>studied the effect of N, N-dipropynoxy methyl amine trimethyl phosphonate as a corrosion inhibitor for iron in sulfuric acid and used potentiodynamic polarization and impedance spectrum analysis techniques to conclude that the inhibitor showed mixed control.

AC-impedance technique has been extensively used in corrosion studies. It has been proven to be a useful technique for investigating charge transfer, ion transport and adsorption processes on metals<sup>3</sup>. Impedance analysis consists of applying a broad range of frequencies of AC signals to a solid state or aqueous system. AC voltage or current is applied and response in the form of impedance is measured. The data obtained is in the form of real and imaginary impedance. From this data the value of impedance ( $Z$ ) is calculated. Nyquist plot is a plot between real and imaginary values of impedance<sup>4</sup>. Researchers have used AC-impedance in investigating the mechanism of corrosion processes occurring at the metal as well as many other corroding interfaces. Lu and his group<sup>5</sup> studied the corrosion behavior of steels exposed to Bayer liquor at high temperatures. They found that the corrosion rates measured using AC-impedance

was in good agreement with the values obtained from weight loss measurements. The effect of relative humidity on the atmospheric corrosion of galvanized steel coated with organic coatings was studied by Dehri and group<sup>6</sup>. They have suggested a new approach of simulating Nyquist plots. Corrosion resistance of 19 different alloys was tested under conditions similar to Space Transportation System (STS) launch environment by a group from NASA<sup>7</sup>. The group analyzed the corrosion data quantitatively using Nyquist plot and qualitatively using Bode plot. From the polarization resistance ( $R_p$ ) values obtained they found that hastelloy C-22 had higher  $R_p$  values and Monel 400 and inconel 600 had the lowest values. They also found that the measured values of  $R_p$  were in good agreement with the predicted values.

All the components of an electrochemical cell can be correlated to an electronic circuit model consisting of an array of capacitors and resistors (Figure 6.1). Applying the principle of AC-impedance to electronic circuit helps in designing or simulating an equivalent circuit, which when compared to the impedance system can be explained in terms of physical or chemical process<sup>8</sup>. Park and Pyum analyzed the impedance spectra of pitted inconel alloy 600 electrode in aqueous  $\text{Na}_2\text{S}_2\text{O}_3$  and  $\text{NaCl}$  solution at high temperatures. From the Nyquist plots they observed that the spectrum was divided into two sections at temperatures from 60° to 150°C with different slopes<sup>9</sup>. They concluded that the section with the smaller slope in lower frequency range was due to combination of resistive and capacitive elements in the pit wall. The section with the higher slope at higher frequencies was due to double layer charging at the pit bottom. Alan and his group performed electrochemical impedance spectroscopy measurements on an interstate highway bridge I-beam that was coated with a surface-tolerant coating, applied at test patches. They studied the changes in the coating resistance and found that the coating was degrading even before a clear degradation was seen, which was concluded from the Nyquist and Bode plots

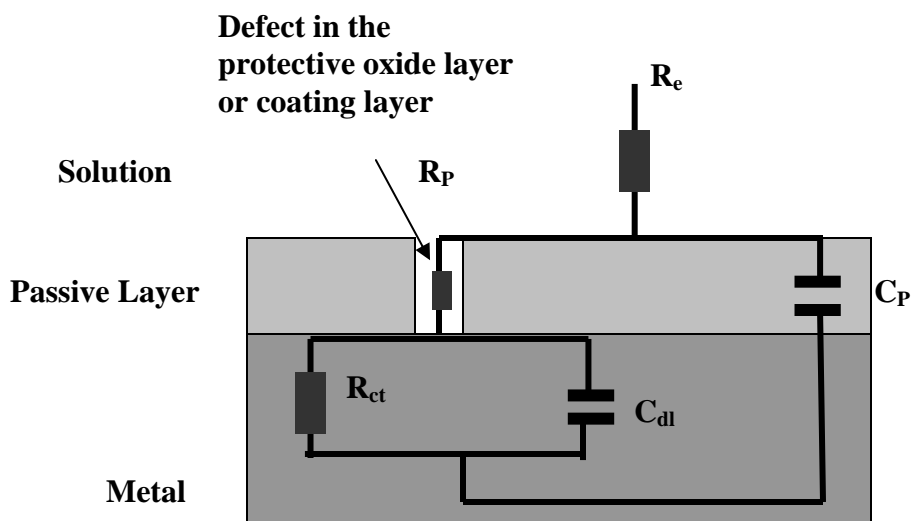


**Figure 6.1. Equivalent circuit representation for electrochemical processes taking place at metal surface and solution ( $R_e$  – resistance of electrolyte,  $R_p$  – polarization resistance,  $C_p$ - polarization capacitance,  $W$ -Warburg impedance,  $C_{dl}$  – double layer capacitance,  $R_{ct}$  – charge transfer resistance)**

obtained<sup>10</sup>. Pettersson and Pound performed AC impedance spectroscopy to study the effect of molybdenum in the passivation of stainless steel. Using the Nyquist plots, polarization curves and equivalent circuits, the group determined that molybdenum played a very important role in dissolution, formation of intermediate species and passivation of stainless steel<sup>11</sup>.

#### 6.1.1. Alloy 600 Vs alloy 690

In past it has been proposed to use alloy 690 instead of alloy 600 in constructing steam generator tubes and components to reduce pressurized water reactor stress corrosion cracking. Alloy 600 has 15% (max.) chromium content whereas alloy 690 has 30% chromium content. The high chromium content in alloy 690 makes it resistant to inter-granular corrosion and inter-granular stress corrosion cracking when compared to alloy 600<sup>12</sup>. Most nuclear power plants use



alloy 600 to build tubes in steam generator systems. But due to depletion of chromium and formation of carbide in the grain boundaries, alloy 600 is susceptible to stress corrosion cracking. So in recent past, alloy 690 has replaced alloy 600 in construction of tubes and other components in the pressurized water reactor systems<sup>13, 14</sup>.

Single mechanism cannot explain stress corrosion cracking at high temperatures in alloy 600. Rebak and Smialowska reviewed different mechanisms that lead to stress corrosion cracking in alloy 600 at high temperatures. At the end of their analysis, they proposed that processes controlled by diffusion leading to internal oxidation and slow growing defects can at least give a good estimate on the life of the tubes<sup>15</sup>. Montemor and group studied oxide films formed on alloy 600 and 690 in aqueous environments (pH 8 and 10) at high temperatures using Auger analysis and photo-electrochemical measurements. From their analysis, the group concluded that the alloy 690 shows a duplex nature. The duplex nature means the semi conducting properties of the alloy are controlled by iron-nickel oxide on the inner surface and by chromium oxide on the outer surface. On the other hand they also observed that nickel oxide controlled the semiconductor properties of alloy 600 at pH of 8 and mixed oxide consisting of iron-nickel at pH of 10<sup>16</sup>.

Lemire and McRae studied the thermodynamic stability of alloy 690 at 310°C in aqueous environment. Based on thermodynamic data, they concluded that Fe and Ni are stabilized and Cr is destabilized in alloy 690 compared to pure elements. They also ruled out formation of stable phase of  $\text{NiCr}_2\text{O}_4$  and  $\text{FeCr}_2\text{O}_4$  at 310°C. In contact with reducing aqueous solution at this temperature, Ni,  $\text{Fe}_3\text{O}_4$  and NiO are more soluble than  $\gamma\text{-CrOOH}$ , which forms a thin film on the surface. Under very oxidation conditions  $\gamma\text{-CrOOH}$  converts to Cr (IV) species and formation of NiO and  $\text{NiFe}_2\text{O}_4$ <sup>17</sup>.

The amines studied in this research are DBU, DMA, ETA and Morpholine. Inconel alloys 600 and 690 have been selected in this study because of their extensive use in steam generator tubing in pressurized water reactors. The purpose of this study was to understand the corrosion inhibition mechanism of the above mentioned amines on materials used in nuclear power plant. To fully understand the inhibition efficiency of the amines it is important to study their effect on inconel surface at steam generator temperatures and pressures. This study is an attempt to understand the mechanism of the amines at the inconel surface at high temperatures (300°C) and also to compare the inhibition efficiency of the newly proposed amine, DBU to the presently used amines, DMA, ETA and morpholine, by CPSES. Not many studies have been performed on DBU to study its corrosion inhibition mechanism. CPSES performed some initial studies by soaking low carbon steels in DBU solution at room temperature and at 150°C.

## 6.2. Experimental setup

### 6.2.1. Room Temperature studies<sup>3</sup>

The effect of 1, 8-diazabicyclo [5.4.0] undec-7-ene (DBU), dimethyl amine (DMA), ethanolamine (ETA) and morpholine on inconel 600 coupons were studied at room temperature. The experiments were carried out using AC-Impedance spectroscopy at frequency range of 100 kHz -5 Hz. Equivalent circuit representing frequency response of each amine in aqueous solution on Alloy 600 is presented. Purpose of this experiment was to compare metal behavior in the presence of different amines from mechanistic point of view i.e. film forming or neutralizing.

---

<sup>2</sup> The entire room temperature study has been reproduced with permission from NACE International, H. Namduri and Nasrazadani, NACE Conference-March 2006, San Diego, CA.

Inconel alloy 600 was used for studying the effect of amines on the metal surface (see Table 6.1 for alloy 600 chemical composition). AC-impedance spectroscopy technique was used to study the effect of the amines DBU, DMA, ETA and morpholine. A Model 2273 Advanced Electrochemical System, manufactured by EG&G Princeton Applied Research Corporation, was used for all the measurements. The system include: a) Model 2273 computer-controlled advanced potentiostat/galvanostat / frequency response analyzer; b) flat Cell with saturated calomel electrode (in saturated KCl) and platinum counter electrode; and c) Power Suite software. The AC-impedance data was gathered in the frequency range of 100 kHz to 5 kHz (Single sine; points/decade, 5; AC amplitude, 5mV; DC potential, 0V vs. OC (open circuit); condition time 0 seconds; condition potential, 0V vs. OC; The alloy samples were in the form of flat coupons. The flat cell was designed in such a way that the exposed metal surface area is  $1 \text{ cm}^2$ . The exposure time of the coupon to the amine solution was varied for 6 hrs, 12 hrs, 24 hrs and 48 hrs. The reason for varying the exposure time was to determine the behavior of the film formed on the metal surface a function of time. An optimized pH of 9.0 is established for steam generator materials to provide corrosion protection in water-cooled nuclear reactors. The electrolyte solution was prepared by adding amine to de-ionized water to maintain the pH at 9.0, which was constant for all the experiments. The data was in the form of Nyquist and Bode plots. Only Nyquist plots have been used in this study for the purpose of analysis.

#### 6.2.2. High Temperature studies

The present section deals with effect of amines (morpholine, DMA, ETA and DBU) on inconel alloys 600 and 690 at high temperature and pressure. Chemical composition of alloys 600 and 690 are given in Table 6.1. Electrochemical impedance and polarization curves have

been used to study the corrosion inhibition mechanism of the amines. Tests were performed in an autoclave at a temperature of 300°C and a pressure of 1000 psi. The morphology of the alloy surface was studied using scanning electron microscopy (SEM) and energy dispersive spectroscopy (EDS) to study the composition of the surface after the samples were treated with amine solution.

Electrochemical impedance spectroscopy (EIS) technique was used to obtain Nyquist plots to study the reaction mechanism taking place at the alloy surface. Both alloys 600 and 690 were soaked in amine solution at 300°C for 3 hrs in the autoclave made of hastelloy. Amine solution at constant pH of 9.0 was used for all the experiments. Amine was added to the distilled water to attain the required pH. An external, cold pressurized Ag/AgCl (0.22V) reference electrode was used to monitor the free corrosion potential and electrochemical impedance of alloys 600 and 690. The amine solution was the electrolyte and the alloy coupon (2.5 x 5.0 cm) was the working electrode. The samples were heated to 300°C and the pressure at this temperature was 1000 psi for 3 hrs. Impedance measurements were taken at 100°C, 200°C and 300°C (3 hrs after exposure at this temperature). Data was collected in the frequency range of 0.1 Hz to 10<sup>6</sup> Hz at AC amplitude of 5 mV/min. Polarization curves were obtained by varying the voltage from -0.225 V to 1.6 V at a scan rate of 1 °C mV/min. The curves were obtained at room temperature, 100°C, 200°C, and 3 hrs at 300°C.

**Table 6.1. Chemical composition of alloys 600 and 690**

	Ni (%)	Cr (%)	Fe (%)	Si (%)	C (%)	Mn(%)	S (%)	Cu (%)
Alloy 600	72	14-17	6-10	0.5 max.	0.15 max.	1.0 max.	0.015 max.	0.5 max.
Alloy 690	58	27-31	7-11	0.5 max.	0.05 max.	0.5 max.	0.015 max.	0.5 max.

## 6.3. Results and Discussion

### 6.3.1. Room Temperature studies

Inconel alloy 600 when exposed to DBU solution, the Nyquist plot showed a partial semicircle at higher frequency along with a semi-circle at medium frequency. Warburg impedance corresponding to diffusion processes taking place at metal surface was observed at low frequencies. From Figure 6.2 it is observed that the semi-circle at the medium frequency range disappears with the increase in the exposure time. The straight line corresponding to diffusion process and the partial semicircle remain constant with the change in the exposure time. The semi-circle corresponds to the formation of intermediate organic compounds at the metal surface. There are two nitrogens present in DBU. One nitrogen ( $N_2$ ) is attached to three carbon atoms ( $sp^3$  nitrogen) and the other nitrogen ( $N_1$ ) is doubly bonded to carbon ( $sp^2$  nitrogen) which in turn is bonded to  $N_2$ -nitrogen. Rao and et al showed that the  $N_1$ - nitrogen in DBU can act as the site of donation and get deshielded in protonating solvent<sup>18</sup>. Further analysis using NMR and XPS can give more information on the type of compound formed on the metal surface. The organic compound in this case is the intermediate compound of amine in the solution. The partial semi-circle is due to the charge transfer process taking place between the ions in the solution and the metal surface. The interface between the solution and the metal surface is modeled as double layer capacitance and is kinetically parallel with charge transfer reaction. Figure 6.3 indicates the equivalent circuit for the Nyquist plot shown in the Figure 6.2.

When inconel alloy 600 coupon was exposed to DMA solution, the Nyquist plot showed a partial semicircle that changes shape at lower frequencies. Even though polarization resistance ( $R_p$ ) and capacitance ( $C_p$ ) values have not been calculated in this study, but the partial semi-circle could still be used to determine  $R_p$  values of these plots. The general procedure to calculate is to

curve fit the partial semicircle which would give the intersection of the semicircle with the real axis <sup>6</sup>.  $R_p$  values in DMA exposed samples at different exposure times shows an increase with time (Figure 6.4). As observed from Figure 6.4, one can see a partial semicircle with a feature at the end in the form of a straight line with a positive slope. This straight line at the low frequency is probably due to diffusion process that could be associated to Warburg impedance.

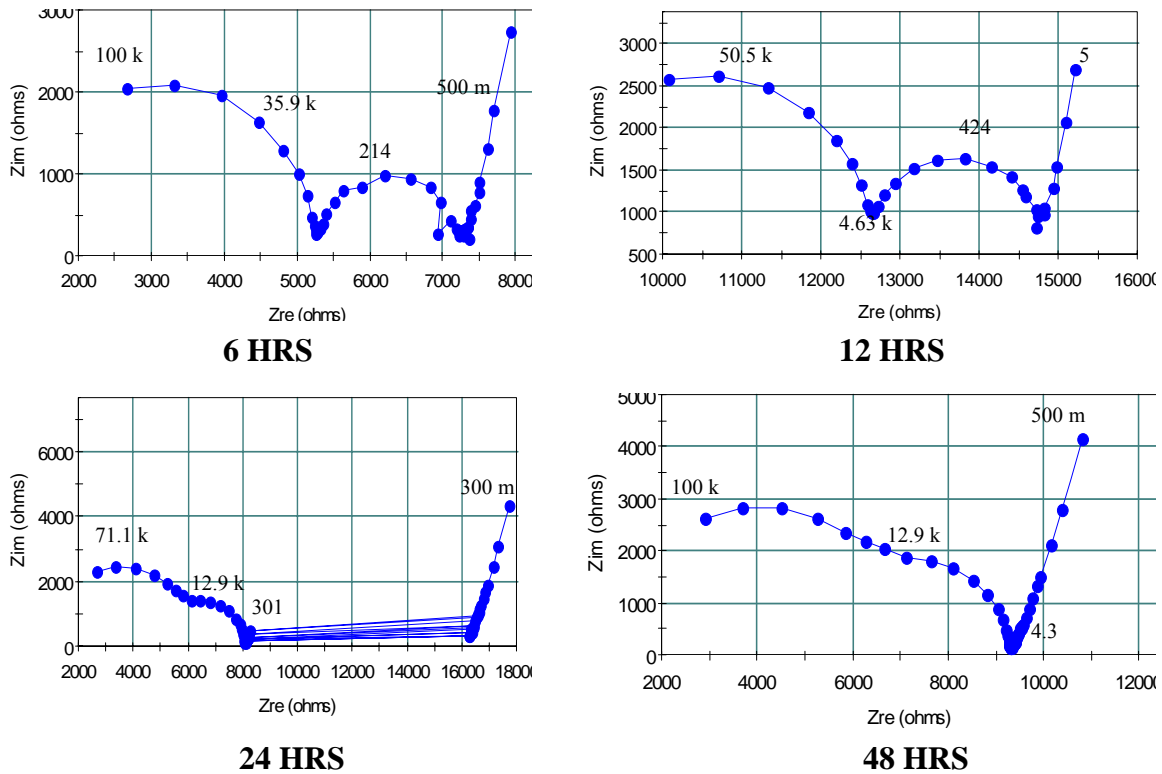


**Figure 6.2. Nyquist plots of Inconel 600 alloy exposed to DBU solution for 6, 12, 24 and 48 hrs**

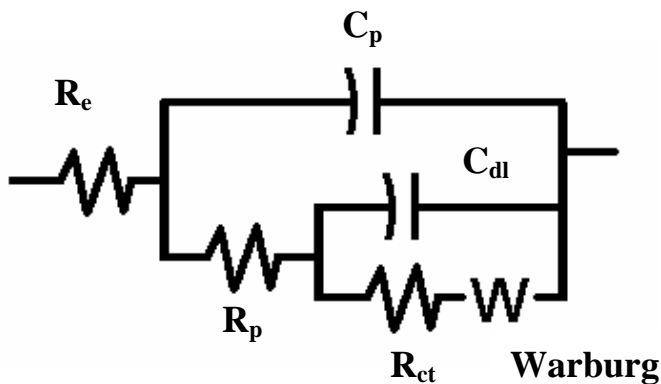


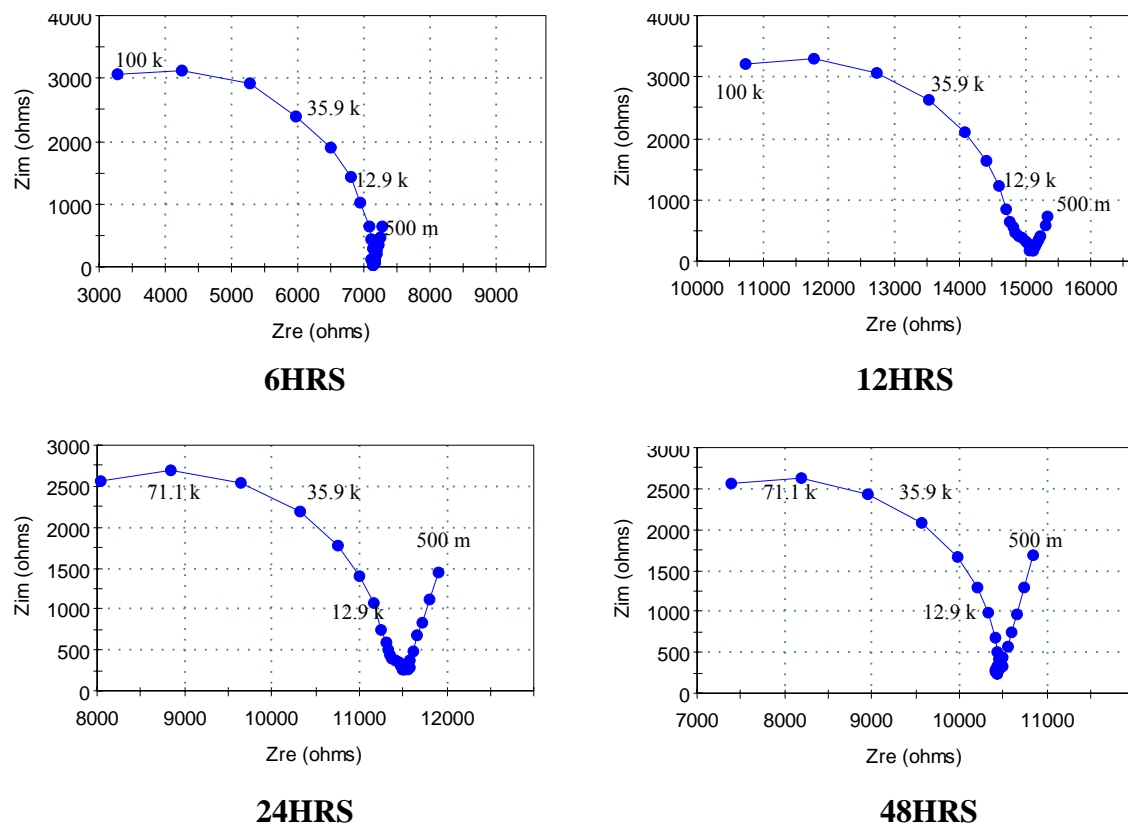
**Figure 6.3. Equivalent circuit for the Nyquist Plot shown in DBU Solution ( $R_e$  – resistance of electrolyte,  $R_p$  – polarization resistance,  $C_p$  – polarization capacitance,  $W$  – Warburg impedance,  $C_{dl}$  – double layer capacitance,  $R_{ct}$  – charge transfer resistance)**

It is also observed that the slope changes with the change in the exposure time, indicating that the diffusion process is changing for different exposure times. The rate at which an electrochemical reaction occurs is affected by diffusion process. The diffusion could occur when the metal is covered by reaction products or the reaction products are absorbed on to the metal surface.

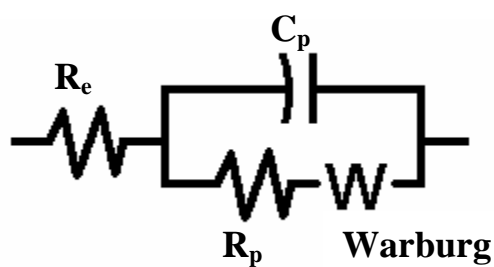
The electrochemical process which is diffusion-controlled has an impedance value, which is the Warburg impedance. At high frequencies one cannot expect to see this kind of impedance because the time is too short for diffusion process to occur<sup>19</sup>. The equivalent circuit for the Nyquist plot (Figure 6.4) is shown in Figure 6.5.

Figure 6.6 shows the AC-impedance spectrum of Inconel alloy 600 coupons exposed to ETA solution for 6, 12, 24, and 48 hrs. Capacitive and inductive loops were seen at low frequency ranges. As the time of exposure increased, the size of the inductive loop gradually decreased. Literature search shows that the inductive loop at lower frequencies is associated with relaxation of coverage of intermediates on the metal surface. The reduction in the inductive loop could be due to desorption process of amine or an intermediate of the amine present in the solution. In the present research, it is possible that the ETA molecules may have reacted with the metal surface and formed a protective film and as the time of exposure increased, the molecules could have desorbed from the metal surface.

The equivalent circuit for the Nyquist plot shown in the Figure 6.6 is given in the Figure 6.7. The inductive loop is typically modeled using the negative values of resistance and capacitance values which are the result of adsorption phenomena<sup>20</sup>. The polarization resistance,  $R_p = R_{ct} + R_{ad}$ , where  $R_{ct}$  is the charge transfer resistance and  $R_{ad}$  is the negative resistance due to adsorption.



**Figure 6.4. Nyquist plots of Inconel 600 alloy exposed to DMA solution for 6, 12, 24 and 48 hrs**



**Figure 6.5. Equivalent circuit for the Nyquist Plot shown in DMA Solution ( $R_e$  – resistance of electrolyte,  $R_p$  – polarization resistance,  $C_p$ - polarization capacitance,  $W$ -Warburg impedance)**



J. Manjanna<sup>21</sup> and his group studied the effect of ETA on Monel, Inconel 800 and stainless steel. They concluded that when the steel coupons were exposed to ETA solution at room temperature and at 150°C, a thin film formed on the surface of the metal, and they also observed adsorption of amine molecule on the metal surface in the form of a precipitate. They suggested that this adsorption could be due to formation of a complex between the amine molecule and the metal surface. They suggested that the formation of complex could have led to less protective film and thereby destabilizing the oxide film. J. S. Baek<sup>22</sup> and his colleagues observed a similar behavior of Alloy 600 exposed to NaOH containing solution and concluded that the impedance locus that bent over the negative real axis in the low frequency range was due to active- passive transition behavior. This active- passive transition phenomenon, they suggested was attributed to the formation of a corrosion film on the surface of the metal. They further indicated that the loop having negative resistance in the low frequency range may possibly have originated from relaxations due to film formation.

Inconel alloy 600 when exposed to morpholine solution showed a formation of a small semicircle at low frequencies and a partial semicircle at higher frequencies (Figure 6.8). This could be related to increase in the corrosion activity at the metal surface exposed to the solution. This small arc on the low frequency side could probably be due to the diffusion process and the arc on the high frequency represents kinetic impedance<sup>23, 24</sup>. As the exposure time increased, not much of a change was observed in the shape of the diffusion arc<sup>25</sup>. Figure 6.9 shows the equivalent circuit for the Nyquist plot in Figure 6.8.

DMA, ETA, and morpholine belong to the family of neutralizing amines, i.e. they prevent corrosion by controlling pH value of the electrolyte. These amines are most commonly

used in pressurized water reactors. The passivation capacity of the amines is due to the hydroxyl ions.

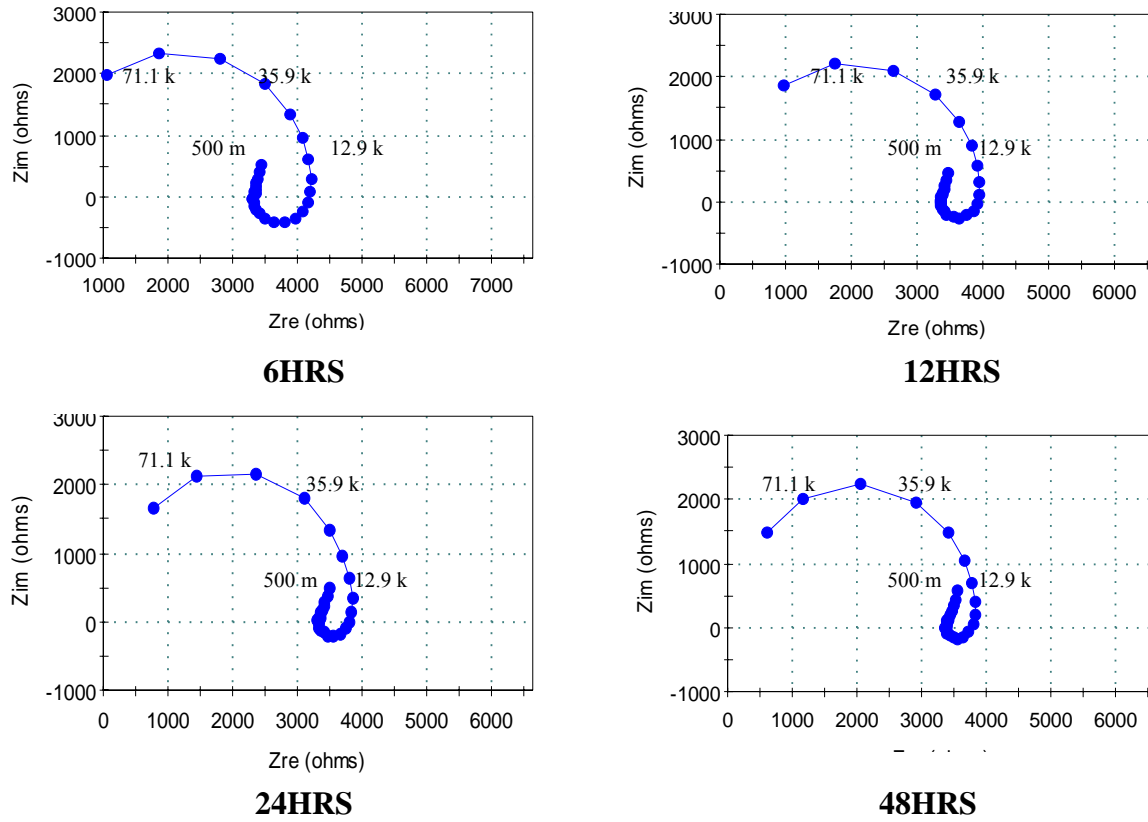


Figure 6.6. Nyquist plots of Inconel 600 alloy exposed to ETA solution for 6, 12, 24 and 48 hrs

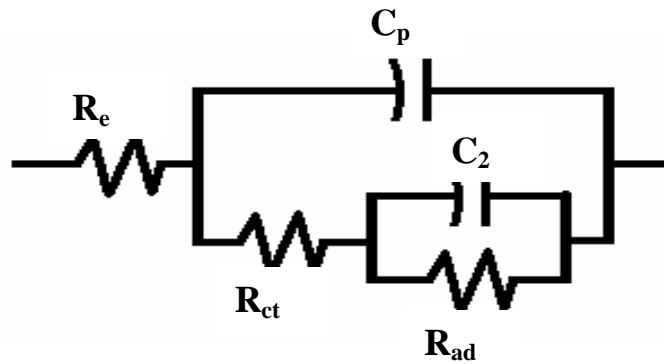


Figure 6.7. Equivalent circuit for the impedance response in the ETA solution ( $R_e$  – resistance of electrolyte,  $R_{ct}$  – charge transfer resistance,  $R_{ad}$ ,  $C_2$  – resistance and capacitance due to adsorption)

Amines hydrolyze as  $\text{RNH}_2 + \text{H}_2\text{O} = [\text{RNH}_3]^+ + \text{OH}^-$ , resulting in alkaline pH range<sup>21</sup>.

Klimas and his group suggested that ETA (less volatile), when compared to DMA and Morpholine, was more effective in neutralizing acidic crevices<sup>26</sup>. Consolidation is the main phenomena in the corrosion inhibition process using amines.

Consolidation is a process where the organic particles chemically bond to the previous deposit or to the bare metal surface. The driving force for this process to occur is the precipitation of smaller particles onto already formed deposit<sup>27</sup>. It is also known that affinity of iron for nitrogen is low, and amines used in this study are nitrogen based organic compounds. So the adsorption behavior on the iron oxide surface is not sensitive to the chemical structure of the adsorbing molecule, but studies in the past have shown that the corrosion inhibitors adsorb on iron in active states. So the adsorption could be due to different nature of the surface or surface chemical effects of the oxidized metal surface<sup>28</sup>. Overall mechanism of the corrosion inhibition of these amines on metal surfaces is related to chemical and physical structure of the amines, and their neutralizing capacity.

### 6.3.2. High Temperature studies

#### 6.3.2.1. Effect of Amines on Inconel Alloy 600

Electrochemical Impedance Spectroscopy: Nyquist plots obtained from high temperature studies of alloy 600 exposed to amine solution is discussed as follows:

a) Morpholine: Figure 6.10. demonstrates impedance spectra in Nyquist presentation obtained from alloy 600 at temperatures 100, 200, and 300°C (for 3 hrs at this temperature only). At

100°C the nyquist plot shows apparent Warburg impedance, indicating that the diffusion process contributes to the total charge transfer rate.

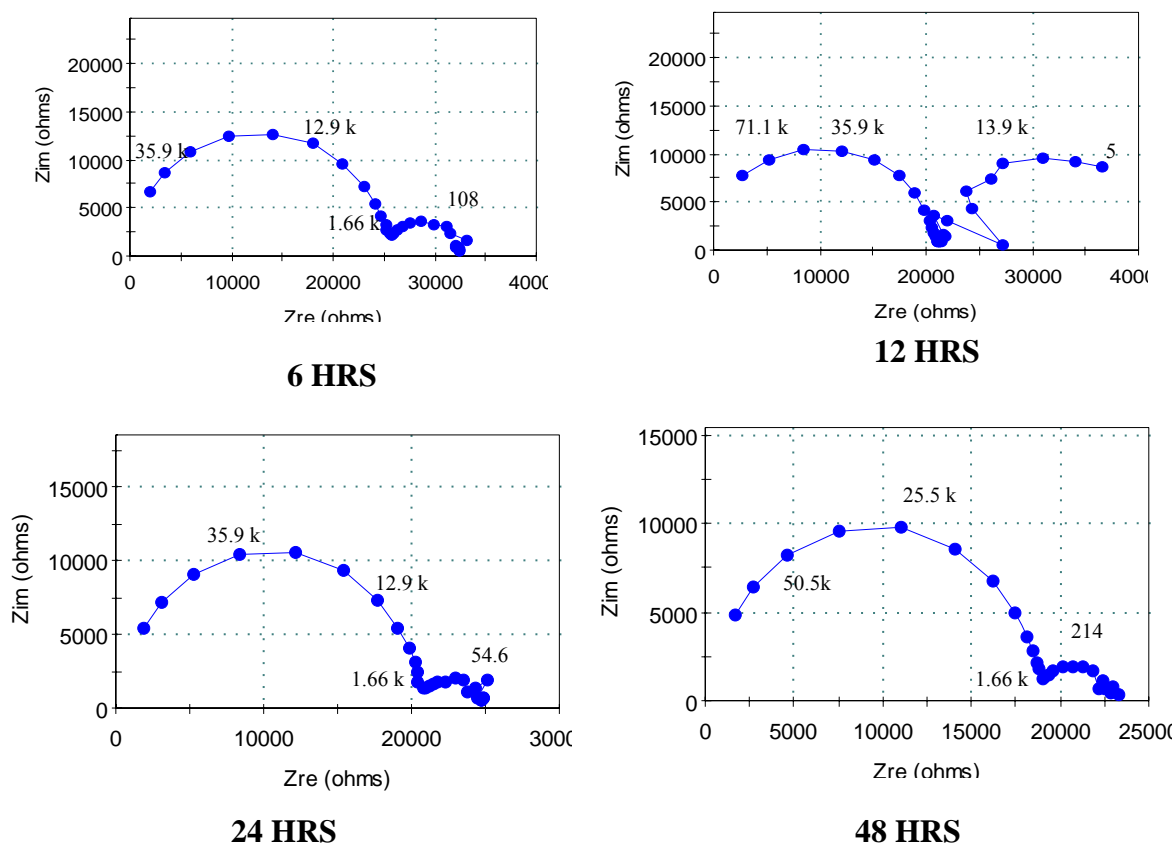


**Figure 6.8. Nyquist plot of Inconel 600 alloy exposed to morpholine solution for 6, 12, 24 and 48 hrs**

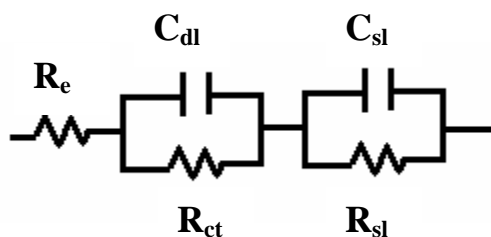


**Figure 6.9. Equivalent circuit for the impedance response in the morpholine solution ( $R_e$  – resistance of electrolyte,  $R_{ct}$  – charge transfer resistance,  $C_{dl}$  – capacitance of the diffusion layer,  $R_{sl}$ ,  $C_{sl}$  –resistance and capacitance of the surface layer)**

Warburg impedance is indicated by a straight line at 45 degrees on the complex plane. At 200°C, there is still a trace of diffusion process along with the presence of capacitive semicircle. This semicircle indicates that the charge transfer rate is more due to the supporting electrolyte. At 300°C Warburg diffusion disappears resulting in increase of capacitive semicircle at low frequency range. This could be the indication of corrosion process taking place at the metal surface and initial formation of passive film on the surface<sup>29</sup>.

b) Ethanolamine (ETA): Figure 6.11 shows Nyquist plot of alloy 600 sample exposed to ETA solution at 100°C. At this temperature the plot shows a capacitive behavior. The plot consists of a depressed semi-circle at high frequency, which could be attributed to charge transfer process. The centre of this semi-circle lies below the real axis, probably due to frequency dispersion of impedance data. Along with the semi-circle, a capacitive loop is also seen at medium frequencies which resemble an inductive loop over the real axis, and a capacitive loop drawing a straight line or a portion of second semi-circle at low frequencies. This line is the Warburg impedance that may be due to the diffusion process taking place at the metal surface. The capacitive loop is due to the adsorption-desorption processes taking place of the passive film at the metal surface<sup>30, 31</sup>. As the temperature is increased to 200°C, there is a break in the capacitive loop giving rise to inductance loop at high temperatures. At 300°C, the partial semi-circle below the real axis is associated with an inductance effect. Similar behavior was found by Hodges and his group while studying the electrochemical nature of stainless steels in high and low conductivity solutions<sup>32</sup>. This negative resistance and capacitance contribute to the total impedance. The pseudo-inductive loop indicates a desorption process of some intermediate amine compound present in the test solution from the metallic surface<sup>33</sup>.

c) Dimethylamine (DMA): Figure 6.12 Nyquist plots consisted of a capacitive loop followed by a second capacitive loop which bends towards positive or negative part of real axis. As the temperature was increased the second capacitive loop was replaced by inductive loop. The first capacitive loop at the low frequency is related to rate of charge transfer reaction at metal-oxide interface and corresponding changes in the film thickness is indicated from the second loop. This in result is related to connection between the double layer and the charge transfer resistance<sup>34, 35</sup>.

d) DBU: At 100°C, alloy 600 coupon exposed to DBU solution shows an inductance loop at high frequency range. This could be due to desorption process where the bare metal is exposed due to damage in the passive film formed by chromium and nickel. As the temperature is increased to 200°C, a complex pattern is observed. The corresponding Nyquist plot shows a large number of time constants. A high frequency capacitive behavior along with inductance behavior at medium frequencies is observed. In addition a capacitance behavior is also observed at lower frequencies. The inductive loop at medium frequencies is indicative of relaxation of the negative surface charge formed by the accumulation of metal vacancies at the film/solution interface. For example the relaxation could be due to some intermediates in the transpassive dissolution reaction of Chromium. The dissolution of chromium from the outermost layers of the anodic film can lead to decrease in the film resistance<sup>36</sup>. This plot may be indicative of active-passive transition region.<sup>37</sup>

At 300°C, Nyquist plot consists of inductive region and small capacitance semicircle at high frequencies, one large capacitive semicircle at medium frequencies and Warburg linear region at low frequencies. The formation of partial semicircle at medium frequency is indicative of charge process in electrode/electrolyte interface. These would relate to the changes in the passive film property and chemical composition<sup>38</sup>. The inductive loop is indicative of relaxation of adsorbed species<sup>39</sup>.

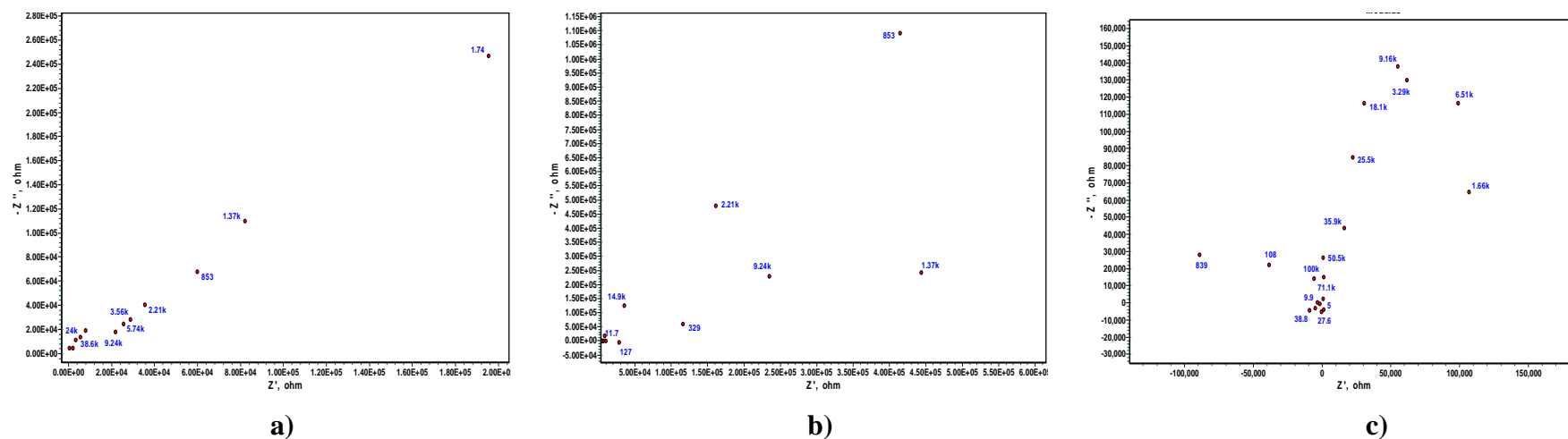


**Figure 6.10. Nyquist plots of alloy 600 in morpholine solution at a) 100°C, b) 200°C, and c) 3 hrs at 300°C**

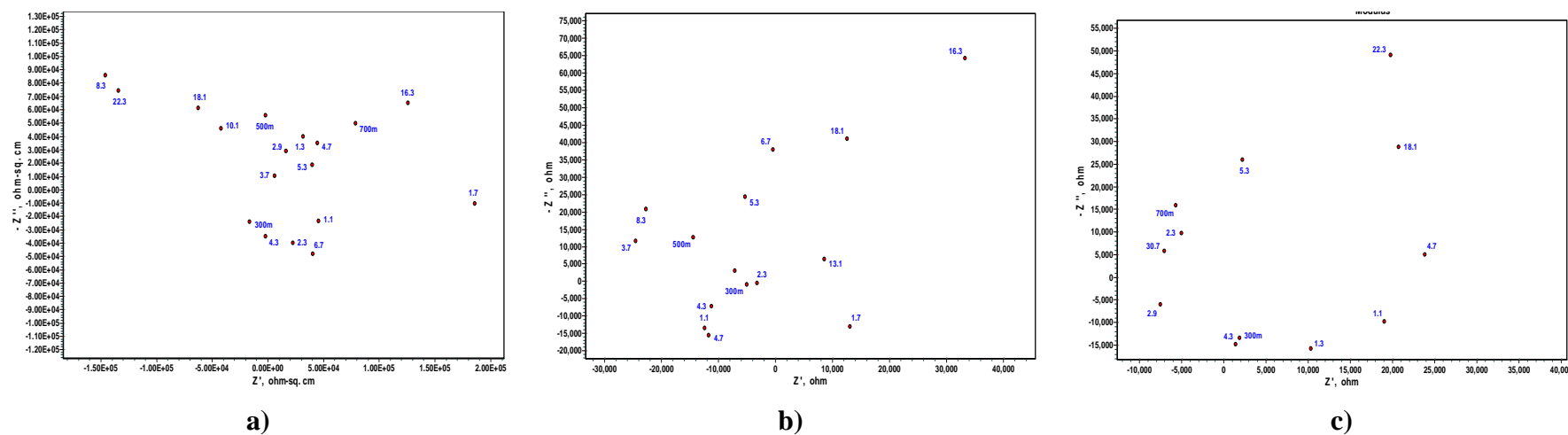


**Figure 6.11. Nyquist plots of alloy 600 in ETA solution at a) 100°C, b) 200°C, and c) 3 hrs at 300°C**

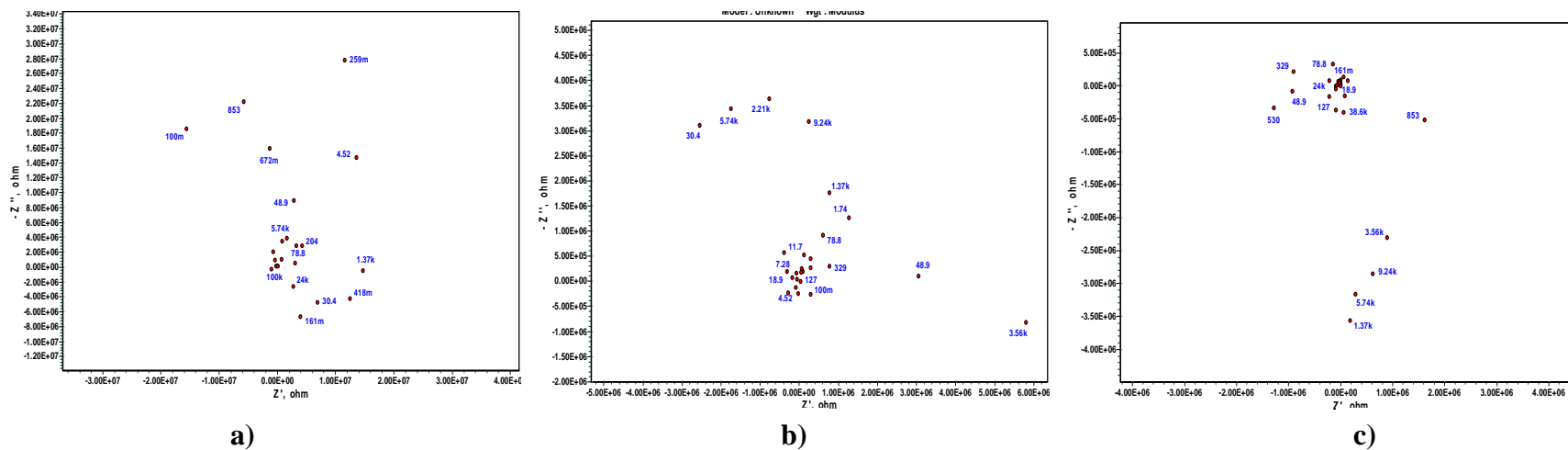


**Figure 6.12. Nyquist plots of alloy 600 in DMA solution at a) 100°C, b) 200°C, and c) 3 hrs at 300°C**

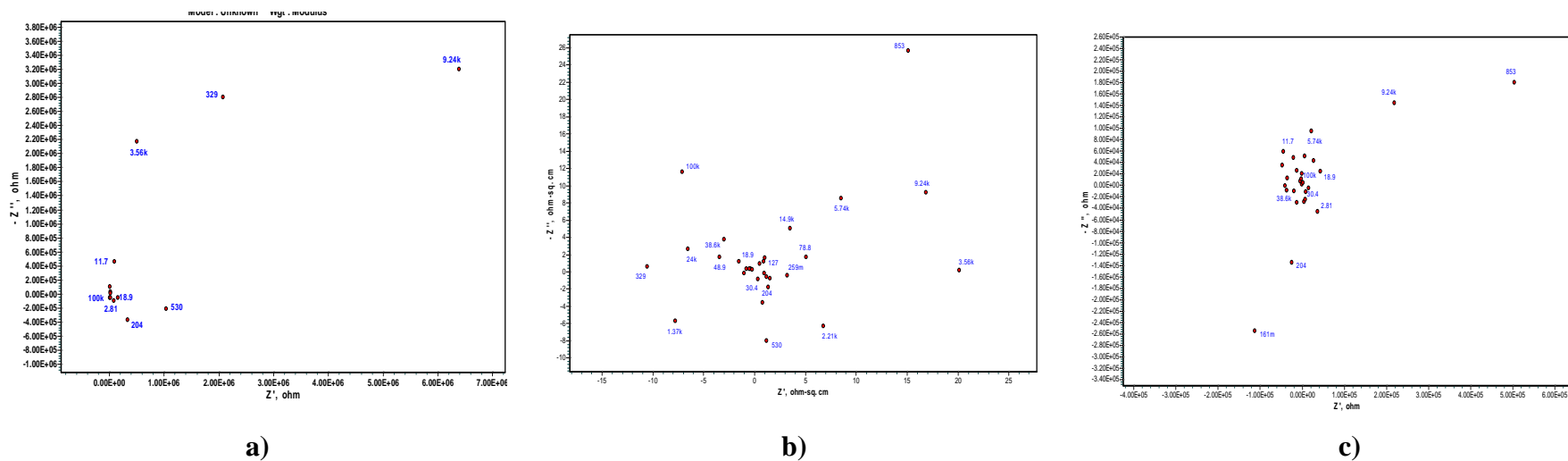


**Figure 6.13. Nyquist plots of alloy 600 in DBU solution at a) 100°C, b) 200°C, and c) 3 hrs at 300°C**



Polarization Resistance: Polarization curves were obtained for the alloy 600 coupons exposed to different amines. The linear portion of the polarization curves was used to determined polarization resistance. Polarization resistance is the slope of this linear portion. The polarization resistance for inconel alloy 600 exposed to different amines is shown in Figure 6.14.

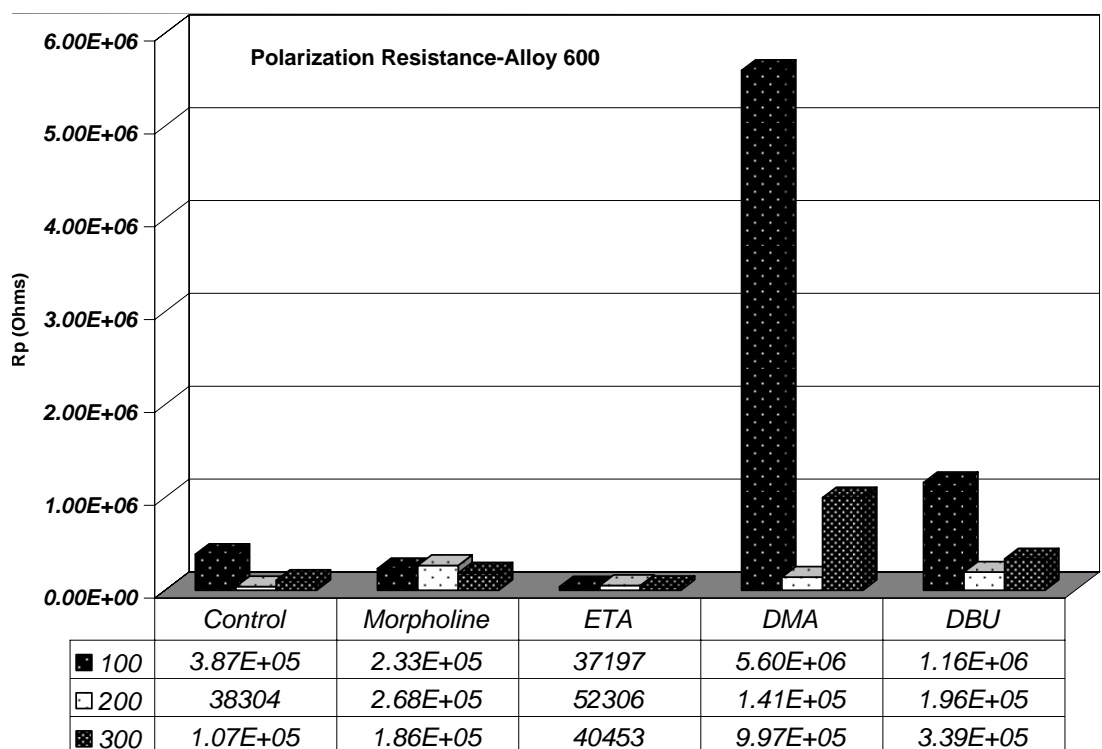


**Figure 6.14. Polarization resistance of alloy 600 for different amines**

DMA showed highest polarization resistance at 100°C and 300°C compared to the other amines. Morpholine showed highest polarization at 200°C. Polarization resistance is inversely proportional to corrosion rate. In general after exposure for 3 hrs at 300°C, the corrosion resistance of alloys can be shown as: ETA<Control (NaOH) <morpholine<DBU < DMA.

SEM-EDS Analysis: Morphology and elemental concentration obtained using SEM-EDS is discussed below. The SEM image is shown in Figure 6.15. The chart in Figure 6.16 shows the distribution of different elements in the alloy 600 samples exposed to different amine solutions.

Untreated: Figure 6.15a and b shows the SEM image of untreated and control samples of alloy 600. As expected, this sample shows the presence of Ni, Cr, Si, Fe, C and Mn. Ni and Cr.

Morpholine: Alloy 600 coupons exposed to morpholine solution at 300°C for 3 hrs at pH 9.0 shows formation of a very porous oxide layer on the metal surface (Figure 6.15 b). EDS spectra shows the major elements like Ni and Cr. It is also observed that there is an increase in the intensity of oxygen in morpholine compared to the untreated sample. This clearly indicates the formation of oxide layers of Cr, Ni, and Fe.

ETA: Figure 6.15 d and e show SEM images and EDS spectra of alloy 600 samples exposed to ETA solution. It was observed that there is a large increase in the intensity of Si and oxygen in the EDS spectra (Figure 6.17). This could be due to formation of  $\text{Ni}_2\text{SiO}_4$  due to pegging effect of internally oxidized silicon at the metal-oxide interface. Initially an external scale is formed consisting of NiO,  $\text{SiO}_2$  with  $\text{Cr}_2\text{O}_3$  precipitates at grain boundaries. This lowers the oxidation potential, promoting the lateral growth of  $\text{Cr}_2\text{O}_3$  scale. So at intermediate stages stable binary oxides convert to ternary oxides like  $\text{Ni}_2\text{SiO}_4$ . This formation of complex ternary silicon oxide is effective in limiting ionic transport<sup>40</sup>. Indication of sulfur in the EDS spectra could be due to the reaction between Ni and S. Sulfur reacts with Ni and coalesces as small nickel sulfide islands which may be covered by lateral growth of chromium oxide islands<sup>41</sup>. Formation of sulfur is known to interfere with the formation of passive layer of nickel and is also known to accelerate stress corrosion cracking<sup>42</sup>.

DMA: The samples exposed to DMA solution (Figure 6.15e) shows the breakdown of protective layer of chromium oxide. The high concentration of silicon peak indicates that the layer under the failed chromium oxide is silicon dioxide. DMA shows highest concentration of silicon compared to other samples (Figure 6.16).

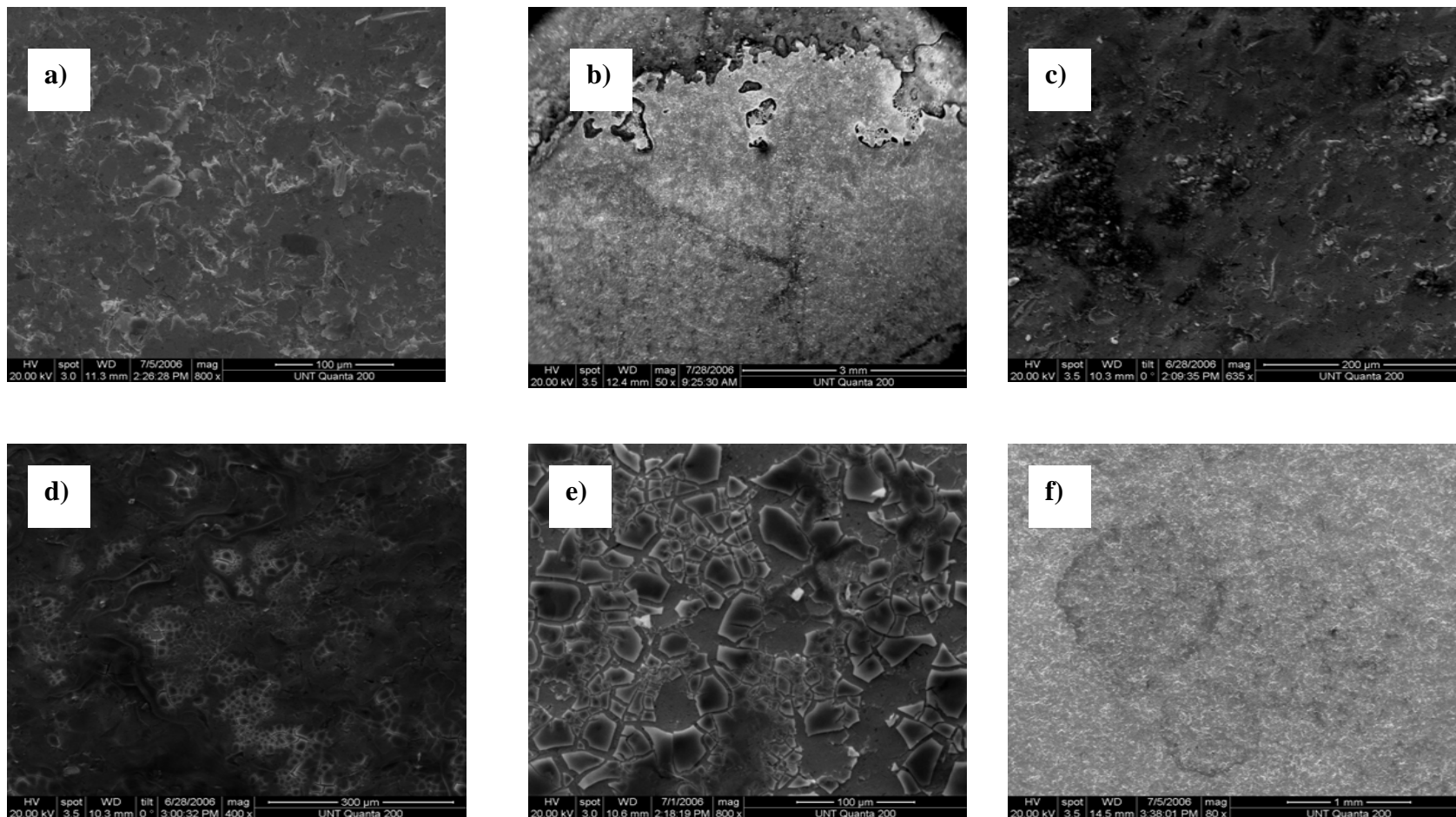


**Figure 6.15. SEM photographs of Inconel alloy 600 samples exposed to a) untreated, b) control (NaOH) , c) morpholine, d) ETA, e) DMA, and f) DBU for 3 hrs at 300°C in autoclave at pH = 9.0**

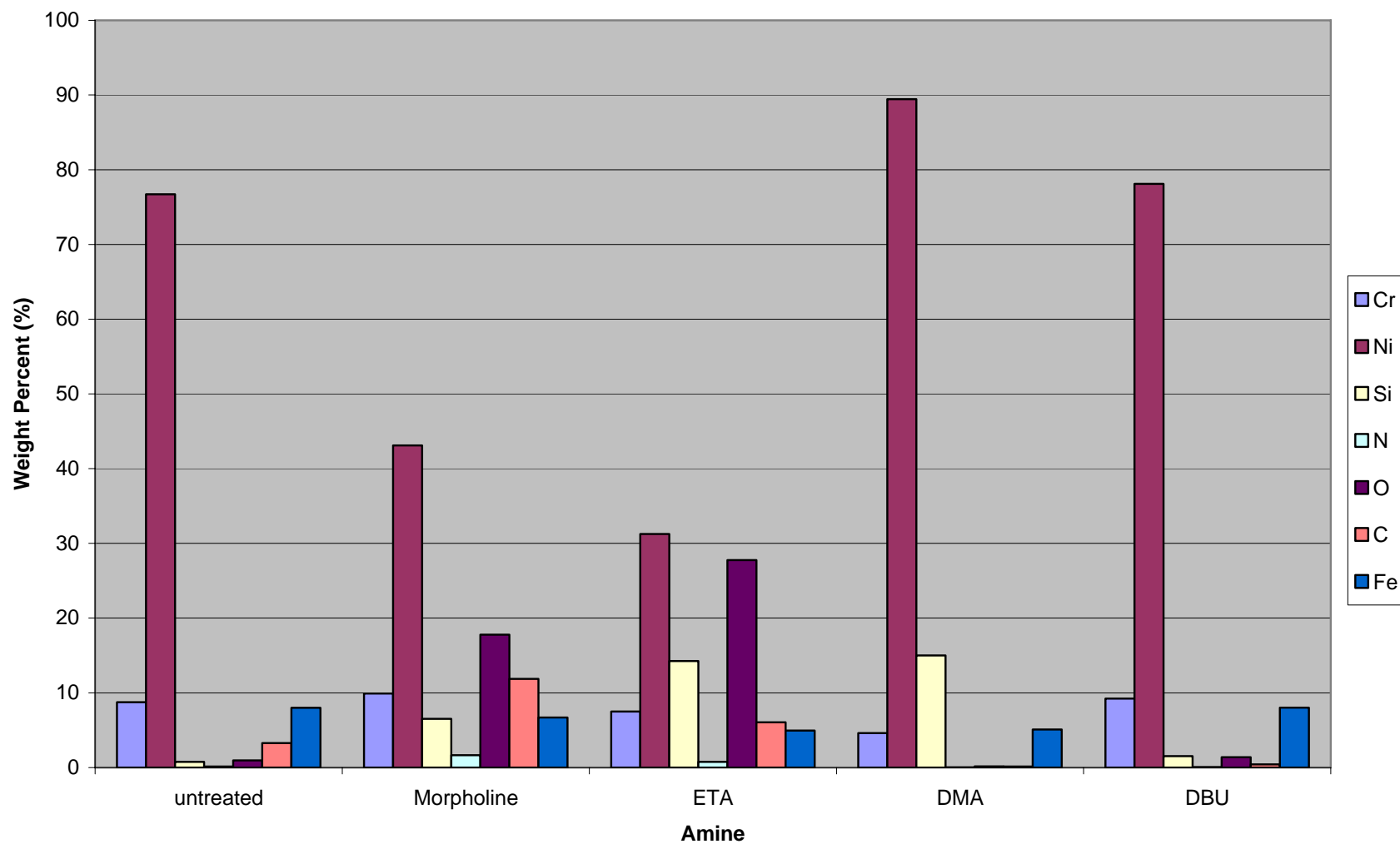


**Figure 6.16. EDS elemental concentration of Inconel 600 samples treated with untreated, morpholine, ETA, DMA, and DBU at 300°C for 3 hrs and pH = 9.0**

Literature review shows that silicon may play an important role in reducing the rate of diffusion of chromium in high alloyed steels and can improve high temperature oxidation resistance<sup>43, 44</sup>. During heating of doped steels, silicon segregates at the outer surface and forms a thin silicon dioxide film.

DBU: Unlike ETA and DMA, samples exposed to DBU do not show any pronounced increase in the concentration of silicon. The SEM images (Figure 6.15f) show a protective layer of chromium oxide on the surface.

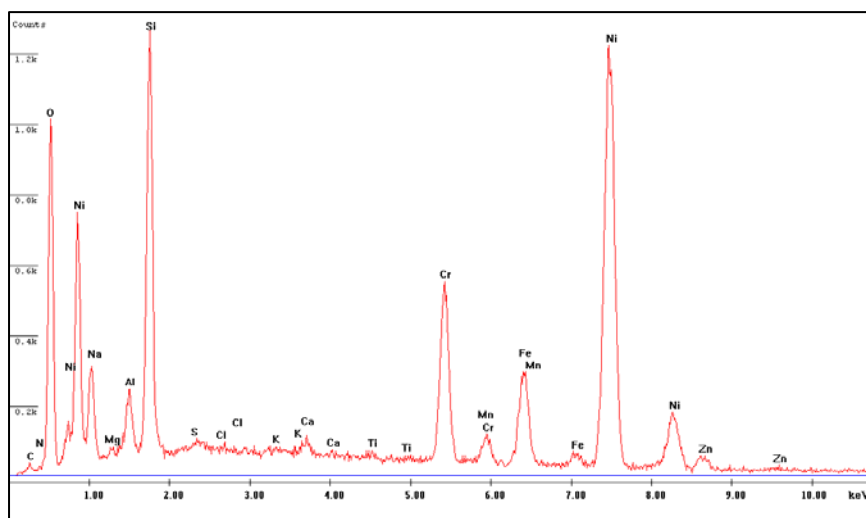


**Figure 6.17. EDS spectra of alloy 600 samples exposed to ETA at 300°C for 3 hrs and pH = 9.0**

#### 6.3.2.2. Inconel Alloy 690

Electrochemical Impedance Spectroscopy: Nyquist plots obtained from high temperature studies of alloy 690 exposed to amine solution (Figures 6.18-6.21) is discussed as follows:

a) Morpholine: At 100°C, the shape of the Nyquist plot shows the relaxation of the charge carriers density in the passive film formed on the metal surface. The loop at low frequency indicates this relaxation process. At 200°C an inductive loop is observed probably due to the

desorption of the passive film. But as the temperature was increased, the inductive loop transforms into capacitive loop due to increase in the anodic potential<sup>45</sup>. As the temperature was increased to 300°C, the low frequency loop changed to high frequency range. A linear Warburg element is observed in the low frequency region indicating the diffusion process between the ions in the solution and the metal surface.

b) ETA: Figure 6.19 shows the Nyquist plots of alloy 690 samples exposed to ETA solution at 100, 200 and 3 hrs at 300°C. Only one semi-circle is present at 100°C temperature at low frequency range. A medium frequency range time constant is observed at 200°C. Presence of two semi-circles may be due to formation of corrosion resistive Ni and Cr film on the metal surface against further diffusion of ion/amine solution. The first loop may be due to the formation of outer layer and the second loop may be due to formation of the inner layer. After heating for 3 hours at 300°C in the autoclave, a time constant is observed at high frequency range. This may be due to capacitive behavior of the oxide film formed on the metal surface<sup>46</sup>. This complex plane diagram shows the nickel in passive region<sup>47</sup>. As the temperature was increased the size of the first loop increased and the second loop decreased. So as the solution temperature is increased, there is a growth in the outer layer and impediment in the growth of inner layer<sup>48</sup>.

c) DMA: At 100°C (Figure 6.20), a large capacitance loop is observed at low frequency range. This has been tentatively related to diffusion process<sup>49</sup>. At 200°C, a high frequency capacitive arc, inductive arc and a low frequency capacitive arc are observed. The third arc is associated with passivation reaction. A high frequency capacitive semi-circle along with Warburg impedance is observed at 300°C. The semicircle indicates the charge transfer resistance of the solution.

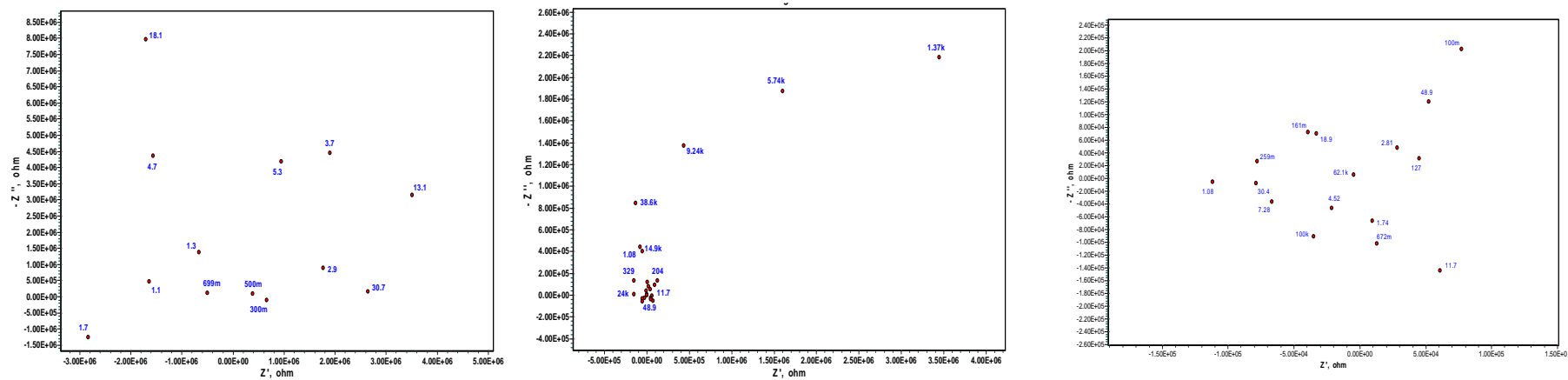


**Figure 6.18. Nyquist plots of alloy 690 in morpholine solution at a) 100°C, b) 200°C, and c) 3 hrs at 300°C**

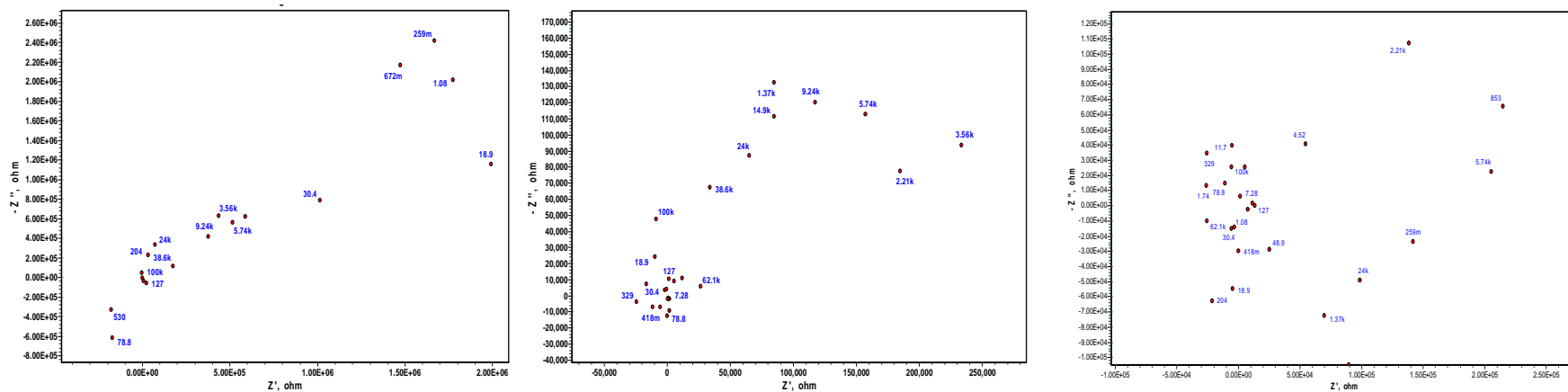


**Figure 6.19. Nyquist plots of alloy 690 in ETA solution at a) 100°C, b) 200°C, and c) 3 hrs at 300°C**

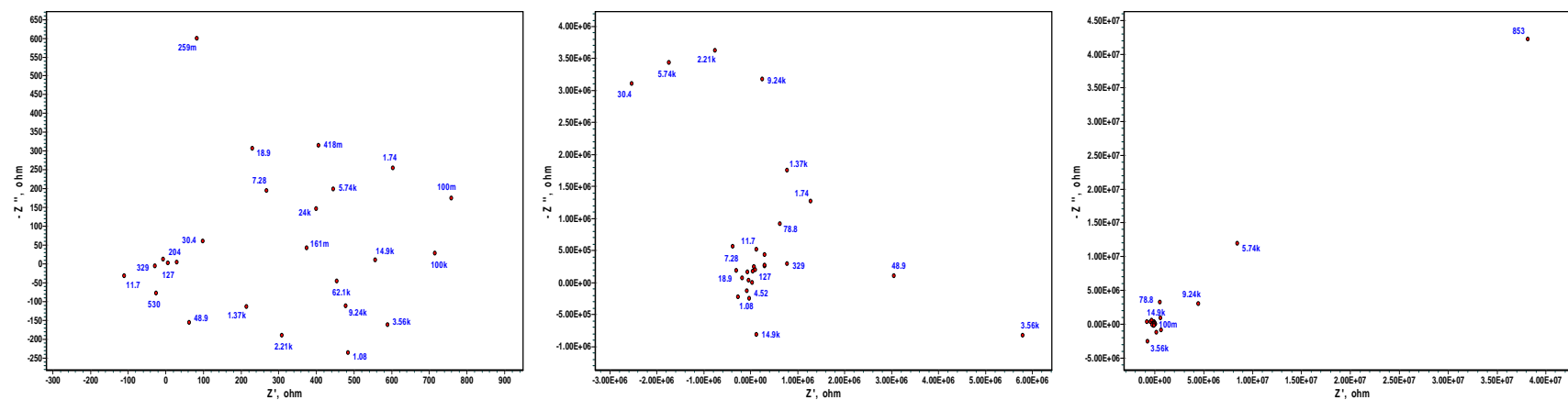


**Figure 6.20. Nyquist plots of alloy 690 in DMA solution at a) 100°C, b) 200°C, and c) 3 hrs at 300°C**

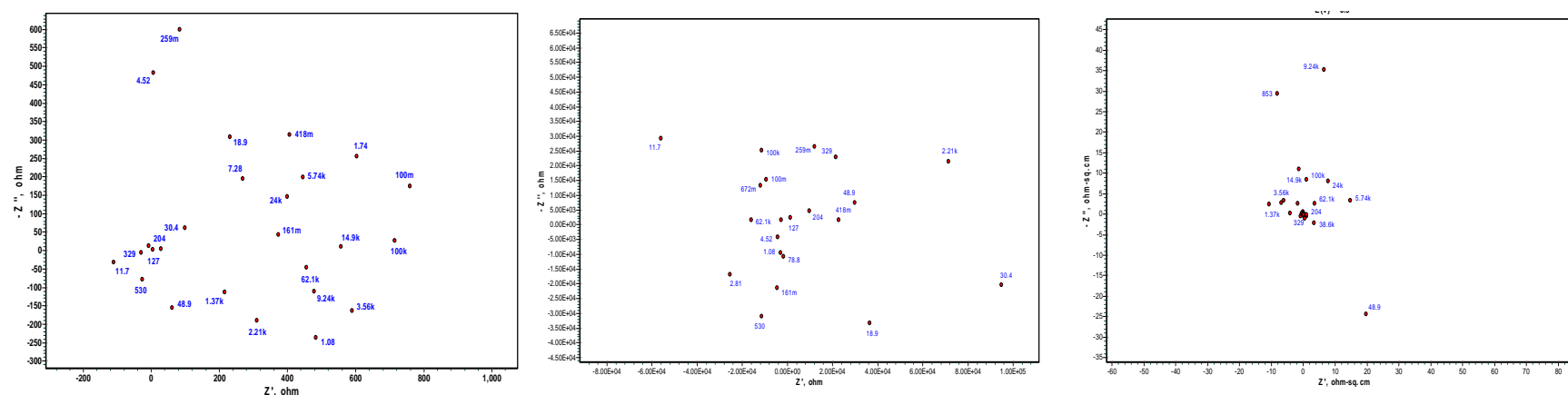


**Figure 6.21. Nyquist plots of alloy 690 in DBU solution at a) 100°C, b) 200°C, and c) 3 hrs at 300°C**



d) DBU: A large capacitance loop similar to sample exposed to DMA, is observed at 100°C. At 200°C a distorted semicircle is seen in the complex plane at low frequencies and having a negative intercept on the real axis at zero frequency. This may be due to adsorption of an intermediate species in passivation reaction or adsorbed molecule of inhibitor on the metal surface. At 300°C, consists of inductive region and small capacitance semicircle at high frequencies, one large capacitive semicircle at medium frequencies and Warburg linear region at low frequencies. The formation of partial semicircle at medium frequency is indicative of charge process in electrode/electrolyte interface. These would relate to the changes in the passive film property and chemical composition. The inductive loop is indicative of relaxation of adsorbed species.

Polarization Curves: Similar to alloy 600, polarization resistance was determined for alloy 600 (Figure 6.22.). DMA and DBU showed very low polarization resistance compared to morpholine and ETA. Morpholine showed the highest corrosion resistance compared to the other amines.

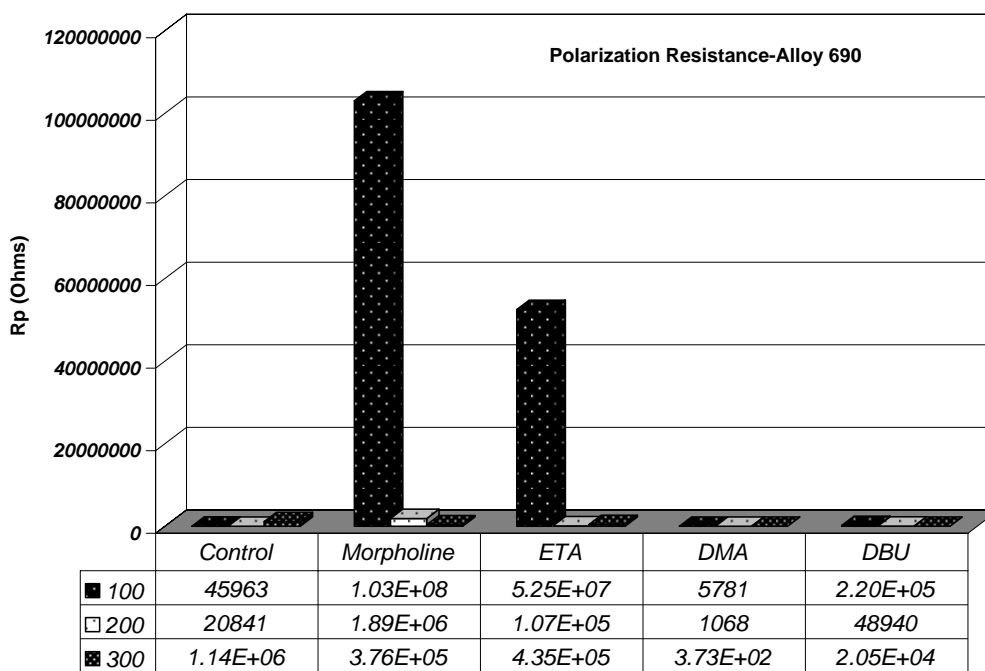


**Figure 6.22. Polarization resistance of alloy 690 for different amines**

SEM-EDS Analysis: Morphology and elemental concentration obtained using SEM (Figure 6.23.)

is discussed as follows:

Untreated: Figure 6.23a and b show the SEM image of untreated sample and control samples of alloy 690. Sample exposed to NaOH solution did not show any extensive signs of corrosion. As expected, the EDS spectrum of the untreated sample (not shown) of alloy 690 compared to alloy 600, the intensity of chromium peak was observed to be higher for alloy 690 when compared to alloy 600. It was also observed that the Ni peak intensity is lower than alloy 600.

Morpholine: Figure 6.23c clearly shows the formation of passive layer of chromium when exposed to Morpholine solution at 300°C at pH 9.0. EDS spectra (not shown) also showed a pronounced increase in the silicon concentration. The image shows a passive layer of chromium with patches of silicon dioxide underneath the chromium layer. The silicon dioxide layer interferes with the diffusion of ionic species and improves the corrosion resistance of the alloy at high temperatures.

ETA: The samples exposed to ETA solution overall show a widely covered protective film of chromium (Figure 6.23d). Some spots show areas where chromium layer was damaged either due to micro cracks, stress concentration etc. This breakdown of the oxide is soon protected by formation of silicon dioxide (Figure 6.25). During oxidation of doped steels, it is known that the silicon dioxide or the silica formed can only allow the formation of chromia with Mn<sup>43</sup>.

DMA: Figure 6.23e shows the sample exposed to DMA solution. The small particulates present on the metal surface can be attributed to undissolved DMA particles. Figure 6.24 shows an increase in nitrogen content compared to other amines. This could be indicative of the amine complexes on the surface. At higher magnifications, EDS showed a pronounced increase in the silicon content

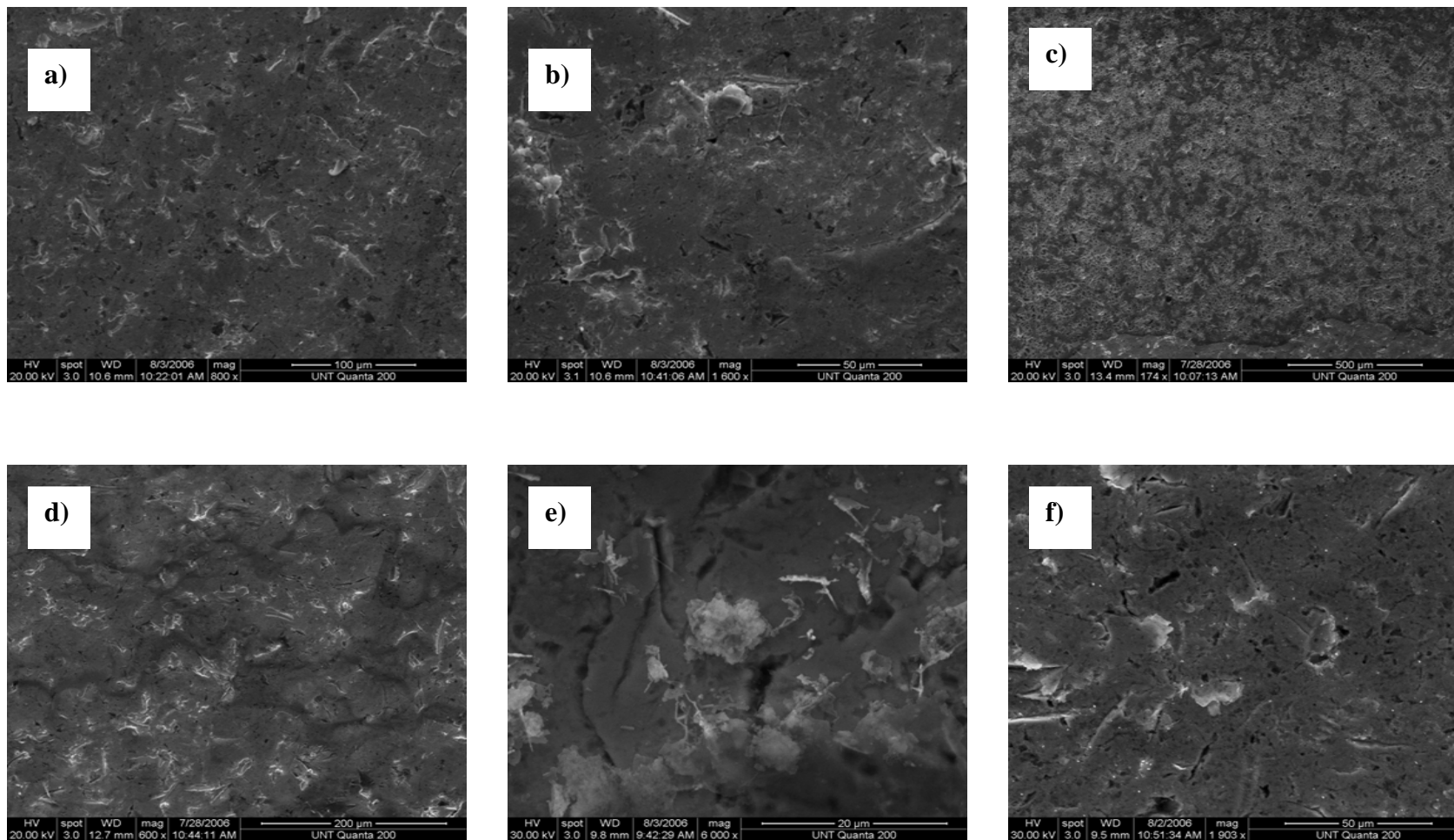


**Figure 6.23. SEM photographs of Inconel alloy 690 samples exposed to a) untreated, b) control (NaOH), c) morpholine, d) ETA, e) DMA, and f) DBU for 3 hrs at 300°C in autoclave at pH = 9.0**

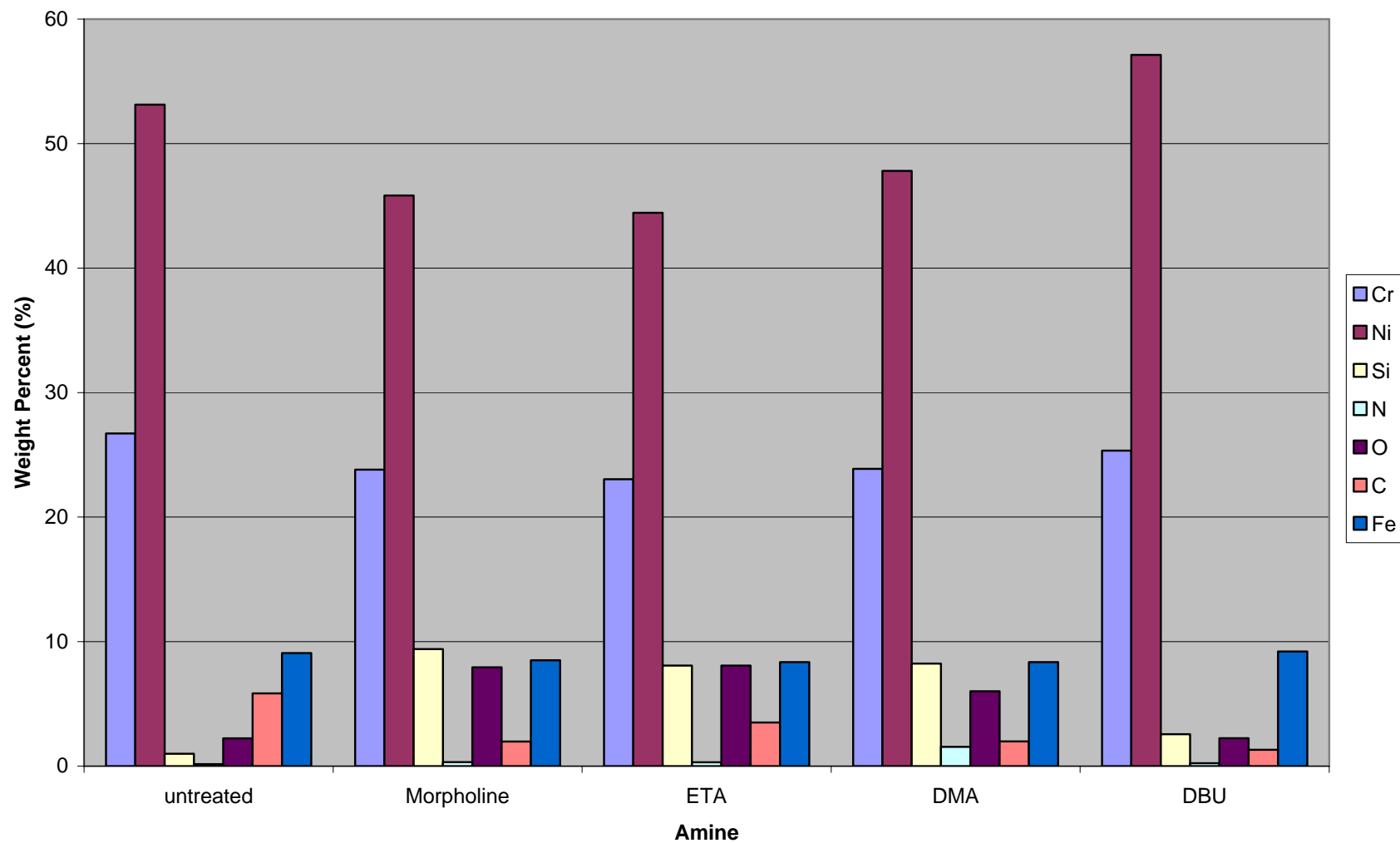


**Figure 6.24. EDS elemental concentration of Inconel 690 samples treated with untreated, morpholine, ETA, DMA, and DBU at 300°C for 3 hrs and pH = 9.0**

and decrease in chromium content. This could be again the presence of silicon oxide layer underneath the chromium passive layer. The samples did not show any film formation like morpholine and ETA but showed crack formation at higher magnifications.

DBU: The samples exposed to DBU solution show no signs of extensive corrosion or any dense or porous film formation (Figure 6.23f). The EDS spectra is not very much different from the untreated sample. The EDS of this area shows a very slight increase in silicon and nickel compared to the untreated sample.

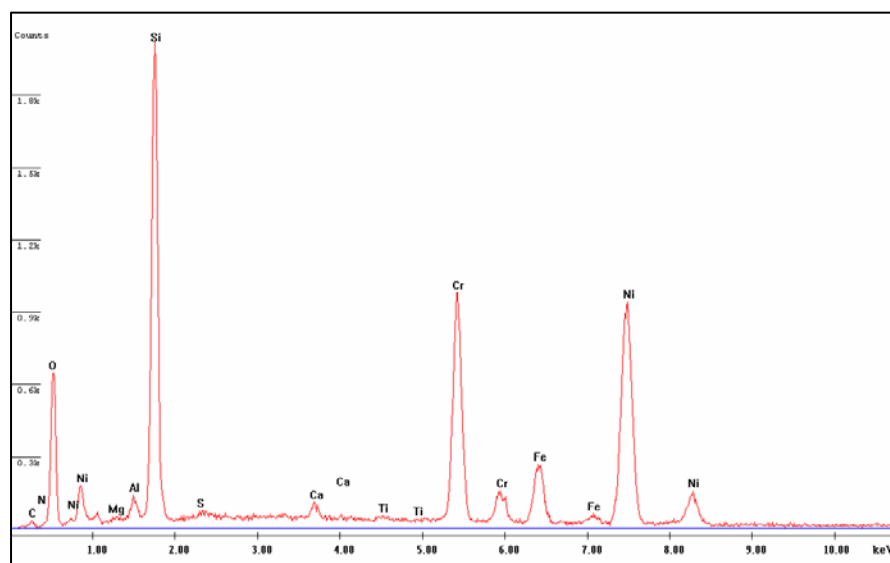


**Figure 6.25. EDS spectra of alloy 690 sample exposed to ETA solution for 3 hrs at 300°C at pH = 9.0**

#### 6.4. Summary and Conclusions

Room Temperature Studies: Alloy 600 sample exposed to DBU solution initially showed adsorption of intermediate organic molecules on the metal surface. As the exposure time was increased, molecules desorbed from the surface. The sample showed diffusion of ions and charge transfer at the metal and solution interface and irrespective of exposure time. The impedance

behavior of Alloy 600 at room temperature in DMA containing solution demonstrated Warburg impedance that is indicative of diffusion controlled process on the metal surface at low frequency region. Impedance data for Alloy 600 exposed to ETA shows an inductive loop which increases with the increase of exposure time, due to film formation and relaxation. Alloy 600 exposed to morpholine - containing solution demonstrated impedance behavior with two clearly defined semicircles that are indicative of formation of a diffusion arc, implying increase in corrosion activity at the metal surface. DMA did not show any desorption or film failure compared to the other amines and ETA showed desorption all through its exposure time. Morpholine showed failure in the film after 12 hours, whereas DBU showed failure after 24 hours. So to conclude DMA showed better corrosion inhibition properties compared to other amines at room temperature.

High Temperature Studies: Samples of alloy 600 and 690 were exposed to DBU, DMA, ETA, morpholine solutions of pH 9.0 at 300°C and were held at 300°C temperature for 3 hours. Nyquist plots obtained from EIS, and polarization resistance obtained from polarization curves were used to study corrosion inhibiting mechanism between the amine solution and the metal surface.

Polarization resistance ( $R_p$ ) of the material is defined as the slope of the potential-current density curve and the following relation gives the relationship between  $R_p$  and  $i_{\text{corr}}$  (corrosion current density):

$$R_p = B/i_{\text{corr}}$$

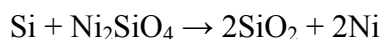
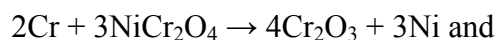
Where, B is the proportionality constant for a particular system and can be determined using  $b_a$  and  $b_c$ , the anodic and cathodic Tafel slopes, i.e.

$$B = b_a * b_c / 2.3 (b_a + b_c)$$

Alloy 600 samples exposed to morpholine and ETA showed an increase in current density (decrease in  $R_p$ ) with increase in temperature indicating increase in corrosion rate. This is consistent with the results showed by Nyquist plots and the polarization resistance values. Morpholine showed an increase in capacitive circle at lower frequency and showed signs of passive layer formation at 300°C, whereas ETA showed increase in corrosion rate in ETA was due to desorption of passive layer. This is consistent with polarization resistance values. Samples exposed to DMA initially showed increase in current density, but as the temperature was increased to 300°C and maintained at that temperature, the sample showed decrease in the current density indicating formation of stable passive layer. This formation of passive layer is indicated by the disappearance of negative inductance loop and formation of capacitive loop at low frequencies<sup>34</sup> and can be further validated by the increase in polarization resistance values. Samples exposed to DBU showed higher corrosion rate at 100°C compared to DMA. The current density increased with increase in temperature and at 300°C, the decrease in the current density was lower when compared to DMA. The Nyquist plots obtained for this sample confirm these conclusions. Inductive loops were observed at 100°C and 300°C, showing desorption of the protective film.

Morphology of the samples was studied using SEM and chemical composition using EDS. SEM images of alloy 600 samples exposed to morpholine showed a formation of porous oxide layer. EDS spectra mainly showed the presence of Ni, Cr and oxygen. SEM and EDS analysis of samples exposed to ETA and DMA solution showed the cracking of the passive oxide layer and formation of a very protective silicon dioxide layer underneath the failed oxide layer. Formation of silicon dioxide layer is known to interfere with the diffusion of ions and charge

transfer between the metal and the solution interface<sup>40, 51, 43</sup>. The mechanism of formation can be explained by the equations given below:



The nickel content in samples soaked in DMA solution was higher compared to ETA. This might be due to dense layer of nickel oxides along with chromium and silicon reducing the corrosion rate in DMA compared to ETA. DBU samples show a formation of porous oxide film. EDS shows less nickel content compare to DMA and higher than ETA and morpholine.

On the other hand alloy 690 samples showed lower corrosion rates (higher polarization resistance) compared to alloy 600. This could be due to high (30%) chromium content in alloy 690 compared to 10% in alloy 600. This is also known to be the reason for less stress corrosion cracking in alloy 690 compared to alloy 600. The sample exposed to morpholine showed signs of pitting at high temperatures. This process is indicated by change of capacitance loop at low frequency to high frequency as the temperature was increase. SEM images of this sample showed very porous oxide layer and EDS sample shows less nickel content compared to the untreated sample. Sample exposed to ETA also showed signs of pitting at high temperatures but at intermediate temperatures, active to passive transition was observed. Overall analysis of SEM and EDS of ETA samples showed decent oxide layer with exceptions of small breakdown in the film exposing oxide layers of Fe, Ni and Si underneath. DMA showed passive behavior at all the temperatures. The SEM of these samples showed small agglomerates of amine or intermediates of amine present in the solution along with presence of small cracks. This is validated by high nitrogen content in these samples compared to the samples exposed to morpholine, ETA and DBU. DBU showed change in the passive layer as the temperature was increased from 100°C to



300°C. SEM images of samples exposed to DBU showed no signs of extensive corrosion and also EDS of the sample showed higher nickel content compared to the other amines.

In general for high temperatures, the corrosion resistance of alloy 600 can be shown as  $\text{ETA} < \text{NaOH} < \text{Morpholine} < \text{DBU} < \text{DMA}$ . In case of alloy 690 it can be shown as  $\text{DMA} < \text{DBU} < \text{Control (NaOH)} < \text{ETA} < \text{Morpholine}$ .

## 6.5. Chapter References

1. Tianbao Du, Jiajian Chen and Dianzhen Cao, “N, N-Dipropynoxy Methyl amine Trimethyl Phosphonate as Corrosion Inhibitor for Iron in Sulfuric Acid”, *Journal of Materials Science* 36(2001), 3903-3907.
2. R. Réquíz, A. Delgado, A. Rivas and A. Ruiz, “The Influence of Hexamethylenetetramine on the Corrosion and Hydrogen Permeation of Type API 5L-X52 Steel”, *Journal of Corrosion Science and Engineering* 6(2003), C086.
3. Popkirov and Schindler, “Validation of Experimental Data in Electrochemical Impedance Spectroscopy”, *Electrochimica Acta* 38(1993)7, pp. 861-867.
4. Jane M. Terry and Laura J. Turbini, “Low Frequency Impedance Investigation on an Epoxide Resin”, Georgia Institute of Technology Atlanta, GA, 605-617.
5. Lu. Q, Stack M.M. and Wiseman.C.R., “A.C. Impedance Spectroscopy as a Technique for Investigating Corrosion of Iron in Hot Flowing Bayer Liquors”, *Journal of Applied Electrochemistry*, 31(2001), 1373-1379.
6. I. Dehri and M. Erbil, “The Effect of Relative Humidity on the Atmospheric Corrosion of Defective Organic Coating Materials: An EIS Study with a New Approach”, *Corrosion Sciences* 42(2000) 969-978.

7. "Evaluation of High Performance Metal Alloys in the STS Launch Environment Using Electrochemical Impedance Spectroscopy", National Aeronautics and Space Administration, Kennedy Space Center, Materials Testing Branch, Document No: MTB-610-89A, August 16, 1990.
8. Danford, "Equivalent Circuit Models for AC Impedance Data Analysis", NASA TM- 100402, June 1990.
9. Jin-Ju Park and Su-II Pyun, "Analysis of Impedance Spectra of a Pitted Inconel alloy 600 Electrode in Chloride Ion-Containing Thiosulfate Solution at Temperature of 298-573K", J. Solid State Electrochemistry (2003) 7, 380-388.
10. Alan D. Zdunek and Xuedong Zhan, "A Field-EIS Probe and Methodology for Measuring Bridge Coating Performance", Fourth World Congress on Coatings Systems for Bridges and Steel Structures, St. Louis, Missouri, February 1-3, 1995.
11. Pettersson and Pound, "Examination of the Role of Molybdenum in Passivation of Stainless Steels using AC Impedance Spectroscopy", Journal of Electrochemical Society 145(1998)5, pp. 1462-1469.
12. Sui, Titchmarsh J.M., Heys G.B., and Congleton J., "Stress Corrosion Cracking of Alloy 600 and Alloy 690 in Hydrogen/Steam at 380°C", Corrosion Science 39 (1997)3, pp. 565-587.
13. Kim and Lee, "Experimental Investigation of Sliding and Fretting Wear of Steam Generator Tube Materials", Wear 250(2001), pp. 673-680.
14. Min-Kyu Lim, Se-Doo Oh and Young-Ze Lee, "Friction and Wear of Inconel 690 and Inconel 600 for Steam generator Tube in Room Temperature Water", Nuclear Engineering and Design 226(2003), pp. 97.

15. Rabak and Smialowska, "The Mechanism of Stress Corrosion Cracking of Alloy 600 in High Temperature Water", *Corrosion Science* 38(1996)6, pp. 971-988.
16. Montemor, Ferreira M. G. S., Hakiki N. E., DA M., Belo C., "Chemical Composition and Electronic Structure of the Oxide Films Formed on 316 L Stainless Steel and Nickel Based Alloys in High Temperature Aqueous Environments", *Corrosion Science* 42 (2000), pp. 1635-1650.
17. Lemire and McRae, "The Corrosion of Alloy 690 in High Temperature Aqueous Media-Thermodynamic Considerations", *Journal of Nuclear Materials* 294 (2001), pp. 141-147.
18. Someswara Rao N., Babu Rao G., Murthy B.N., Das M.M., Prabhakar T., and Lalitha M., "Natural Abundance Nitrogen-15 Nuclear Magnetic Resonance Spectral Studies on Selected Donors", *Spectrochimica Acta AA* 58 (2002), pp. 2737-2757.
19. Yartiza M. Lopez de Jesus, "Characterization of Proton Exchange Membrane and Fuel Cell and PEM Electrolyzer using Non-Steady State Electrochemical Techniques", Masters Thesis, University of Puerto Rico, Mayaguez Campus, 2004.
20. Bastidas, J.L.Polo, E.Cano, C.L.Torres and N. Mora, "Localized Corrosion of Highly Alloyed Stainless Steels in an Ammonium Chloride and Diethylamine Chloride Aqueous Solution", *Materials and Corrosion*, 51(2000), 712-718.
21. J. Manjanna, S. Rangarajan, S.M. Velmurugan and S.V. Narasimhan, "Surface Analysis of Monel, Incoloy, and stainless steel exposed to ETA and LiOH at 150C", *Corrosion Prevention & Control*, March 2002, 18-26.
22. Baek, J. G. Kim, D. H. Hur, and J.S.Kim, "Anodic Film Properties Determined by EIS and Their Relationship with Caustic Stress Corrosion Cracking of Alloy 600", *Corrosion Science* 45 (2003), 983-994.

23. Castañeda and M. Urquidi-Macdonald, "Detecting External Failures in Coated, Buried Pipelines: Theoretical Model and Experimental Verification", *Corrosion* 60 (2004), Issue 6, 538-547.
24. Liya Muslinkina, "Molecular Recognition Studies with Ion-Selective Membranes: Complexation in the Bulk and Molecular Recognition on the Surface", Doctoral Dissertation, Kazan State University, Russia, 2004.
25. Sheba Devan, Venkat R. Subramanian and R. E. White, "Analytical Solution for the Impedance of a Porous Electrode", *Journal of Electrochemical Society* 151 (2004), No. 6, A905-A913.
26. Klimas, K. Fruzzetti, C.W. Turner, P.V. Balakrishnan, G.L. Strati and R.L. Tapping, "Identification and Testing of Amines for Steam Generator Corrosion and Fouling Control", ECI Conference on Heat Exchanger Fouling and Cleaning: Fundamentals and Applications, Santa Fe, New Mexico, USA, 2004.
27. Turner C, and S. Klimas, "The Effect of Alternate Amines on the Rate of Boiler Tube Fouling", EPRI Report TR-108004, September 1997.
28. Kern and D. Landolt, "Adsorption of Organic Corrosion Inhibitors on Iron in the Active and Passive State. A Replacement Reaction between Inhibitor and Water Studied with the Rotatory Quartz Crystal Microbalance", *Electrochimica Acta* 47 (2001).
29. Itagaki, Fukushima H., and Watanabe K., "Application of Electrochemical Impedance Spectroscopy to Analysis of Solvent Extraction Mechanism of Mn (II)-8-Hydroxyquinoline System", *Analytical Sciences* 15 (1999), pp. 1219-1225.

30. Bastidas, Polo J.L., Torres C.L., and Cano E. "A Study on the Stability of AISI 316L Stainless Steel Pitting Corrosion through its Transfer Function", *Corrosion Science* 43 (2001), pp. 269-281.
31. Polo, Cano E., and Bastidas J.M, "AC Impedance Study on the Influence of Molybdenum in Stainless Steel Pitting Corrosion", *Journal of Electroanalytical Chemistry* 537 (2002), pp. 183-187.
32. Hodges, "Electrochemical Phenomenon on Stainless Steel in High and Low Conductivity Solutions", *Journal of Undergraduate Research, University of Florida* 5 (2004)9.
33. Bastidas, J. L. Polo, E. Cano, C. L. Torres, and N. Mora "Localised Corrosion of Highly Alloyed Stainless Steels in an Ammonium Chloride and Diethylamine Chloride Aqueous Solution", *Materials and Corrosion* 51 (2000), pp. 712-718.
34. Nagarajan, M. Karthega, and N. Rajendran, "Pitting Corrosion Studies of Super Austenitic Stainless Steels in Natural Sea Water Using Dynamic Electrochemical Impedance Spectroscopy", *Journal of Applied Electrochemistry* 37 (2007) 2, pp. 195-201.
35. Clerc and Landolt, "AC Impedance Study of Anodic Films in Nickel in LiCl", *Electrochimica Acta* 33 (1988)7, pp. 859-871.
36. Bojinov, Betova I., Fabricius G., Laitinen T., Raicheff R., Saario T., "The Stability of the Passive State of Iron-Chromium Alloys in Sulfuric Acid Solution", *Corrosion Science* 41 (1999), pp. 1557-1584.
37. Cao, "On the Impedance Plane Displays for Irreversible Electrode Reactions Based on the Stability Conditions of the Steady-State –II. Two State Variables besides Electrode Potential", *Electrochimica Acta* 35(1990)5, pp. 837-844.

38. Ningshen, U. Kamachi Mudali, G. Amarendra, P. Gopalan, R.K. Dayal and H.S. Khatak, "Hydrogen Effects on the Passive Film Formation and Pitting Susceptibility of Nitrogen Containing Type 316L Stainless Steels", *Corrosion Science* 48 (2006), pp. 1106-1121.
39. Cachet, Ganne F., Maurin G., Petitjean J., Vivier V., and Wiart R, "EIS Investigation of Zn Dissolution in Aerated Sulfate Medium. Part I: Bulk Zinc", *Electrochimica Acta* 47(2001), pp. 508-518.
40. Grünling and Bauer, "The Role of Silicon in Corrosion-Resistant High Temperature Coatings", *Thin Solid Films* 95 (1982), pp. 3-20.
41. Marcus and Grimal, "The Antagonistic Roles of Chromium and Sulphur in the Passivation of Ni-Cr-Fe Alloys Studied by XPS and Radiochemical Techniques", *Corrosion Science* 31(1990), pp. 377-382.
42. Millett, "PWR Secondary Water Chemistry Guidelines-Revision 5", TR-102134, EPRI 2004.
43. Baccalaro, A. Mattern, I. Hauer, M. Pohl, G. Schneider, and A. Flaig, "Influence of Alloying Elements on the Heat Resistance of Sintered Stainless-Steel Elements", EuroPM2005, Prague.
44. Huntz, Bague V., Beauple G., Haut C., Severac C., Lecour P., Longaygue X., Ropital F., "Effect of Silicon on the Oxidation Resistance of 9% Cr Steels", *Applied Surface Science* 207(2003), pp. 255-275.
45. Keddarn, Oscar Rosa Mottos, and Hisasi Takenouti, "Reaction Model for Iron Dissolution Studied by Electrode Impedance", *Journal of Electrochemical Society* 128 (1981)2, pp. 257-266.
46. Rout, "Electrochemical Impedance Spectroscopy Study on Multi-Layered Coated Steel Sheets", *Corrosion Science* 49 (2007), pp.794-817.
47. Armstrong and Henderson, "The Active-Passive Transition of Nickel in H<sub>2</sub>SO<sub>4</sub>", Short Communication, *Electroanalytical Chemistry and Interfacial Electrochemistry* 39 (1972).

48. Park J.-J., Pyun S.-I., and Lee S.-B, “Growth Kinetics of Passivating Oxide Film of Inconel Alloy in 0.1 M Na<sub>2</sub>SO<sub>4</sub> Solution at 25-300°C using the Abrading Electrode Technique and AC Impedance Spectroscopy”, *Electrochimica Acta* 49 (2004), pp. 281-292.
49. Oltra and Keddam, “Application of EIS to Localized Corrosion”, *Electrochimica Acta* 35 (1990) 10, pp. 1619-1629.
50. Bojinov, G. Fabricius, P. Kinnunen, T. Laitinen, K. Mäkelä, T. Saario and G. Sundholm, “The Mechanism of Transpassive Dissolution of Ni-Cr Alloys in Sulfate Solutions”, *Electrochimica Acta* 45 (2000), pp. 2791-2802.
51. Li, Spiegel M. and Shimada S. “Effect of Al/Si Addition on KCl Induced Corrosion of 9% Cr Steel”, *Material Letters* 58 (2004), pp. 3787-3791.

## CHAPTER 7

### CONCLUSIONS AND RECOMMENDATIONS

The main aim of the research presented in this dissertation was to characterize corrosion deposits formed at Comanche Peak Steam Electric Station (CPSES), Glen Rose, Texas. This plant is a nuclear power station and consists of two units (unit 1 and unit 2) of steam generator systems. Characterization of the corrosion deposits formed in the secondary side of the steam generator units can give very valuable information on chemistry of the plant and can help better plan plant operations and maintenance. Amines play an important role in the chemistry of the corrosion deposits entering the feedwater train. In past electrochemical techniques have been shown to be a very efficient way to study the corrosion inhibition mechanism. A detailed electrochemical impedance studies have been performed to understand the kinetics between the metal surface and different amine solutions. Following conclusions can be drawn based on the results presented in the previous chapters:

Deposit Characterization: Samples were collected and analyzed from different components of secondary side of unit 1 (2004 outage) and unit 2 (2003 outage) and compared to analysis of the samples from previous outages (unit 1-2002 and unit 2-2002). SEM analysis for morphology and oxide thickness, EDS for chemical composition and FTIR for oxide phase analysis was performed on all these samples. In case of unit 1, the average thickness of the oxide layer was found to be 18.90  $\mu\text{m}$  which in comparison with average thickness of 92  $\mu\text{m}$  samples collected from 2002 outage from unit 1. The oxide layer in most of the samples was found to be porous with flaky particles on the top surface.  $\alpha\text{-Fe}_2\text{O}_3$ ,  $\alpha\text{-FeOOH}$  along with traces of  $\text{Fe}_3\text{O}_4$  were found to be the dominant iron oxide phases whereas samples from 2002 outage mostly consisted



of  $\text{Fe}_3\text{O}_4$ . Elemental mapping showed elements Fe, O, Cr, Ni and V with traces of Cl, Si and Li present in the samples from unit 1.

In case of unit 2, the average thickness of the oxide layer was found to be  $17.87\text{ }\mu\text{m}$  which was  $2.5\text{ }\mu\text{m}$  more than the 2002 outage samples from unit 2. The oxide layer in most of the samples was found to be porous with flaky particles on the top surface.  $\alpha\text{-Fe}_2\text{O}_3$ ,  $\text{Fe}_3\text{O}_4$  along with  $\gamma\text{-FeOOH}$  were found to be the dominant iron oxide phases whereas samples from 2002 outage mostly consisted of  $\gamma\text{-Fe}_2\text{O}_3$  and  $\text{Fe}_3\text{O}_4$ . Elemental mapping showed elements Fe, O, Al, Cu, Ni with traces of F, V and Ar present in the samples from unit 2.

Magnetite is a reduced form of iron oxide when compared to maghemite. Therefore one can conclude that the conditions in unit 1 were more reducing than that of unit 2. One of the potential reasons can be the increased addition of hydrazine, which led to reducing conditions in unit 1 when compared to unit 2. Presence of magnetite ( $\text{Fe}_3\text{O}_4$ ) in unit 1 indicates a more reduced phase of iron oxide when compared to unit 2 where maghemite ( $\gamma\text{-Fe}_2\text{O}_3$ ) was found to be the dominant phase.

Maghemite is an oxidized form ( $\text{Fe}^{3+}$  ions) of magnetite and therefore is more stable. The tendency for oxidation of magnetite is higher than that of maghemite. Unit 1 is an older plant than unit 2 and it is also learnt from the history of operation of unit 1 that morpholine was initially used before using dimethylamine (DMA) to control the acidic conditions in the system, whereas DMA has been always been used in unit 2. It is understood from literature that DMA is a better corrosion inhibitor than morpholine. In addition, mentioned in the previous sections, the construction material for tubing used in unit 1 is alloy 600 MA (mill-annealed) whereas in unit 2 is alloy 600 TT (thermally treated). Studies show that thermally treated alloy 600 is less susceptible to corrosion when compared to mill annealed. Thermally treatment of inconel alloy

600 is known to reduce the residual stresses introduced by the final processing steps (straightening and polishing). Mill annealing is known to result in chromium carbide precipitation, an associated chromium depleted layer and trace element segregation. On the other hand, thermal treating results in trace element segregation but no depletion of chromium. So from the history of operation of these units one can conclude that unit 1 can have high deposit formation when compared to unit 2.

Iron Oxide Characterization: Laser induced breakdown spectroscopy (LIBS) and Fourier transform infrared spectroscopy (FTIR) techniques have proven to be efficient tool in characterizing iron oxides. Correlation curves were obtained for different phases of iron oxides using LIBS. By applying the method outlined in this study, LIBS could prove to be a very valuable tool for a quick and accurate method in identifying iron oxides and other corrosion products present in the steam generator system.

FTIR calibration curves were obtained by using different known concentrations of iron oxides mixtures, namely hematite, magnetite and maghemite. Further these calibrations were successfully used to determine the concentration of iron oxide present in the samples collected from steam generator systems at CPSES.

Applying the LIBS and FTIR quantification methods developed in this research study to other elemental oxides like Cu, Cr, Si, Pb, Mn, S, and Mg, etc. can help plant operations and maintenance in better understanding and controlling water chemistry.

Effect of amines on inconel alloys: DMA, ETA and morpholine are commonly used in nuclear power plants to control water chemistry for controlling corrosion and fouling in pressurized water reactors. Experimental analysis was performed to study the effect of the above mentioned amines on inconel alloys 600 and 690. Along with these three amines, effect of DBU on the

inconel surface was also studied. DBU is a ternary amine and its efficiency as corrosion inhibitor has been also studied. DBU has never been used as corrosion inhibitor in power plants or elsewhere. Some initial studies were performed by CPSES to study efficiency of DBU at room temperature and 150°C on low carbon steel. Knowing the inhibition mechanism of DBU on Inconel alloy 600 and 690 at high temperatures and pressure can give very valuable information.

Room temperature studies of inhibition mechanism of amines DBU, DMA, ETA and morpholine on Inconel alloy 600 showed that in case of DMA the film formed on the metal surface even after exposing it to the amine solution for 48 hrs. In case of DBU, the Nyquist plots showed very good protection initially but the film failed after exposing to amine solution for 24 hours. In case of ETA and morpholine the film failed at very short exposure times compared to DBU and DMA.

Inconel alloy 600 and 690 samples when exposed to different amine solutions at high temperature showed passivity at lower temperatures. But as the temperature was increased, alloy 600 and 690 showed failing of the passive layer of chromium oxide. Alloy 690 when exposed to morpholine solution showed highest corrosion resistance after exposing for 3 hours at 300°C temperature unlike other samples exposed to DBU, ETA and DMA. None of the amines showed efficient protection at high temperatures in case of alloy 600. One of the reasons of corrosion resistance of alloy 690 over alloy 600 is due to high chromium content in the former alloy. Alloy 600 has 10% chromium whereas alloy 690 has 30%. Chromium forms a protective layer on the metal surface and interferes with corrosion processes taking place at the metal surface. The chromium content in alloy 600 is not adequate to form a uniform dense passive layer on the metal surface. Alloy 690 samples showed an increase in pitting potential at higher temperatures when exposed to morpholine and ETA. SEM and EDS analysis of the samples (alloy 600 and

690) also showed the possibility of formation of protective silicon dioxide layer underneath the failed chromium film. The concentration of silicon in these alloys is 0.5 percent. Literature suggests that when silicon present in these concentrations in alloy steels can form a protective layer underneath the passive oxide layer of chromium, nickel and iron. This layer of silica interferes with any charge transfer or ion diffusion between the metal and solution interface. In general at high temperatures the corrosion resistance for alloy 600 alloys is shown as  $\text{ETA} < \text{NaOH} < \text{morpholine} < \text{DBU} < \text{DMA}$  and for alloy 690 is  $\text{DMA} < \text{DBU} < \text{Control (NaOH)} < \text{ETA} < \text{morpholine}$ .

Further surface studies of these samples using XPS and SIMS can give more accurate information on the type of oxide formed and the inhibition mechanism of these amines. NMR and liquid ion chromatography can give very valuable information on the breakdown of the amines. This can give a better understanding on how the physical and chemical structure of the amines can affect the inhibition mechanism process in power plants.

## REFERENCES

- Addepalli and Kelber. (2003). "Effects of Amine Inhibitors on the Corrosion of Iron in Sulfate Media: Weightloss Measurements," Comanche Peak Steam Electric Station.
- Addepalli and Kelber. (2003). "Role of Dissolved Oxygen in the Inhibitor Protection of Iron Films in Sulfate Solutions-Latest Results," Comanche Peak Steam Electric Station.
- Alcalál, Criado and Real. (2004). "Synthesis of Nanocrystalline Magnetite by Mechanical Alloying of Iron and Hematite," *Journal of Materials Science* 39: 2365-2370.
- Armstrong and Henderson. (1972). "The Active-Passive Transition of Nickel in  $H_2SO_4$ ," [Short Communication], *Electroanalytical Chemistry and Interfacial Electrochemistry* 39.
- Atenas and Mielczarski. "Some Aspects about Iron Oxidation Reaction in Aqueous Solutions," Cabierta, Universidad De Chile, Vol. 23, ISSN: 0717 8948.
- Ayyub, Multani, Barma, Palkar, and Vijayaraghavan. (1988). "Size-induced Structural Phase Transitions and Hyperfine Properties of Microcrystalline  $Fe_2O_3$ ," *Journal of Physics C: Solid State Physics* 21: 2229-2245.
- Baccalaro, Mattern, Hauer, Pohl, Schneider and Flaig. "Influence of Alloying Elements on the Heat Resistance of Sintered Stainless-Steel Elements," EuroPM2005, Prague.
- Baek, Kim, Hur and Kim. (2003). "Anodic Film Properties Determined by EIS and Their Relationship with Caustic Stress Corrosion Cracking of Alloy 600," *Corrosion Science* 45: 983-994.
- Baucells, Ferrer, Gomez, Lacort and Roura. (1993). "Quantitative Analysis of Caffeine Applied to Pharmaceutical Industry," *Journal of Molecular Structure* 294: 219-222.
- Bastidas, Polo, Cano, Torres and Mora. (2000). "Localized Corrosion of Highly Alloyed Stainless Steels in an Ammonium Chloride and Diethylamine Chloride Aqueous Solution," *Materials and Corrosion* 51: 712-718.
- Bastidas, Polo, Torres and Cano. (2001). "A Study on the Stability of AISI 316L Stainless Steel Pitting Corrosion through its Transfer Function," *Corrosion Science* 43: 269-281.
- Bette and Noll. (2004). "High Speed Laser-Induced Breakdown Spectrometry for Scanning Microanalysis," *Journal of Applied Physics* 37: 1281-1288.
- Beverkog and Puigdomenech. (1999). "Pourbiac Diagrams for the Ternary System of Iron-Chromium-Nickel," *Corrosion* 55.
- Bloom and Daniels. (2001). "Advance amines cut Condensate Corrosion," *Power* 145(4): 81.

- Blesa, Maroto, Passaggio, Labenski and Saragovi-Badler. (1978). "Moessbauer Study of the Behaviour of Synthetic Corrosion Products of Nuclear Power Plants," *Radiation Physical Chemistry* 11: 321-326.
- Boer and Dekkers. (2001). "Unusual Thermomagnetic Behaviour of Hematites; Neoformation of a Highly Magnetic Spinel Phase on Heating in Air," *Geophysical Journal of International* 144: 481-494.
- Bogard, Johnson, Kumar and Cunningham. (1982). "Quantitative Analysis of Nitrate Ion in Ambient Aerosols by Fourier Transform Infrared Spectroscopy," *Environmental Science and Technology* 16: 138-140.
- Bojinov, Betova, Fabricius, Laitinen, Raicheff, and Saario. (1999). "The Stability of the Passive State of Iron-Chromium Alloys in Sulfuric Acid Solution," *Corrosion Science* 41: 1557-1584.
- Brundle, Evans and Wilson. (1992). *Encyclopedia of Materials Characterization*. Butterworth, Heinemann Co. ISBN-0-7506-9168-920.
- Bojinov et al. (2000). "The Mechanism of Transpassive Dissolution of Ni-Cr Alloys in Sulfate Solutions," *Electrochimica Acta* 45: 2791-2802.
- Cachet, Ganne, Maurin, Petitjean, Vivier and Wiart. (2001). "EIS Investigation of Zn Dissolution in Aerated Sulfate Medium. Part I: Bulk Zinc," *Electrochimica Acta* 47: 508-518.
- Cao. (1990). "On the Impedance Plane Displays for Irreversible Electrode Reactions Based on the Stability Conditions of the Steady-State –II. Two State Variables Besides Electrode Potential," *Electrochimica Acta* 35(5): 837-844.
- Castañeda and Urquidi-Macdonald. (2004). "Detecting External Failures in Coated, Buried Pipelines: Theoretical Model and Experimental Verification," *Corrosion* 60(6): 538-547.
- Castle, Visser, Smith, and Winefordner. (1997). "Level Populations in a Laser-Induced Plasma on a Lead Target," *Spectrochimica Acta, Part B* 59: 1995-2009.
- Chastukhin, Izotov, Gorichev and Kutepov. (2003). "Analysis of  $\text{Fe}_2\text{O}_3$  and  $\text{Fe}_3\text{O}_4$  Dissolution Kinetics in Terms of the Chain Mechanism Model," *Theoretical Foundations of Chemical Engineering* 37(4): 398-406.
- Cornell and Schwertmann. (1996). *The Iron Oxides - Structures, Properties, Reactions, Occurrence and Uses*. New York: VCH Publishers, ISBN – 3-527-28576-8.
- Corsi, Cristoforetti, Palleschi, Salvetti and Tognoni. (2001). "A Fast and Accurate Method for the Determination of Precious Alloys Caratage by Laser Induced Plasma Spectroscopy," *The European Physical Journal D* 13: 373-377.
- Cravetchi, Taschuk, Tsui, and Fedossejevs. (2004). "Scanning Microanalysis of Al alloys by Laser –Induced Breakdown Spectroscopy," *Spectrochimica Acta, Part B*, 59: 439-1450.

- Cyrus and Maggi. (2003). "Steam Generator Deposit Trends and Characterization for Operating Nuclear Power Stations," Steam Generator Secondary Side Management Conference, February 10-12.
- Danford. (1990, June). "Equivalent Circuit Models for AC Impedance Data Analysis," NASA TM- 100402.
- Davranche and Bollinger. (2001). "A Desorption-Dissolution Model for Metal Release from Polluted Soil under Reductive Conditions," *Journal of Environmental Quality* 30: 1581-1586.
- Dehri and M. Erbil. (2000). "The Effect of Relative Humidity on the Atmospheric Corrosion of Defective Organic Coating Materials: An EIS Study with a New Approach," *Corrosion Sciences* 42: 969-978.
- Do, Hee, Sik, Sub and Chul. (2001). "High Temperature Application of EDTA Solvents for Iron Oxide Removal," *Journal of Nuclear Materials* 299: 271-273.
- Domingo and Clementa. (1991). "The Pathways to Spinel Iron Oxides by Oxidation of Iron (II) in Basic Media," *Materials Research Bulletin* 26: 47-55.
- Dorra and Niemax. (1990). "Temporal and Spatial Distribution of Analyte Atoms and Ions on Microplasmas Produced by Laser Ablation of Solid Samples," *Spectrochimica Acta* 45B(8): 917-926.
- Du, Chen and Cao. (2001). "N, N-Dipropynoxy Methyl Amine Trimethyl Phosphonate as Corrosion Inhibitor for Iron in Sulfuric Acid," *Journal of Materials Science* 36: 3903-3907.
- EPRI. (2002a). *Protonation Constant of Morpholine, Dimethylamine and Ethanolamine to 290 °C and the Effect of Morpholine and Dimethylamine on the Surface Charge of Magnetite at 150-250 °C*. Report No. 1003179.
- EPRI. (2002b). *Identification and Testing of Amines for Steam Generator Chemistry and Deposit Control*. Report No. TR-1002773.
- EPRI. (1999). *Surface Chemistry Interventions to Control Boiler Tube Fouling*. Report No. TR-110083.
- EPRI. (1998). *Flow-Associated Corrosion in Power Plants*. Report No. TR-106611-R1.
- EPRI. (1997). *The Effect of Alternative Amines on the Rate of Boiler Tube Fouling*. Report No. TR-108004.
- EPRI. (1996). *Characterization of PWR Steam Generator Deposits*. Report No. TR-106048, Research Project S523-01.

- EPRI. (1994). *Qualification Testing of Three Advanced Amines for Secondary System pH Control in Once-Through Steam Generator Plants*. Report No. TR-103098.
- Fellers. Chemistry Projects and Programs, TXU. Interview by author, 17 December, 2002, Glenn Rose, Texas.
- Fellers and Nichols. (2002). "Strategic Elements of Steam Cycle Control Practices at TXU's Comanche Peak Steam Electric Station," *Chimie, France*.
- Finch and Sinha. (1957). "An Electron-Diffraction Study of the Transformation  $\alpha$ -Fe<sub>2</sub>O<sub>3</sub> to  $\gamma$ -Fe<sub>2</sub>O<sub>3</sub>," *Proceedings of Royal Society, London A* 241: 1-8.
- Friedel. (2002). "Characterization of Oxidized Steel Surfaces with Microscopic and Analytical Methods," *Sonderbaende der Praktischen Metallographie* 33: 59-67.
- Galbács, Gornushkin, Smith and Winefordner. (2001). "Semi-quantitative Analysis of Binary Alloys using Laser-Induced Breakdown Spectroscopy and a New Calibration Approach Based on Linear Correlation," *Spectrochimica Acta Part B* 56: 1159-1173.
- Garcell, Morales, Andres-Verges, Tartaj and Serna. (1998). "Interfacial and Rheological Characteristics of Maghemite Aqueous Solutions," *Journal of Colloid and Interface Science* 205(2): 470-475.
- Gornushkin, Ruiz-Medina, Anzano, Smith and Winefordner. (2000). "Identification of Particulate Materials by Correlation Analysis Using a Microscopic Laser Induced Breakdown Spectrometer," *Journal of Analytical Atomic Spectroscopy* 15: 581-586.
- Greene and Donaldson. (1993). "The Role Played by Ion Chromatography in the Assessment of Amines for Two-Phase Erosion-Corrosion Control in Nuclear Electric's Steam-Water Circuits," *Journal of Chromatography* 640: 303-308.
- Grünling and Bauer. (1982). "The Role of Silicon in Corrosion-Resistant High Temperature Coatings," *Thin Solid Films* 95: 3-20.
- Hodges. (2004). "Electrochemical Phenomenon on Stainless Steel in High and Low Conductivity Solutions," *University of Florida Journal of Undergraduate Research* 5: 9.
- Hofmann, Campbell, Kaczmarek and Welzel. (1996). "Mechanochemical Transformation of Hematite to Magnetite: Structural Investigation," *Material Science Forum* 228-231(2): 607-614,
- Hohreiter, Carranza and Hahn. (2004). "Temporal Analysis of Laser-Induced Plasma Properties as related to Laser-Induced Breakdown Spectroscopy," *Spectrochimica Acta Part B* 59: 327-333.
- Huntz, Bague, Beauple, Haut, Severac, Lecour, Longaygue and Ropital. (2003). "Effect of Silicon on the Oxidation Resistance of 9% Cr Steels," *Applied Surface Science* 207: 255-275.



- Ishii and Nakahira. (1972). "Infrared Absorption Spectra and Cation Distribution in  $(\text{MnFe})_3\text{O}_4$ ," Solid State Communications 11: 209-212.
- Ishikawa, Nishimori, Yasukawa and Kandori. (1993). "Formation of  $\gamma\text{-FeOOH}$  in the Presence of Amines," Journal of Materials Science Letters 12: 1359-1361.
- Ishikawa, Takeda and Kandori. (1992). "Effects of Amines in the Formation of  $\beta\text{-Ferric Oxide Hydroxide}$ ," Journal of Materials Science Letters 27: 4531-4535.
- Itagaki, Fukushima and Watanabe. (1999). "Application of Electrochemical Impedance Spectroscopy to Analysis of Solvent Extraction Mechanism of Mn (II)-8-Hydroxyquinoline System," Analytical Sciences 15: 1219-1225.
- Jobe. (1997). *The Calculated Solubilities of Hematite, Magnetite and Lepidocrocite in Steam Generator Feed Trains*. AECL.
- Keddam, Mottos and Takenouti. (1981). "Reaction Model for Iron Dissolution Studied by Electrode Impedance," Journal of Electrochemical Society 128(2): 257-266.
- Kern and Landolt. (2001). "Adsorption of Organic Corrosion Inhibitors on Iron in the Active and Passive State. A Replacement Reaction between Inhibitor and Water Studied with the Rotatory Quartz Crystal Microbalance," Electrochimica 47.
- Kim and Lee. (2001). "Experimental Investigation of Sliding and Fretting Wear of Steam Generator Tube Materials," Wear 250: 673-680.
- Kim, Kim, Lee, Kim, Lee, Hur, Choi and Han. (2003). "Wear Behavior of Steam Generator Tubes in Nuclear Power Plant Operating Condition," *Transactions of the 17<sup>th</sup> International Conference on Structural Mechanics in Reactor Technology*. Prague, Czech Republic, August 17-22, 2003.
- Klimas, Fruzzetti, Turner, Balakrishnan, Strati and Tapping. (2004). *Identification and Testing of Amines for Steam Generator Corrosion and Fouling Control*. ECI Conference on Heat Exchanger Fouling and Cleaning: Fundamentals and Applications. Santa Fe, New Mexico.
- Ko. (1989). "On the Internal Standardization in Optical Emission Spectrometry of Microplasmas Produced by Laser Ablation of Solid Samples," Fresenius Z. Analytical Chemistry 335: 648-651.
- Krivacsy and Hlavay. (1995). "Comparison of Calibration Methods in Quantitative Diffuse Reflectance Infrared Spectroscopy," Talanta 42(4): 613-620.
- Kumbhar, Narasimhan and Mathur. (1998). "Spectrophotometric Method for Determination Parts Per Million Levels of Cyclohexylamine in Water," Talanta 47: 421-437.
- Laberty and Navrotsky. (1998). "Energetics of Stable and Metastable Low-temperature Iron Oxides and Oxyhydroxides," Geochimica et Cosmochimica Acta 62(17): 2905-2913.

- Legodi, De Waal and Potgieter. (2001). "Quantitative Determination of  $\text{CaCO}_3$  in Cement Blends by FT-IR," *Society for Applied Spectroscopy* 55(3): 361-365.
- Lemire and McRae. (2001). "The Corrosion of Alloy 690 in High Temperature Aqueous Media-Thermodynamic Considerations," *Journal of Nuclear Materials* 294: 141-147.
- Liu, Mao, Yoo and Russo. (1999). "Early Phase Laser Induced Plasma Diagnostics and Mass Removal during Single-Pulse Laser Ablation of Silicon," *Spectrochimica Acta Part B* 54: 1607-1624.
- Lu, Stack and Wiseman. (2001). "AC Impedance Spectroscopy as a Technique for Investigating Corrosion of Iron in Hot Flowing Bayer Liquors," *Journal of Applied Electrochemistry* 31: 1373-1379.
- Lim and Lee. (2003). "Friction and Wear of Inconel 690 and Inconel 600 for Steam Generator Tube in Room Temperature Water," *Nuclear Engineering and Design* 226: 97.
- Manjanna, Rangarajan, Velmurugan and Narasimhan. (2002, March). "Surface Analysis of Monel, Incoloy, and Stainless Steel Exposed to ETA and LiOH at 150 °C," *Corrosion Prevention & Control*, 18-26.
- Marcus and Oudar. (1995). *Corrosion Mechanism in Theory and Practice*. New York: Marcel Dekker, Inc. ISBN – 0-8247-9592-X.
- Marcus and Grimal. (1990). "The Antagonistic Roles of Chromium and Sulphur in the Passivation of Ni-Cr-Fe Alloys Studied by XPS and Radiochemical Techniques," *Corrosion Science* 31: 377-382.
- Marks and Varrin. (2003). "Application of Deposit Oxidation Models to Plant Practices: The Seabrook Example," *Steam Generator Secondary Side Conference*, February 10-12.
- Meillon, Dammak, Flavin and Pascard. (1995). "Existence of a Direct Phase Transformation from Hematite to Maghemite," *Philosophical Magazine Letters* 72: 105-110.
- Meissner, Lippert, Wokaun and Guenther. (2004). "Analysis of Trace Metals in Comparison of Laser-Induced Breakdown Spectroscopy with LA-ICP-MS," *Thin Solid Films* 453-454: 316-322.
- Melamud and Yur'ev. (2001). "Study of the Hematite-Magnetite Reduction," *Metally* 1: 3-13.
- Millett. (1997). "Recent Advances in Water Chemistry Control at US PWRs," *Proceedings of 58<sup>th</sup> International Water Conference*, Pittsburgh, PA, October.
- Millett. (2000). *PWR Secondary Water Chemistry Guidelines*. TR-102134-R5, Final Report.
- Monchoux and Rabkin. (2002). "Microstructure Evolution and Interfacial Properties in the Fe-Pb System," *Acta Materialia* 50: 3159-3174.

- Montemor, Ferreira, Hakiki, Da and Belo. (2000). "Chemical Composition and Electronic Structure of the Oxide Films Formed on 316 L Stainless Steel and Nickel Based Alloys in High Temperature Aqueous Environments," *Corrosion Science* 42: 1635- 1650.
- Mora-Mendoza and Turgoose. (2002). "Fe<sub>3</sub>C influence on the Corrosion Rate of Mild Steel in Aqueous CO<sub>2</sub> Systems under Turbulent Flow Conditions," *Corrosion Science* 44: 1223-1246.
- Music, Krehula, Popovic, and Skoko. (2003). "Some Factors Influencing Forced Hydrolysis of FeCl<sub>3</sub> Solutions," *Materials Letters* 57: 1096-1102.87.
- Nagarajan et al. (2007). "Pitting Corrosion Studies of Super Austenitic Stainless Steels in Natural Sea Water using Dynamic Electrochemical Impedance Spectroscopy," *Journal of Applied Electrochemistry* 37(2): 195-201.
- Namduri. (2003). *Characterization of Iron Oxide Deposits formed at Comanche Peak Steam Electric Station*. Masters thesis, University of North Texas, Denton.
- Nasrazadani. (1984). *Formation and Transformation Characteristics of Magnetite (Fe<sub>3</sub>O<sub>4</sub>) under Different Laboratory and Field Conditions*. PhD. dissertation, Louisiana State University.
- Nasrazadani, and Namduri. (2002). *Characterization of Iron Oxide Deposits formed at Comanche Peak Steam Electric Station (CPSES)*. Final Report.
- Nasrazadani, Namduri, Fellers, Stevens and Theimer. (2003). "Application of FTIR in the Analysis of Iron Oxides and Oxyhydroxides Formed in PWR Secondary System," *Steam Generator Secondary Side Management Conference*, February 10-12.
- Nasrazadani and Raman. (1993). "Application of IR Spectra to Study the Rust Systems," *Corrosion Science* 34(8): 1335-1365.
- National Aeronautics and Space Administration. (1990). *Evaluation of High Performance Metal Alloys in the STS Launch Environment using Electrochemical Impedance Spectroscopy*. Kennedy Space Center, Materials Testing Branch, Document No: MTB-610-89A.
- Ningshen, Kamachi Mudali, Amarendra, Gopalan, Dayal and Khatak. (2006). "Hydrogen Effects on the Passive Film Formation and Pitting Susceptibility of Nitrogen Containing Type 316L Stainless Steels," *Corrosion Science* 48: 1106-1121.
- Nordmann and Fiquet. (1996). "Selection Criteria for the Best Secondary Water Chemistry," *Nuclear Engineering and Design* 160: 193-201.
- Ochaoa, Baril, Moran and Pebere. (2002). "Study of the Properties of a Multi-Component Inhibitor used for Water Treatment in Cooling Circuits," *Journal of Applied Electrochemistry* 32: 497-504,.

- Ogura and Sato. (1979). "Cathodic Dissolution of the Passive Film on Iron – I. Kinetics and Mechanism," *Electrochimica Acta* 25: 857-862.
- Olowe and Génin. (1991). "The Mechanism of Oxidation of Ferrous Hydroxide in Sulphated Aqueous Media: Importance of the Initial Ratio of the Reactants," *Corrosion Science* 32(9): 965-984.
- Olsson, Agarwal, Frey and Landolt. (2000). "An XPS Study of the Adsorption of Organic Inhibitors on Mild Steel Surfaces," *Corrosion Science* 42: 1197.
- Oltra and Keddad. (1990). "Application of EIS to Localized Corrosion," *Electrochimica Acta* 35(10): 1619-1629.
- Park. (2003). "Analysis of Impedance Spectra of a Pitted Inconel Alloy 600 Electrode in Chloride Ion-Containing Thiosulfate Solution at Temperature of 298-573K," *J. Solid State Electrochemistry* 7: 380-388.
- Park and Lee. (2004). "Growth Kinetics of Passivating Oxide Film of Inconel Alloy in 0.1 M Na<sub>2</sub>SO<sub>4</sub> solution at 25-300 °C using the Abrading Electrode Technique and AC Impedance Spectroscopy," *Electrochimica Acta* 49: 281-292.
- Passell, Welty, Hobart and Hobart. (1987). "Use of Organic Amines in Water Chemistry Control for Pressurized Water Reactor Secondary Systems," *Progress in Nuclear Energy* 20(3): 235-254.
- Payer, Boyd, Lippold and Fisher. (1980, May). "NBS-Battelle Cost of Corrosion Study (70 billion!)," *Materials Performance*.
- Pettersson and Pound. (1998). "Examination of the Role of Molybdenum in Passivation of Stainless Steels using AC Impedance Spectroscopy," *Journal of Electrochemical Society* 145(5): 1462-1469.
- Popkurov and Schindler. (1993). "Validation of Experimental Data in Electrochemical Impedance Spectroscopy," *Electrochimica Acta* 38(7): 861-867.
- Polo, Cano and Bastidas. (2002). "AC Impedance Study on the Influence of Molybdenum in Stainless Steel Pitting Corrosion," *Journal of Electroanalytical Chemistry* 537: 183-187.
- Rabak and Smialowska. (1996). "The Mechanism of Stress Corrosion Cracking of Alloy 600 in High Temperature Water," *Corrosion Science* 38(6): 971-988.
- Radziemski. (1994). "Review of Selected Analytical Applications of Laser Plasmas and Laser Ablation," *Microchemical Journal* 50: 218-234.
- Rainer. (1999). "Determination of Amines used in the Oil and Gas Industry (Upstream Section) by Ion Chromatography," *Journal of Chromatography A* 850: 289-295.

- Randrianantoandro, Mercier, Hervieu and Greneche. (2001). "Direct Phase Transformation from Hematite to Maghemite During High Energy Ball Milling," *Materials Letters* 47:150-158.
- Raymond, De Murcia and Dhaunut. (1987). "Speciation and Analysis of Corrosion Products in the Primary Coolant of Pressurized Water Reactors," *Analytica Chimica Acta* 195: 265-273.
- Réquiz, Delgado, Rivas and Ruiz. (2003). "The Influence of Hexamethylenetetramine on the Corrosion and Hydrogen Permeation of Type API 5L-X52 Steel," *Journal of Corrosion Science and Engineering* 6: C086.
- Reig, Gimeno Adelantado, Peris Martinez, Moya Moreno and Domenech Cerbo. (1999). "FT-IR Quantitative Analysis of Solvent Mixtures by the Constant Ratio Method," *Journal of Molecular Structure* 480-481: 529-534.
- Reig, Gimeno Adelantado and Moya Moreno. (2002). "FTIR Quantitative Analysis of Calcium Carbonate(calcite) and Silica (quartz) Mixtures Using the Constant Ratio Method. Application to Geological Samples," *Talanta* 58: 811-821.
- Rout. (2007). "Electrochemical Impedance Spectroscopy Study on Multi-Layered Coated Steel Sheets," *Corrosion Science* 49: 794-817.
- Rusak, Castle, Smith and Winefordner. (1998). "Recent Trends and the Future of Laser Induced Plasma Spectroscopy," *Trends in Analytical Chemistry* 17(8, 9): 453-461.
- Sabsabi, Lucas and Héon. (2004). *Laser-Induced Breakdown Spectroscopy: A New Tool for Process Control*. 16<sup>th</sup> WCNDT, Montreal, Canada, Aug 30 - Sep 3. Paper Code 679.
- Sala, Combrade, Erre and Gelpi. (1993). *Local Chemistry and Formation of Deposits on the Secondary Side of Steam Generators. A Laboratory Study*. Sixth International Symposium on Environmental Degradation of Materials in Nuclear Power Systems-Water Reactors, San Diego, CA, Aug 1-5.
- Salih, Mazhar and Mahanny. (2004). "The Effect of Sour Gases and Some Anions on the Corrosion Behavior of Carbon Steel," *Portugaliae Electrochimica Acta* 22: 205-225.
- Schimanke and Martin. (2000). "In Situ XRD Study of the Phase Transition of Nanocrystalline Maghemite ( $\text{Fe}_3\text{O}_4$ ) to Hematite ( $\alpha\text{-Fe}_2\text{O}_3$ )," *Solid State Ionics* 136-137: 1235-1240.
- Schneider, Ruhle and Riess. (2000). *Magnetite Deposition in PWR Secondary Systems* 80: 11. VGB-Kraftwerktechnik GmbH, Essen, Germany.
- Sei, Cook and Townsend. (1997). "Characterization of Iron Oxides Commonly Formed as Corrosion Products on Steel," *Hyperfine Interaction* 1998: 59-65.
- Sheba, Venkat and White. (2004). "Analytical Solution for the Impedance of a Porous Electrode," *Journal of Electrochemical Society* 151(6): A905-A913.

- Srikantiah and Chappidi. (2000). "Particle Deposition and Fouling in PWR Steam Generators," Nuclear Engineering and Design 200: 285-294.
- Stevens. (2003, July). *Secondary System Oxide Characterization Study at Comanche Peak*. 12<sup>th</sup> Annual Southwest Chemistry Workshop, Dallas, TX.
- Stevens, Fellers, and Orbon. (2002). *S/G Deposit Control Program Assessment at Comanche Peak*. Chimie 2002, France.
- Stevens, Theimer, Nasrazadani and Namduri. (2006). *Secondary System Oxide and Lead Study at Comanche Peak*. International Water Conference, October 22-26, Pittsburgh, PA.
- Sudakar, Subanna and Kutty. (2003). "Effect of Anions on the Phase Stability of  $\gamma$ -FeOOH Nanoparticles and the Magnetic Properties of Gamma –Ferric Oxide Derived from Lepidocrocite," Journal of Physics and Chemistry of Solids 64: 2337-2349.
- Sui, Titchmarsh, Heys and Congleton. (1997). "Stress Corrosion Cracking of Alloy 600 and Alloy 690 in Hydrogen/Steam at 380 °C," Corrosion Science 39(3): 565-587.
- Taylor. (1984a). "Influence of Chloride on the Formation of Iron Oxides form Fe (II) Chloride. I. Effect of [Cl]/[Fe] on the Formation of Magnetite," Clays and Clay Minerals 32(3): 167-174.
- Taylor. (1984b). "Influence of Chloride on the Formation of Iron Oxides form Fe (II) Chloride. II. Effect of [Cl] on the Formation of Lepidocrocite and Its Crystallinity," Clays and Clay Minerals 32(3): 175-180.
- Togawa, Sano, Wada, Yamamoto, Tsuji and Tamaura. (1996). "The Effect of the Crystal Orientation on the Rate of Formation of Cation-Excess Magnetite," Solid State Ionics 89: 279-286.
- Torres, Blesa and Matijevic. (1990). "Interactions of Metal Hydrous Oxides with Chelating Agents. IX. Reductive Dissolution of Hematite and Magnetite by Aminocarboxylic Acids," Journal of Colloid and Interface Science 134(2): 475-485.
- United States Nuclear Regulatory Commission. (2004, January). *Steam Generator Tube Issues Fact Sheet*.
- Wade. (1995, August). "Steam Generator Degradation and its Impact on Continued Operation of Pressurized Water Reactors in the United States," Energy Information Administration/ Electric Power Monthly.
- Wainner, Harmon, Miziolek, McNesby and French. (2001). "Analysis of Environmental Lead Contamination: Comparison of LIBS Field and Laboratory Instruments," Spectrochimica Acta Part B 56: 777-793.

- Weritz, Ryahi, Schaurich, Taffe and Wilsch. (2005). "Quantitative Determination of Sulfur Content in Concrete with Laser Breakdown Spectroscopy," *Spectrochimica Acta Part B* 60(7-8): 1121-1131.
- Whitehouse, Young, Botheroyd, Evans, Lawson and Wright. (2000). *In-vessel Material Analysis of AGR Steam Generator Tubes using a Fiber Probe LIBS Instrument*. LIBS 2000 Conference, Terrenia, Pisa, (Italy), October 8-12.
- Whitehouse, Young, Botheroyd, Lawson, Evans and Wright. (2001). "Remote Material Analysis of Nuclear Power Station Generator Tubes by Laser-Induced Breakdown Spectroscopy," *Spectrochimica Acta Part B* 56: 821-830.
- Wiens, Arvidson, Cremers, Ferris, Blacic, Seelos and Deal. (2002). "Combined Remote Mineralogical and Elemental Identification from Rovers: Field and Laboratory Tests using Reflectance and Laser-Induced Breakdown Spectroscopy," *Journal of Geophysical Research* 107(E11): 8003.
- Wu, Ibrahim, Abbas and Ju. (2003). "Surface Structure of  $\alpha$ -Fe<sub>2</sub>O<sub>3</sub> Nanocrystal Observed by O K-Edge X-ray Absorption Spectroscopy," *Nuclear Instruments and Methods in Physics Research, Section B; Beam Interactions with Materials and Atoms* 199: 291-294.
- Xu, Addepalli and Kelber. (1996). *EQCM studies of Amine Inhibition*. Comanche Peak Steam Electric Station.
- Xu, Cornilsen, Popko, Wei, Pennington and Wood. (2001). "Quantitative Mineral Analysis by FTIR Spectroscopy," *Internet Journal of Vibrational Spectroscopy* 5(4): 1-12.
- Xu, Yin, Li and Chen. (1992). "Preparation of Mono-Phasic Iron Oxides and Ferrite Spinel and Analysis of their Mixtures," *Applied Catalysis A: General* 89: 117-129.
- Yartiza. (2004). *Characterization of Proton Exchange Membrane and Fuel Cell and PEM Electrolyzer using Non-Steady State Electrochemical Techniques*. Masters thesis, University of Puerto Rico, Mayaguez Campus.
- Zdunek and Zhan. (2004). *A Field-EIS Probe and Methodology for Measuring Bridge Coating Performance*. Fourth World Congress on Coatings Systems for Bridges and Steel Structures, St. Louis, Missouri, February 1-3.